
Magnetic field expulsion in driven
 $\text{YB}_2\text{C}_3\text{O}_{6.48}$

DISSERTATION

*zur Erlangung des Doktorgrades an der Fakultät für
Mathematik, Informatik und Naturwissenschaften*

Fachbereich Physik

DER UNIVERSITÄT HAMBURG

vorgelegt von

Sebastian Fava

Hamburg

2024

Gutachter/innen der Dissertation:	Prof. Dr. Andrea Cavalleri Prof. Dr. Martin Christian Eckstein
Zusammensetzung der Prüfungskommission:	Prof. Dr. Andrea Cavalleri Prof. Dr. Martin Christian Eckstein Prof. Dr. Ludwig Mathey Prof. Dr. Tim Oliver Wehling Prof. Dr. Dieter Hans Jaksch
Vorsitzende/r der Prüfungskommission:	Prof. Dr. Ludwig Mathey
Datum der Disputation:	26.11.2024
Vorsitzender des Fach-Promotionsausschusses PHYSIK:	Prof. Dr. Markus Drescher
Leiter des Fachbereichs PHYSIK:	Prof. Dr. Wolfgang J. Parak
Dekan der Fakultät MIN:	Prof. Dr.-Ing. Norbert Ritter

Declaration on oath

I hereby declare and affirm that this doctoral dissertation is my own work and that I have not used any aids and sources other than those indicated.

If electronic resources based on generative artificial intelligence (gAI) were used in the course of writing this dissertation, I confirm that my own work was the main and value-adding contribution and that complete documentation of all resources used is available in accordance with good scientific practice. I am responsible for any erroneous or distorted content, incorrect references, violations of data protection and copyright law or plagiarism that may have been generated by the gAI.

*Sebastian Fava
Hamburg, den 23/09/2024*

Unterschrift der Doktorandin / des Doktoranden

*Dedicated to all those people who, through sacrifices in their lives,
enable future generations to pursue their natural aspirations.*

Abstract

In recent years, strongly correlated materials have emerged as promising candidates for hosting next-generation technologies. Due to their rich phase diagrams featuring different competing orders, their macroscopic properties can be controlled on demand with tailored external stimuli. In particular, the development of intense ultrafast light sources in the mid-infrared and terahertz regime enabled the direct and efficient coupling to the low-energy tuning knobs of these quantum solids. Experiments in this novel field have confirmed the generation of transient ferroelectric, magnetic, topological, and superconducting orders.

Cuprate superconductors are the archetypical member of this class of materials, wherein antiferromagnetism, superconductivity, charge and spin order interchange with moderate tuning of the carrier doping or crystal lattice. Remarkably, in underdoped $\text{YBa}_2\text{Cu}_3\text{O}_{7-\delta}$, signatures of incoherent superconducting fluctuations are present above T_c , extending up to and above room temperature. The most accepted interpretation postulates that superconductivity exists locally in this pseudogap phase, and fluctuations prevent the emergence of long-range order. These observations have sparked a series of experiments aimed at resurrecting the superconducting state by directly driving the inter-layer coupling of this layered compound, conjectured as the determining factor for the superconducting pairing. These expectations were positively met by experiments where transient optical properties reminiscent of equilibrium superconductivity were observed in terahertz time-domain spectroscopy.

However, these findings were not conclusive since they were also compatible with a non-superconducting state with enhanced mobility. In order to clarify the nature of the photo-excited state, it was paramount to verify whether it presented the dynamical equivalent of a Meissner effect, considered a fingerprint of the macroscopic coherence characterizing the superconducting order. However, prior to this work, no experimental study had interrogated the magnetic properties of this exotic transient state.

Here, we set out to address this fundamental question. The core of the investigation revolved around the development of the novel Ultrafast Magnetometry experimental technique, combining elements of magneto-optic imaging with the sampling of terahertz pulses. The diamagnetic response of the superconductor was detected by measuring the spatial profile of the magnetic field in its surroundings. Improving on previous designs, the adoption of diamagnetic detectors and advanced analysis techniques made it possible, for the first time, to follow the magnetic dynamics associated with the onset of superconductivity with ~ 1 ps time-resolution and ~ 1 μT sensitivity.

This experimental technique revealed the presence of a sizable magnetic field expulsion in $\text{YBa}_2\text{Cu}_3\text{O}_{6.48}$ upon photo-excitation. Quasi-static simulations confirmed that the sampled magnetic field was caused by a colossal diamagnetic response $\chi \sim -0.3$, reproduced at equilibrium only by type-II superconductors. This observation is incompatible with a photo-induced increase in mobility. Rather, it underscores the onset of superconducting coherence over macroscopic length scales. Remarkably, the effect was seen to persist up to room temperature and correlated positively with the terahertz optical measurements, suggesting a common physical origin for these two different observables. These experimental findings support the picture of a pseudogap phase in which incipient superconducting correlations are enhanced or synchronized by the drive.

Zusammenfassung

In den letzten Jahren haben stark korrelierte Materialien großes Potenzial als Kandidaten für die nächste Generation von Technologien gezeigt. Aufgrund ihrer reichen Phasendiagramme, die verschiedene konkurrierende Ordnungen aufweisen, können ihre makroskopischen Eigenschaften nach Bedarf mit maßgeschneiderten externen Stimuli verändert werden. Insbesondere die Entwicklung intensiver ultraschneller Lichtquellen im mittleren Infrarot- und Terahertzbereich ermöglicht die direkte und effiziente Kopplung an die niederenergetischen Stellschrauben dieser Quantenmaterialien. Experimente in diesem neuen Bereich bestätigten die Erzeugung transientser ferroelektrischer, magnetischer, topologischer und supraleitender Ordnungen.

Cuprat-Supraleiter sind das archetypische Mitglied dieser Materialklasse, in denen Antiferromagnetismus, Supraleitung, Ladungs- und Spinordnung durch eine moderate Anpassung der Trägerdotierung oder des Kristallgitters wechseln. Bemerkenswerterweise zeigen unterdotierte YBCO-Proben Anzeichen von inkohärenten supraleitenden Fluktuationen oberhalb von T_c , die sich bis hin zu und über Raumtemperatur erstrecken. Die am weitesten akzeptierte Interpretation dieses Phänomens postuliert, dass die Supraleitung lokal in dieser "Pseudogap"-Phase existiert, aber Fluktuationen das Entstehen einer langreichweitigen Ordnung verhindern. Diese Beobachtungen lösten eine Reihe von Experimenten aus, die darauf abzielen, den supraleitenden Zustand wiederherzustellen, indem die Interlayer-Kopplung dieses in Schichten aufgebauten Materials direkt angesteuert wird, die als der entscheidende Faktor für den supraleitenden Zustand vermutet wird. Die ersten Experimente in der Terahertz-Zeitbereichsspektroskopie bestätigten diese Vermutung, bei denen transiente optische Eigenschaften beobachtet wurden, die denen der Gleichgewichts-Supraleitung ähneln.

Diese Ergebnisse waren jedoch nicht schlüssig, da sie auch mit einem nicht-supraleitenden Zustand mit erhöhter Mobilität vereinbar waren. Um die Natur des photoangeregten Zustands zu klären, war es entscheidend, zu überprüfen, ob er das dynamische Äquivalent eines Meissner-Effekts aufwies, der als Fingerabdruck der makroskopischen Kohärenz gilt, die den supraleitenden Zustand charakterisiert. Vor dieser Arbeit hatte jedoch keine experimentelle Studie die magnetischen Eigenschaften dieses exotischen transienten Zustands untersucht.

Hier gehen wir dieser fundamentalen Frage nach. Im Zentrum der Untersuchung steht die Entwicklung einer neuartigen experimentellen Technik der Ultraschnellen Magnetometrie, die Elemente der magneto-optischen Bildgebung mit der Abtastung von Terahertz-Pulsen kombiniert. Die diamagnetische Antwort des Supraleiters wurde durch die Messung des räumlichen Profils des umgebenden Magnetfelds detektiert. Durch Verbesserungen von früheren Designs, insbesondere die Verwendung von diamagnetischen Detektoren und fort-

schrittlichen Analysetechniken, war es erstmals möglich, die magnetische Dynamik, die mit dem Einsetzen der Supraleitung verbunden ist, mit einer Zeitauflösung von ~ 1 ps und einer Sensitivität von ~ 1 μ T zu verfolgen.

Diese experimentelle Technik erlaubte den Nachweis der Anwesenheit einer beträchtlichen Magnetfeldverdrängung in YBCO nach Photoanregung. Quasistatische Simulationen bestätigten, dass das abgetastete Magnetfeld durch eine kolossale diamagnetische Antwort von $\chi \sim -0.3$ verursacht wurde, die im Gleichgewicht nur von Typ-II-Supraleitern reproduziert wird. Diese Beobachtung ist nicht mit einer photoinduzierten Erhöhung der Mobilität vereinbar, sondern unterstreicht das Einsetzen der supraleitenden Kohärenz über makroskopische Längenskalen hinweg. Bemerkenswerterweise wurde festgestellt, dass der Effekt bis hin zur Raumtemperatur anhielt und positiv mit den Terahertzoptischen Messungen korrelierte, was auf einen gemeinsamen physikalischen Ursprung dieser beiden unterschiedlichen Beobachtungen hindeutet. Diese experimentellen Befunde unterstützen das Bild einer Pseudospaltphase, in der beginnende supraleitende Korrelationen durch die Anregung verstärkt oder synchronisiert werden.

Contents

Introduction	1
1 Magnetic properties of superconductors	7
1.1 Phenomenology of Superconductivity	7
1.1.1 Persistent currents	7
1.1.2 Meissner effect	7
1.1.3 Shielding currents	9
1.1.4 Zero-field cooled and in-field cooled superconductors	10
1.1.5 Demagnetizing fields	11
1.2 Spatial distribution of magnetic fields surrounding superconductors	13
1.3 London's theory	15
1.3.1 Rigidity of the superconducting state	16
1.4 Ginzburg-Landau theory	17
1.4.1 Free Energy functional	17
1.4.2 Spatial gradients	18
1.4.3 Magnetic fields	19
1.4.4 Type-I and Type-II superconductors	21
1.4.5 Fluxoid quantization	22
1.4.6 Anisotropic formulation	24
1.4.7 Time-dependent formulation and vortex motion	24
1.5 Fluctuations above critical temperature	25
1.5.1 Gaussian fluctuations	25
1.5.2 BKT instability	27
2 The unconventional Superconductor $\text{YBa}_2\text{Cu}_3\text{O}_{7-\delta}$	29
2.1 Crystal Structure and lattice modes	30
2.1.1 Infrared active modes in $\text{YBa}_2\text{Cu}_3\text{O}_{6.5}$	31
2.1.2 Transient displacement of the lattice via nonlinear phononics	31
2.2 Phase diagram and electronic properties	34
2.2.1 Fluctuations in the pseudogap phase	36
2.3 Superconducting signatures in THz reflectivity	38
2.4 Ultrafast control of superconductivity	40
2.4.1 Disruption of superconductivity with optical pulses	40
2.4.2 Light-induced superconductivity	41
2.4.3 Pump frequency dependence	42

2.4.4	Josephson plasmons amplification	43
3	Ultrafast Optical Magnetometry	47
3.1	Origin of the Faraday effect	47
3.1.1	Ferrimagnetic, diamagnetic, and paramagnetic detectors	49
3.1.2	Frequency dependence of the Verdet constant	51
3.2	Magneto-optic sampling	51
3.2.1	Reflection and transmission configurations	52
3.2.2	Polarization analysis	54
3.2.3	Suppression of spurious contributions	55
3.2.4	Polarization dependence	57
3.2.5	Reconstruction of the full polarization state	58
3.3	Spatial resolution	61
3.3.1	Equilibrium measurements of $\text{YBa}_2\text{Cu}_3\text{O}_7$ thin films	63
3.3.2	Superconducting transition	64
3.3.3	Spatial dependence	65
3.4	Time resolution	66
3.4.1	Dynamical measurements of $\text{YBa}_2\text{Cu}_3\text{O}_7$ thin films	68
4	Magnetic properties of equilibrium and driven $\text{YBa}_2\text{Cu}_3\text{O}_{6.48}$	71
4.1	Sample and detector arrangement	71
4.2	Equilibrium measurements	72
4.2.1	Spatial dependence	73
4.2.2	Applied magnetic field dependence	73
4.3	Driven magnetic field expulsion	74
4.3.1	Spatial dependence	77
4.3.2	Probe pulse polarization dependence	77
4.3.3	Applied magnetic field dependence	78
4.3.4	Fluence dependence	78
4.3.5	Temperature dependence	79
4.4	Magnetic field propagation	80
	Conclusions	83
	A Sample growth and characterization	85
	B Light sources and signal acquisition	87
	C Data acquisition and analysis	91
	D Quasi-static magnetic simulations	93
	Bibliography	97
	Acknowledgements	103

List of Figures

1	Non-thermal pathways due to laser drive	1
2	First studies of light-induced superconductivity	2
3	Magneto Optical Image of superconducting vortex array	4
1.1	Persistent currents	8
1.2	The Meissner effect	9
1.3	ZFC vs FC states in a disk	11
1.4	ZFC vs FC states in a ring	12
1.5	Magnetostatic simulation of field expulsion	14
1.6	Ginzburg-Landau coherence length	19
1.7	Flux quantization	23
1.8	BKT transition	28
2.1	Crystal structure of $\text{YBa}_2\text{Cu}_3\text{O}_{7-\delta}$	29
2.2	Crystal structure of $\text{YBa}_2\text{Cu}_3\text{O}_{6.5}$	30
2.3	Infrared active modes of $\text{YBa}_2\text{Cu}_3\text{O}_{6.5}$	32
2.4	Infrared and Raman phonon modes	32
2.5	Atomic displacement in nonlinear phononics	34
2.6	Phase diagram of $\text{YBa}_2\text{Cu}_3\text{O}_{7-\delta}$	35
2.7	Effect of fluctuations on high- T_c cuprates	37
2.8	THz optical features of equilibrium $\text{YBa}_2\text{Cu}_3\text{O}_{6.5}$	39
2.9	Ambiguity of THz measurements.	40
2.10	Optical properties of disruption of superconductivity	41
2.11	Optical properties of enhancement of superconductivity	41
2.12	Pump frequency dependence of optical properties of $\text{YBa}_2\text{Cu}_3\text{O}_{6.5}$	43
2.13	Amplification of Josephson plasmon modes	44
2.14	Temperature dependence of Josephson amplification	45
3.1	Verdet constant in GaP	50
3.2	Material dependence of Verdet constant	51
3.3	Frequency dependence of Verdet constant	52
3.4	Transmission and reflection configuration for MOS	53
3.5	Polarization analysis for MOS	54
3.6	Experimental configuration to minimize spurious contributions	56
3.7	Polarization dependence of the Faraday and Pockels effect	58
3.8	Spatial resolution in MOS	63

3.9	MOS characterization: sample detector geometry dependence	63
3.10	MOS characterization: superconducting transition	64
3.11	MOS characterization: spatial dependence	65
3.12	Temporal resolution in MOS	67
3.13	MOS characterization: temporal dependence dynamics	69
3.14	MOS characterization: spatial dependence dynamics	70
4.1	Sample-detector arrangement	71
4.2	Temperature dependence at equilibrium	72
4.3	Edge effect at equilibrium	73
4.4	Magnetic field dependence at equilibrium	74
4.5	Geometry of the experiment	75
4.6	Pump probe time dependence	76
4.7	Spatial dependence away from sample	76
4.8	Probe pulse polarization dependence	77
4.9	External magnetic field dependency	78
4.10	Fluence dependence	79
4.11	Time traces at different temperatures	79
4.12	Temperature dependence	80
4.13	Schematics of magnetic field pulse propagation	80
4.14	Magnetic field pulse propagation	81
4.15	Experimental configuration for thin $\text{YBa}_2\text{Cu}_3\text{O}_{6.48}$ lamella measurements	84
A.1	SQUID characterization of the sample	85
B.1	Experimental setup for thin-film measurements	88
B.2	Experimental setup for bulk measurements	90
C.1	Data acquisition scheme for $\text{YBa}_2\text{Cu}_3\text{O}_7$ measurements	91
C.2	Data acquisition scheme for $\text{YBa}_2\text{Cu}_3\text{O}_{6.48}$ measurements	92
D.1	Comparison between measured magnetometry data and simulations . .	94
D.2	Magnetic susceptibility estimates	95

Introduction

Control of Strongly Correlated Materials

Strongly correlated materials are the predominant focus of modern condensed matter research. In these systems, the electronic kinetic energy is comparable with the interaction energy associated with charge, spin, orbital, and lattice degrees of freedom. As a consequence, different ground states, with different and often competing types of orders, are frequently found close in energy. The delicate balance between them can be toppled with a moderate external stimulus. For example, hydrostatic pressure can induce the transition from a Mott-insulator to a Weyl semimetal by enhancing the overlap between electronic wavefunctions [1], or an intense magnetic field can suppress the superconducting state in favor of a charge-density order [2].

The development of ultrashort light sources was a successful addition to the field, making it possible to induce transitions over significantly shorter time scales. Recent applications in this field go beyond simply melting the thermal state. In these cases, the process cannot be described by the conventional two-temperature model [3], wherein the transient properties are accounted for by a heating of the electronic subsystem. Rather, the use of intense light sources widely tunable from the ultraviolet to the terahertz regime made it possible to selectively drive only the degrees of freedom relevant to the desired transition. This approach explores non-thermal pathways and offers the potential for reaching new states not available at equilibrium [4]. For example, mid-infrared radiation resonant to a specific phonon mode in SrTiO₃ was shown to induce a metastable transition to a ferroelectric state not present at equilibrium [5].

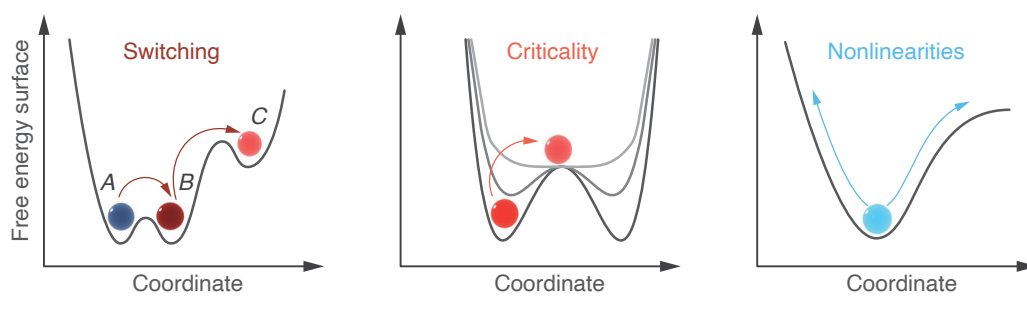


FIGURE 1: Illustration of possible non-thermal mechanisms upon laser excitation. Adapted from [4].

This idea is illustrated in the first panel of Figure 1, where the intense drive can induce *switching* to degenerate or metastable states. A complementary description is shown in the second panel, where the drive induces a deformation of the free energy landscape and, in particular conditions, *critical behavior*. The last panel depicts how the resonant excitations of specific modes can drive the coordinate to high amplitudes

and trigger *nonlinear dynamics*, where additional couplings between modes are available. In experiments involving strongly correlated systems, all these effects are often realized simultaneously.

Light-induced Superconductivity

Superconductors are among the most studied quantum materials, given the potential they host in future technological applications. Considerable effort has been invested into synthesizing superconductors with ever-increasing critical temperatures. An alternative approach relies on selectively photo-exciting existing systems to favor the superconducting pairing and increase their critical temperature. This may sound counter-intuitive at first since injecting energy into a material will, in general, increase its temperature and hinder superconductivity. The key lies in efficiently coupling to specific degrees of freedom and studying the out-of-equilibrium dynamics that ensue after photo-excitation before the system has thermalized.

This ambitious goal was first applied to the study of the single-layer cuprate $\text{La}_{1.8-x}\text{Eu}_{0.2}\text{Sr}_x\text{CuO}_4$. In this compound, superconductivity is quenched for lower dopings ($x < 0.2$), where a competing stripe order emerges (see diagram in Figure 2). This 1-dimensional modulation of spin and charge is associated with a low-temperature tetragonal (LTT) lattice distortion, as shown in the inset. In the parent compound $\text{La}_2\text{Sr}_{2-x}\text{CuO}_4$, this distortion is less pronounced, and superconductivity is retained for higher temperatures (see orange dashed line in the phase diagram).

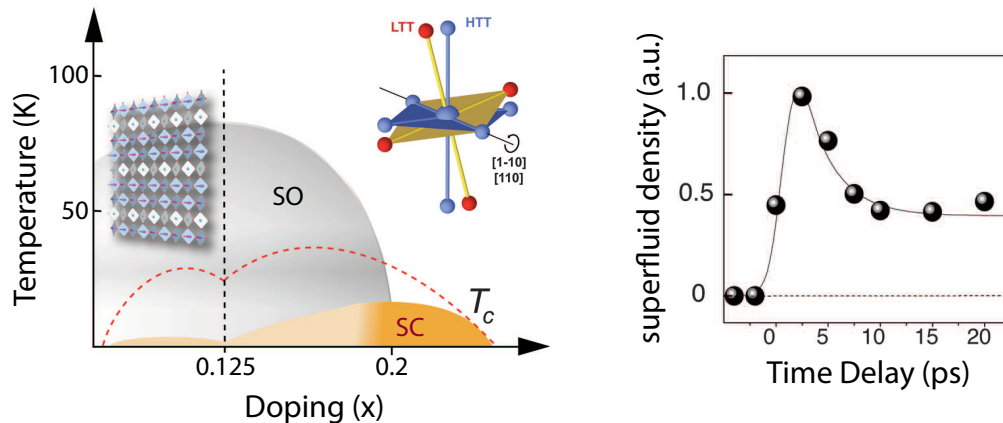


FIGURE 2: First studies of light-induced superconductivity in $\text{La}_{1.8-x}\text{Eu}_{0.2}\text{Sr}_x\text{CuO}_4$ employing terahertz reflectivity to reconstruct the transient optical properties. SC: superconductivity, SO: stripe order. Adapted from [6].

An experiment was performed in the stripe-ordered $\text{La}_{1.675}\text{Eu}_{0.2}\text{Sr}_{0.125}\text{CuO}_4$ ($x = 0.125$) at a base temperature of 10 K. The goal was to induce a transition to the high-temperature tetragonal (HTT) phase, where superconductivity is expected to be more favorable, by selectively driving the lattice mode linked to the LTT with mid-infrared

radiation. The dynamics was observed with time-domain terahertz spectroscopy. As will be discussed in more detail in a dedicated section in Chapter 2, this technique provides a measurement of the transient superfluid density of the system, which is used as a figure of merit for the superconducting state. This quantity is plotted on the right of Figure 2 as a function of delay with respect to the mid-infrared photo-excitation, which drives the sample at time zero. The transient detection of a finite superfluid density provided the first indication compatible with the induction of a superconducting state.

Qualitatively similar transient optical features were later obtained in the stripe-ordered phase of $\text{La}_{2-x}\text{Ba}_x\text{CuO}_4$ [7, 8], and extended even to organic compounds, such as the charge-transfer salt $\kappa\text{-(BEDT-TTF)}_2\text{Cu[N(CN)}_2\text{]Br}$ [9, 10] and the alkali-doped fullerene K_3C_{60} [11, 12, 13]. These experiments sparked the novel field of *light-induced superconductivity*.

In related investigations, particular attention has been dedicated to the bilayer cuprate $\text{YBa}_2\text{Cu}_3\text{O}_{7-\delta}$ [14, 15, 16, 17], where superconductivity is not induced starting from a sharply distinct competing order, but rather from a pseudogap phase, where partial signatures reminiscent of superconductivity are still present. Remarkably, these features are detected up to and above room temperature, prompting the search for a room-temperature superconducting state, albeit transient. This promising yet poorly understood material will be the central subject of this thesis work.

Why are magnetic measurements crucial?

Up to now, light-induced superconductivity has been uniquely investigated with time-domain terahertz spectroscopy. The reason is twofold. First, terahertz (THz) frequencies are well-suited for studying the low-energy properties of the superconducting state. Second, THz pulses can be easily integrated into a pump-probe setup, offering the time resolution required for ultrafast studies. However, the crucial limitation of this technique is that it only measures the conductivity of the system. As such, it cannot distinguish a transient superconducting state from a transient metallic state with a significantly enhanced scattering time (see discussion in Section 2.3). Due to this ambiguity, another experimental tool more sensitive to the superconducting properties was highly required.

The Meissner effect, wherein a static magnetic field is expelled from the interior of a material, originates from the macroscopic coherence typical of superconductors. It is widely recognized as a cornerstone of superconductivity and is the ideal indicator of this correlated state. The standard approach to observe its onset is the measurement of the sample magnetization. Commercial superconducting quantum devices (SQUID) can measure magnetic moments with unparalleled resolution and have been established as the preferred technique by most experimentalists to detect superconductivity. Unfortunately, it does not offer the time resolution required to track ultrafast dynamics.

An alternative solution is *optical magnetometry*. In this case, the magnetic field inside a detection crystal is encoded in the polarization state of an optical beam traversing it and then quantified by conventional polarization analysis techniques. The detector is then placed in proximity to the sample, to measure the magnetic field due to its magnetization. Using short pulses as probe beams makes it possible to achieve the time resolution required for ultrafast studies. Additionally, by scanning the probe beam, it is possible to retrieve the magnetic field distribution inside the sample or in its proximity. For example, Figure 3 shows an ensemble of pinned vortices in a thin film of Nb.

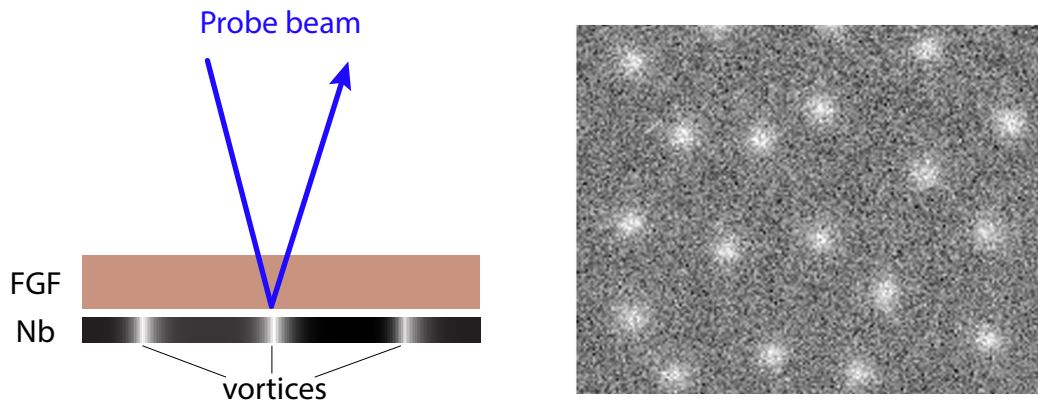


FIGURE 3: Magneto Optical Image of superconducting vortex array in a Nb thin film measured in an adjacent Ferrite Garnet Film (FGF). The color scale represents the different amplitudes of the sampled magnetic field. Data adapted from [18].

Despite the promising time resolution, the fastest superconducting magnetic field dynamics found in literature is of order 100 ps^1 , a hundred times slower than the expected onset of light-induced superconductivity [19]. The bottleneck in the time resolution did not lie in the probe pulse duration but in the response time of the detectors. In order to maximize efficiency, magnetically ordered materials are commonly employed. However, the same magnetic order is also the cause of the slower response time offered.

This thesis work has been dedicated to overcoming this fundamental limitation by employing diamagnetic detectors, which offer the picosecond time resolution required for ultrafast studies. Their implementation has not been straightforward since the significantly lower resolution required advanced techniques of polarization analysis typically not needed with traditional ferrimagnetic detectors. These efforts were fruitful. For the first time, the ultrafast magnetic properties of driven $\text{YBa}_2\text{Cu}_3\text{O}_{7-\delta}$ have come to light.

¹This was enough to justify paper titles including the term “picosecond studies”.

Thesis outline

Chapter 1 reviews the characteristic magnetic properties of superconductors. Particular emphasis is placed on the derivations of the distribution of magnetic fields due to the superconducting diamagnetic response. This notion will prove crucial in the interpretation of magnetometry data. A discussion on the possible mechanisms responsible for the superconducting condensate instability is also included, which will be applied to the phase diagram of $\text{YBa}_2\text{Cu}_3\text{O}_{7-\delta}$.

Chapter 2 introduces $\text{YBa}_2\text{Cu}_3\text{O}_{7-\delta}$, the cuprate compound that has been the subject of this thesis work. First, its equilibrium crystal structure is presented alongside the techniques of nonlinear phononics employed to deform it transiently. The discussion follows with an overview of its phase diagram, where all the competing orders present in this compound are briefly introduced. Finally, the notion of light-induced superconductivity in this compound is presented. The interpretations of the THz time-domain reflectivity experiments and their limitations are discussed in detail.

Chapter 3 presents the development of the Ultrafast Magnetometry experimental technique. First, the origin of the Faraday effect is reviewed, with considerations relevant to the correct choice of Faraday detector. Second, the practical implementation of an optical-magnetometry setup is discussed in detail, including a discussion on advanced analysis techniques to recover the full polarization state of the probe beam. Finally, the spatial and temporal resolutions of the techniques are discussed, with characterization experiments performed on thin films of optimally-doped $\text{YBa}_2\text{Cu}_3\text{O}_7$.

Chapter 4 applies the Ultrafast Magnetometry technique to the study of photo-excited $\text{YBa}_2\text{Cu}_3\text{O}_{6.48}$. First, the equilibrium magnetic properties are presented, including a comparison with more conventional magnetic probes. Subsequently, a broad set of dependencies in the transient state and their relevance is discussed. Finally, experiments related to the dynamical propagation of the magnetic signal are presented. The interpretation of the experimental data and the future outlooks are discussed in the Conclusions.

Chapter 1

Magnetic properties of superconductors

Superconductivity is a fascinating physical phenomenon that has attracted the attention of condensed matter physicists since its discovery in 1911 by H. Kamerlingh Onnes [20]. Its charm lies in the macroscopic manifestation of quantum properties normally absent in everyday life. These properties are embodied by a resistivity that falls to exactly zero and by the expulsion of a static magnetic field. The latter property will be the focus of the current chapter.

1.1 Phenomenology of Superconductivity

1.1.1 Persistent currents

The name “superconductor” originates from the property of sustaining an electrical current with significantly less resistance than a regular conductor. This effect is so striking that it is quite challenging, experimentally, to put an upper bound on the value of resistivity for these materials. The conventional technique relies on inductively starting a current I in a superconducting ring and then measuring its evolution as a function of time (see Figure 1.1).

The current has an initial value I_0 , and once the drive is over, it follows an exponential decay of the form $I_0 e^{t/\tau}$. Here, τ defines the characteristic decay time of the induced current. From this quantity, one can estimate an upper bound on the resistivity of the material. In superconductors, this was shown to be as low as $10^{-21} \Omega \text{ m}$ [21]. As a comparison, the resistivity for gold at low temperatures is $\sim 2.4 \times 10^{-8} \Omega \text{ m}$.

1.1.2 Meissner effect

Faraday-Lenz law states that a conductor builds up a current in response to a *changing* magnetic field to counteract changes of the latter in its interior. This *eddy currents* are effective at screening magnetic field changes only for a time proportional to their decay time. In the case of superconductors, given their extremely long decay times (or, equivalently, their vanishing resistivity), it immediately follows that the magnetic field is constant in time within the material. Contrary to a common misconception,

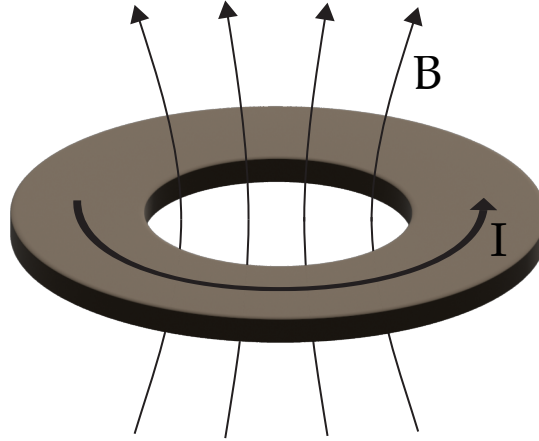


FIGURE 1.1: Persistent currents inductively induced in a superconductor.

this is *not* the Meissner effect but rather a consequence of the vanishing resistivity of the superconductor.¹

The following thought experiment can capture the key distinction between a state of matter with zero resistivity and a superconductor. Place a material at high temperature inside a coil and turn on a steady current to apply a static magnetic field. If the material is a conductor, it builds up eddy currents to slow down the changes in the magnetic field in its interior. After a finite amount of time, those eddy currents completely decay, and the statically applied magnetic field traverses the material. Cool the sample below a certain critical temperature, which induces a phase transition. Even if this new phase is characterized by a vanishing resistivity, we do not expect it to expel the external magnetic field since conductors only respond to changing magnetic fields, as mentioned above (see Figure 1.2, left). Instead, the superconductor does respond to the static magnetic field and expel it from its interior (see Figure 1.2, right). As discussed in the following sections, this is a consequence of the macroscopic quantum coherence of the superconducting state.

Assuming as constitutive relation for the material

$$\mathbf{B} = \mu_0(\mathbf{H} + \mathbf{M}) = \mu_0\mathbf{H}(1 + \chi) \quad (1.1)$$

where χ is its magnetic susceptibility, it immediately follows that the Meissner effect implies a χ of -1 . A negative χ means that superconductors are diamagnetic. Furthermore, this value of χ is the minimum compatible with thermodynamic equilibrium. Superconductors are therefore said to be *perfect diamagnets*.

¹This confusion often leads to erroneously associating the divergence in the imaginary part of the optical conductivity to the Meissner effect. This is not correct. As discussed in 2.3, the latter is indicative of dissipationless transport. In order to directly probe the Meissner effect, a technique sensitive to the magnetic properties of the superconductor is crucial.

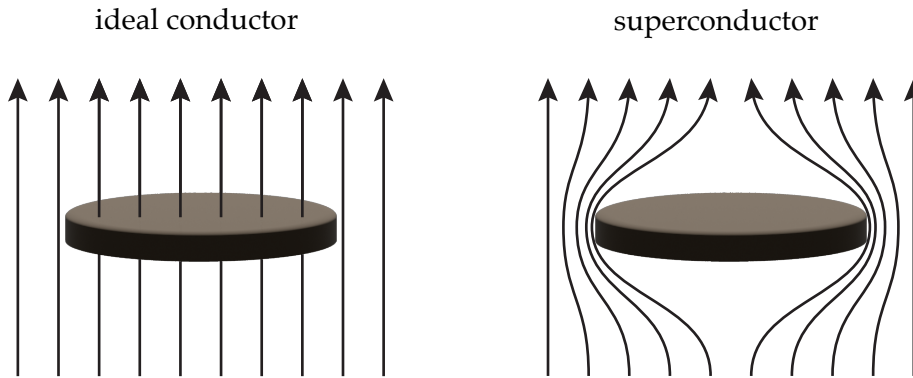


FIGURE 1.2: The Meissner effect, the hallmark property of superconductivity, is the expulsion of a static magnetic field from the interior of the medium (right). An ideal conductor with vanishing resistivity does not respond to static magnetic fields (left). Arrows represent magnetic field lines.

1.1.3 Shielding currents

Let us consider for simplicity the case of an infinitely long cylinder² embedded in an external magnetic field $\mathbf{B}_0 = \mu_0 \mathbf{H}_0$ directed along its length. In this geometry, all the fields are along the same direction and can be treated as scalars. From the continuity equations for the \mathbf{H} field (the component parallel to the interface has to be continuous), it immediately follows that \mathbf{H} is uniform in all space as $\mathbf{H} = \mathbf{H}_0$.

In order to shield the \mathbf{B} field, it follows from the constitutive relation 1.1 that inside the superconductor the magnetization \mathbf{M} is uniform and opposite to \mathbf{H} , so that $\mathbf{M} = -\mathbf{H}_0$. From Ampère's law, considering that $\nabla \times \mathbf{H} = 0$, it follows that

$$\nabla \times \mathbf{B} = \mu_0 \nabla \times \mathbf{M} = \mu_0 \mathbf{J}_{sh} \quad (1.2)$$

where J_{sh} represents the *shielding current density* of the superconductor.

Deep inside the superconductor, \mathbf{M} is uniform. Therefore, $\mathbf{J}_{sh} = 0$. This is expected since a non-zero current necessarily implies a finite magnetic field. The shielding current is then localized at the edge of the superconductor.

In Section 1.3, we will see that the magnetic field, and consequently the shielding current, actually penetrates inside the superconductor over a characteristic length λ . This finite penetration makes the magnetization \mathbf{M} non-homogenous in that region. However, λ is typically of order ~ 100 nm and is often neglected in calculations involving bulk samples. To good approximation, the field due to the presence of the

²This shape allows us to neglect the complications associated with demagnetizing fields. These effects are, however, relevant for this thesis work and will be discussed in Subsection 1.1.5.

superconductor can be modeled as that generated by a uniformly magnetized body with $\chi = -1$.

1.1.4 Zero-field cooled and in-field cooled superconductors

In practice, the superconductor is far from the ideal cylinder presented in the previous subsection. For example, point defects in the crystal create regions of normal material where the field does not have to be excluded entirely. These imperfections can be modeled as a superconducting ring, with either a vacuum or a normal region within its center. Either of the two does not respond to magnetic fields, so we assume to have a vacuum for simplicity. The dimension of this hole also makes little difference. It could be a few atomic lattices wide or extend over macroscopic distances.

This different topology for the superconducting phase leads to significant differences in the response to an external magnetic field. Contrary to the case discussed in Subsection 1.1.2, the final state depends not only on the value of temperature and of the applied field but also on the *order* in which these two were applied. This characteristic is not exclusive to superconductors and is observed in all those systems that present hysteresis, most notably in ferromagnets.³

We start from the simplest case: an ideal superconductor without holes nor imperfections. As shown in Figure 1.3, whether the system is first subject to the external magnetic field and cooled below T_c or vice versa does not make a difference. The final state, with the entirety of the magnetic field expelled from its interior, is the same.

The situation differs for the ring geometry shown in Figure 1.4. In this case, if we first cool down the material and then apply the external field, we reach the so-called *zero field cooled* (ZFC) state. In this state, the field is expelled both from the superconducting region and from the hole at its center. The physical origin is the Faraday-Lenz law applied to an ideal conductor. The shielding current that builds up to prevent a change in the magnetic field flux in the sample interior never decays. Therefore, the field is *excluded* from the whole area of the system. As mentioned in Subsection 1.1.2, this exclusion does not rely on the Meissner effect but rather on the perfect conductivity of the superconducting ring.

On the other hand, if we first apply a static field and then cool down the system, we reach the *field cooled* (FC) state, where the magnetic field is *expelled*⁴ only from the superconducting region. This expulsion is a consequence of the Meissner effect since it would not happen in an ideal conductor. Interestingly, the system builds up shielding

³More generally, any broken-symmetry phase can potentially host this feature. This is a direct consequence of the ground state having a lower symmetry than the system itself. The direction in which the symmetry is lowered is either random or dependent on the history of the system. As discussed in Section 1.4, the superconducting state breaks a global U(1) symmetry by acquiring a macroscopic phase for its order parameter. In non-simply connected topologies such as the ring shown in the figure, the winding of the phase around the loop determines the magnetic flux through the ring. Each integer number of winding corresponds to a different but equally possible state. Determining which one is actually realized depends on the history of the system.

⁴Note the different terminology to highlight the different physical origins: field “exclusion” refers to the field excluded by the ideal conductor response case and field “expulsion” to the field expelled by the Meissner effect. In practice, the latter may be used for both without distinction.

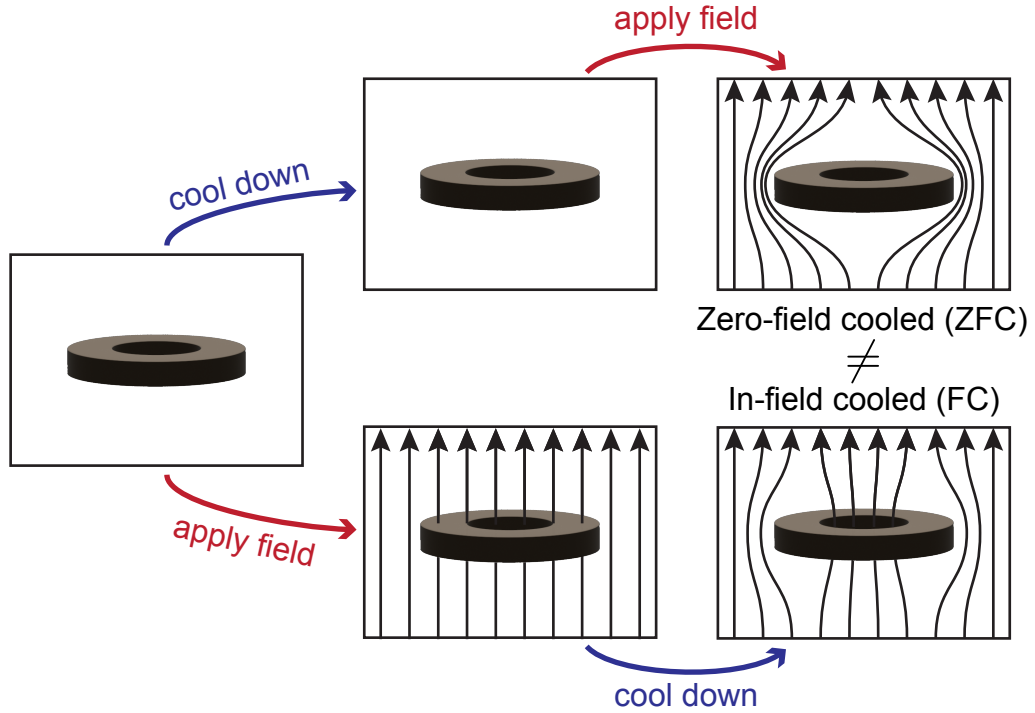


FIGURE 1.4: For a superconductor with imperfections, the ZFC state (first cooled down and then subject to a field) expels more field than the FC state (subject to a field first, then cooled down). Which state is reached then depends on the history of the system.

field \mathbf{H}_d , adds on top of the external one as

$$\mathbf{H} = \mathbf{H}_0 + \mathbf{H}_d \quad (1.3)$$

\mathbf{H}_d is generally non-uniform and hard to compute. For the simple case of ellipsoids with a field applied along one of its principal axes, it can be shown [23] that a simple relation exists between applied and internal fields. In this case, the internal magnetization is uniform, and the fields, all pointing along the same axis, can be treated as scalars. Then, the demagnetizing field is proportional to the magnetization as

$$\mathbf{H}_d = -NM \quad (1.4)$$

where N is a constant between 0 and 1 that depends on the geometry. For a sphere, $N = 1/3$. If the principal axes have different lengths, N is higher if the field is applied along the shortest and lower if along the longest. The negative sign justifies the term “demagnetizing” since \mathbf{H}_d is directed against the internal magnetization.⁷

⁷This term originated in the context of ferromagnets, wherein the induced magnetization usually points along the external bias \mathbf{H}_0 .

Summing both external and internal contributions, the magnetization amounts to

$$\mathbf{M} = \mathbf{H}_0 \frac{\chi}{1 + \chi N} \quad (1.5)$$

For positive χ , such as in ferromagnets, the demagnetizing field is directed opposite to the magnetization and, consequently, effectively works against the applied field. In contrast, in superconductors, where χ is negative, the demagnetizing field enhances the effect of the applied field.⁸ Assuming an ideal superconductor with $\chi = -1$, from Equation 1.5 we see that the internal field is increased by $\frac{1}{1-N}$. This factor has to be accounted for when investigating the properties of a superconductor, such as critical field and susceptibility, with a given external field.

1.2 Spatial distribution of magnetic fields surrounding superconductors

The presence of the superconductor strongly affects the magnetic field in its surroundings. Thus, sampling the magnetic field is a great diagnostic tool for superconductivity. In this brief section, we visualize these changes by solving simple models to build a physical intuition for experiments.

We want to solve the magneto-static problem for a magnetizable object (the superconductor) embedded in an external field. We start by writing the Maxwell equations in a medium to include the response of the system, where we drop all time-dependent terms since we are interested in the steady-state solution. Furthermore, we assume there are no free currents. In this limit, the magnetic and electric variables are independent, and we can focus only on the former

$$\begin{aligned} \nabla \cdot \mathbf{B} &= 0 \\ \nabla \times \mathbf{H} &= 0 \end{aligned} \quad (1.6)$$

with the constitutive relation 1.1.

The external field is included by imposing, as a boundary condition, that the \mathbf{H} field far away from the magnetizable sample has to be equal to the applied field \mathbf{H}_0 . This assumption is justified for distances much greater than the sample dimensions where the demagnetizing field is negligible.

⁸To give an intuitive picture of the effect of demagnetizing fields, it helps to consider the medium as composed of separated regions, each generating a magnetic field due to a point-like magnetic dipole. The demagnetizing field is the field felt by an individual region due to the presence of the neighboring dipoles. $N = 0$ (no demagnetizing field) corresponds to the arrangement where they are stacked in a line along the direction of the applied field (rod parallel to the field). In this case, the field due to opposite dipoles cancels, and the demagnetizing field is zero. $N = 1$ (strongest demagnetizing field) corresponds to the arrangement where they are stacked in a line perpendicular to the applied field (thin film perpendicular to the field). Contrary to the previous case, the fields of neighboring dipoles add, giving a strong contribution, which is important to account for in the analysis.

The system of Equations 1.6 can be solved numerically (see Appendix D). We consider a cylindrical sample to lower the computation times so that the problem possesses axial symmetry and the computed B field depends only on radial distance ρ and vertical distance z . The system parameters are the sample dimensions (radius and height) and its magnetic susceptibility. The latter can assume any value between -1 (ideal superconductor) and 0 (normal state with negligible susceptibility). The intermediate values are appropriate for type-II superconductors in their vortex state.

We present only the results obtained for the geometry relevant to this thesis work, which is a thin cylinder whose height ($2\ \mu\text{m}$) is much smaller than its diameter ($350\ \mu\text{m}$)⁹. An external magnetic field of $10\ \text{mT}$ is applied transversally along its axis. Figure 1.5 shows the differential field, that is, the field due to the magnetization of the superconductor. The field exclusion from the interior of the superconductor decreases the external field on the top of the sample and enhances it on its edges.

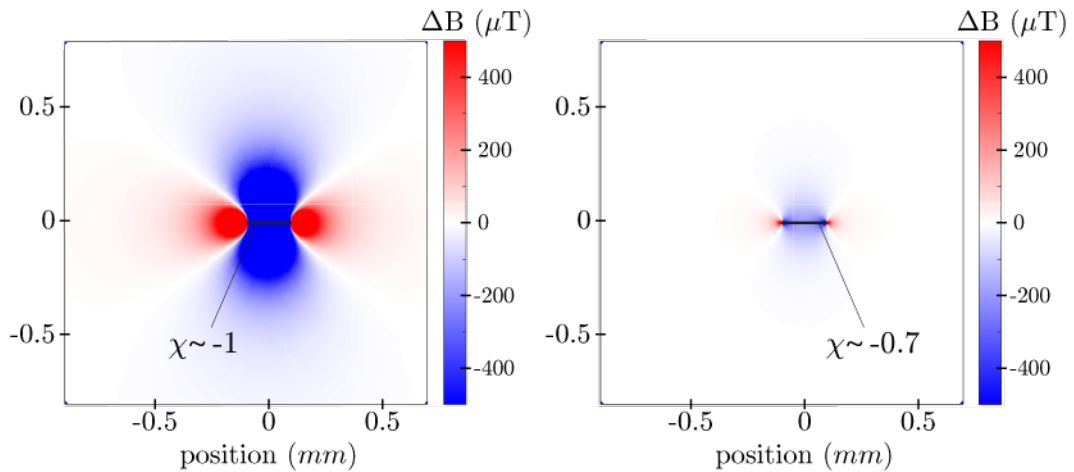


FIGURE 1.5: Magnetic field differential response of a thin superconductor (black) placed transversally to an external field of $10\ \text{mT}$. On top of the superconductor, the field is screened (blue region) and enhanced on the side (red region). The left panel shows an ideal superconductor with $\chi = -1$, and the right one a possible type-II superconductor in its vortex state with $\chi = -0.7$.

Two different magnetic susceptibilities are shown. On the left, $\chi = -1$ shows the case of an ideal type-I superconductor or type-II below its first critical field. This scenario presents the strongest response. On the right, $\chi = -0.7$ shows the case for a type-II superconductor in its vortex state. It is clear that, even for a slightly lower susceptibility, the field expulsion is much reduced compared to the ideal case.

⁹Note that, as discussed in Subsection 1.1.5, this is a highly unfavorable geometry for superconductivity, in which the demagnetizing factor significantly enhances the external field. Hence, for the validity of this analysis, it is essential to check whether the internal H field is still lower than the critical field.

1.3 London's theory

A first phenomenological theory accounting for the electrodynamic properties of superconductors was proposed by F. and H. London in 1935. This theory postulates that below some critical temperature T_c , the electronic transport is due to two separate fluids, referred to as normal (n_n) and superconducting (n_s), where n indicates their density, assumed to be uniform and stationary. This picture seemed plausible in view of Einstein's theory of Bose-Einstein condensation, but no justification on why the fermionic electrons should condense was provided.

The normal fluid follows Ohm's law

$$\mathbf{j}_n = \sigma_n \mathbf{E} \quad (1.7)$$

with Drude conductivity

$$\sigma_n = \frac{n_n e^2 \tau}{m} \quad (1.8)$$

where n_n , e , τ , and m represent the normal carriers' density, charge, scattering time, and mass, respectively.

The superfluid, instead, is assumed not to scatter, which leads to an inductive response

$$\frac{\partial \mathbf{j}_s}{\partial t} = \frac{n_s e^2}{m} \mathbf{E} \quad (1.9)$$

where we assume that the mass and the charge are the same as the normal carriers. This is the *First London Equation*. It shows that the superconducting response is purely inductive and proportional to the superfluid density n_s .

By taking the curl of Equation 1.9 and integrating in time, we obtain (using Faraday's law)

$$\nabla \times \mathbf{j}_s = -\frac{n_s e^2}{m} \mathbf{B} + \mathbf{C}(\mathbf{r}) \quad (1.10)$$

where the last term is an integration constant to be determined. To derive it, we assume that the material started with no currents and zero magnetic field inside. Hence, $\mathbf{C}(\mathbf{r}) \equiv 0$, which leads to the *Second London Equation*

$$\nabla \times \mathbf{j}_s = -\frac{n_s e^2}{m} \mathbf{B} \quad (1.11)$$

It is important to note that London theory, since it assumes a stationary superfluid density, cannot explain the Meissner effect. The latter is manifested by a field expulsion upon superconducting transition when the superfluid density goes from zero to a finite value. The London theory rather *assumes* the Meissner state as a starting point.

The main experimental prediction that follows can be obtained by taking the curl of Ampère's law and dropping off all time-dependent terms since we are interested in

the stationary case

$$\nabla \times \nabla \times \mathbf{B} = -\frac{\mu_0 n_s e^2}{m} \mathbf{B} \quad (1.12)$$

Since $\nabla \cdot \mathbf{B} = 0$, it follows that

$$\nabla^2 \mathbf{B} = \frac{1}{\lambda_L^2} \mathbf{B} \quad (1.13)$$

where we introduced the London penetration depth

$$\lambda_L := \sqrt{\frac{m}{\mu_0 n_s e^2}} \quad (1.14)$$

Let us solve this equation for a semi-infinite medium in the positive half of the x-axis. An external field $\mathbf{B}_0 = B_0 \hat{\mathbf{y}}$ is applied parallel to its surface. Inside the medium, the field decays as

$$\mathbf{B}(x) = B_0 e^{-x/\lambda_L} \hat{\mathbf{y}} \quad \text{for } x \geq 0 \quad (1.15)$$

The physical meaning of λ_L is the length over which the magnetic field penetrates inside the superconductor.

It is worth noting that in experiments, one often finds much longer penetration depths than what is expected from London theory. This deviation can be accounted for by introducing the notion of Pippard coherence length, which is connected to the non-locality of the superconducting response (see e.g. [24], Section 1.3).

The main shortcoming of London Theory is that it assumes n_s as spatially uniform and stationary. These constraints will be lifted in the Ginzburg-Landau theory introduced in Section 1.4.

1.3.1 Rigidity of the superconducting state

F. London provided a justification for the assumptions that led to the Second London Equation. First we combine the two London Equations 1.9 and 1.11 by introducing the vector potential \mathbf{A} , defined so that $\frac{\partial \mathbf{A}}{\partial t} = -\mathbf{E}$ and $\nabla \times \mathbf{A} = \mathbf{B}$

$$\mathbf{j}_s = -\frac{n_s e^2}{m} \mathbf{A} \quad (1.16)$$

Charge conservation requires $\nabla \cdot \mathbf{j}_s = 0$, which imposes the gauge choice $\nabla \cdot \mathbf{A} = 0$, referred to as London gauge in this context.

We now write the quantum mechanical expression for the current in zero field given the many-body wave function $\Psi_s(\mathbf{r}_1, \mathbf{r}_2, \dots)$ representing the superconducting stationary state.¹⁰ Assuming e as unit charge, we have

$$\mathbf{j}_s(\mathbf{r}) = \frac{e}{m} \sum_j \Re\{\langle \Psi_s^* | \mathbf{p}_j | \Psi_s \rangle\} \quad (1.17)$$

¹⁰This is a general quantum mechanical representation of a many-body state, which applies equally to superconductors and metals. It should not be confused with the Ginzburg-Landau treatment introduced in the next section, which assumes that all the superfluid particles condense in the same state.

The presence of the vector potential \mathbf{A} can be accounted for with the substitution $\mathbf{p}_j \rightarrow \mathbf{p}_j - e\mathbf{A}(\mathbf{r}_j) = -i\hbar\frac{\partial}{\partial\mathbf{r}_j} - e\mathbf{A}(\mathbf{r}_j)$. By splitting the kinetic and electromagnetic contributions, we obtain

$$\mathbf{j}_s(\mathbf{r}) = -\frac{e\hbar i}{m} \sum_j \Re\left\{\langle\Psi_s^*|\frac{\partial}{\partial\mathbf{r}_j}|\Psi_s\rangle\right\} - \frac{e^2 n_s}{m} \mathbf{A}(\mathbf{r}) \quad (1.18)$$

where n_s denotes the superfluid density.

Now, the steady-state Ψ_s depends, in general, on \mathbf{A} . The assumption advanced by London was that the stationary state Ψ_s is *rigid* under \mathbf{A} . This means that, to first order, Ψ_s *does not* depend on \mathbf{A} , in the gauge $\nabla \cdot \mathbf{A} = 0$. In this situation, it follows that the first term of Equation 1.18 represents the current flow of the stationary state Ψ_s for $\mathbf{A} \equiv 0$, and therefore vanishes.¹¹ Therefore, the expression for the current flow is equivalent to 1.16, and this assumption is sufficient to support the whole theory.

In the context of the Bardeen-Cooper-Schrieffer (BCS) theory, the rigidity of Ψ_s was later understood as the presence of a non-zero gap in the excitation spectrum of the superconducting wave function.

1.4 Ginzburg-Landau theory

Ginzburg-Landau's theory is a generalization of Landau's symmetry-breaking theory of phase transition. It is based on thermodynamical considerations and does not provide a microscopical justification for the onset of superconductivity. However, starting from very general considerations can lead to great physical insight.

1.4.1 Free Energy functional

We consider a complex order parameter ψ representing the macroscopic superconducting wave function. In the normal state $\psi = 0$. Below the critical temperature T_c , we expect an energetic gain by giving a finite amplitude to the order parameter.

We can formalize these concepts by writing the Free Energy functional $F[\psi]$, representing the system energy as a function of ψ . The ground state of the system is determined by the value of the order parameter that minimizes the Free Energy functional. Landau proposed that, close to the transition temperature above which ψ vanishes, we can express $F[\psi]$ as a Taylor expansion in $|\psi|$.

$$F[\psi] \approx F_0 + \alpha|\psi|^2 + \frac{\beta}{2}|\psi|^4 \quad (1.19)$$

We only have even powers because we require $F[\psi]$ to be analytical, and we did not include expansions on the phase of ψ because, in analogy with quantum mechanics, we do not expect the energy to depend on the phase of the wave function. F_0 represents the Free Energy of the normal state above T_c .

¹¹Note the analogy between the first term in Equation 1.18 and the integration constant $\mathbf{C}(\mathbf{r})$ in Equation 1.10.

In order to observe a phase transition, α should become negative below T_c . The simplest functional form that accomplishes that is $\alpha(T) = \alpha'(T - T_c)$, with $\alpha' > 0$ independent of T . β is assumed to be constant and is defined as positive for superconductors.

Below T_c , $F[\psi]$ is minimized by

$$|\psi| = \sqrt{-\frac{\alpha}{\beta}} = \sqrt{\frac{\alpha'}{\beta}} \sqrt{T_c - T} \quad (1.20)$$

which has the typical $\psi \propto \sqrt{T_c - T}$ scaling of mean field theories.

1.4.2 Spatial gradients

To capture edge effects, we must allow for a spatial dependence of the order parameter $\psi \equiv \psi(\mathbf{r})$. The Free Energy functional is then an integral of the energy density over all space (the lowercase symbols correspond to energy densities). We expect an energy cost associated with gradients of the order parameter. We add the simplest term allowed by symmetry

$$F[\psi] \approx \int d^3r \left[f_0 + \alpha|\psi|^2 + \frac{\beta}{2}|\psi|^4 + \frac{1}{2m^*} \left| \frac{\hbar}{i} \nabla \psi \right|^2 \right] \quad (1.21)$$

where the prefactors to the last term are added based on their physical interpretation as kinetic energy with effective mass m^* .

The ground state of the system is found by minimization of $F[\psi]$. By techniques of functional analysis, it is possible to show that this is achieved by an order parameter ψ that solves the following differential equation

$$-\frac{\hbar^2}{2m^*} \nabla^2 \psi + \alpha\psi + \beta|\psi|^2\psi = 0 \quad (1.22)$$

This is equivalent to the Schrödinger equation with an additional non-linear term.¹²

The physical implications of the last equation can be illustrated by solving the 1-dimensional problem for an interface between vacuum and superconductor. As boundary conditions, we impose the order parameter to be identically zero at the interface ($x = 0$) and fully developed as $|\psi| = \sqrt{-\frac{\alpha}{\beta}}$ deep in the superconductor ($x \rightarrow \infty$).

This problem can be solved analytically. Since all the coefficients are real, the solution can be chosen real

$$\psi(x) = \sqrt{-\frac{\alpha}{\beta}} \tanh\left(\frac{x}{\sqrt{2}\xi}\right) \quad (1.23)$$

where

$$\xi := \frac{\hbar}{\sqrt{-2m^*\alpha}} > 0 \quad (1.24)$$

¹²In the framework of the Gross-Pitaevskii theory of bosonic superfluids, this term accounts for an attractive interaction between the particles.

represents the Ginzburg-Landau coherence length. As shown in 1.6, ξ can be interpreted as the typical length over which the amplitude of the superconducting order parameter can change.

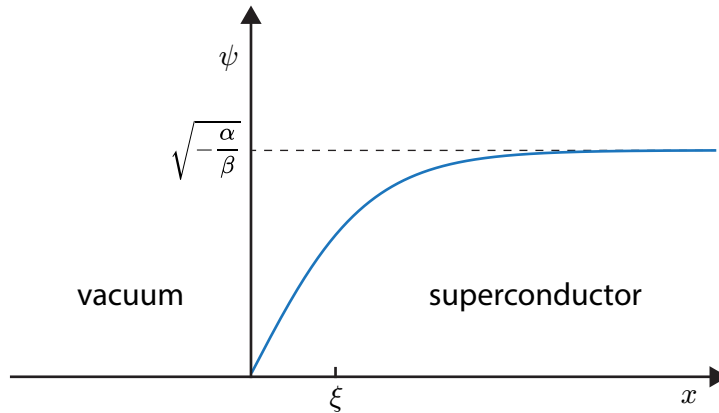


FIGURE 1.6: The Ginzburg-Landau coherence length represents the typical length over which the amplitude of the superconducting order parameter can appreciably change.

1.4.3 Magnetic fields

In order to gain insight into the Meissner effect in the Ginzburg-Landau framework, we need to include the effects of magnetic fields in the Free Energy functional. This can be achieved by applying the usual Peierls substitution to the momentum operator $\frac{\hbar\nabla}{i} \rightarrow \frac{\hbar\nabla}{i} - q\mathbf{A}$ and by adding a term for the energy density of the magnetic field¹³

$$F[\psi, \mathbf{A}] \approx \int d^3r \left[f_0 + \alpha|\psi|^2 + \frac{\beta}{2}|\psi|^4 + \frac{1}{2m^*} \left| \left(\frac{\hbar}{i} \nabla - q\mathbf{A} \right) \psi \right|^2 + \frac{B^2}{2\mu_0} \right] \quad (1.25)$$

Minimization of this Free Energy functional with respect to ψ (see for example [25]) leads to the *First Ginzburg-Landau equation*

$$\frac{1}{2m^*} \left(\frac{\hbar}{i} \nabla - q\mathbf{A} \right)^2 \psi + \alpha\psi + \beta|\psi|^2\psi = 0 \quad (1.26)$$

which is equivalent to a non-linear Schrödinger equation in a magnetic field.

The *Second Ginzburg-Landau equation* can be obtained by minimization with respect of \mathbf{A}

$$\mu_0 \mathbf{j} = \frac{q}{m^*} \Re \left\{ \psi^* \left(\frac{\hbar}{i} \nabla - q\mathbf{A} \right) \psi \right\} \quad (1.27)$$

¹³Different authors use different conventions for the magnetic contribution to the Free Energy. The magnetic energy in the absence of the material $\frac{H_0^2}{2\mu_0}$ is often omitted. We retain it in this analysis.

In the limit of uniform ψ , the last equation reduces to

$$\mathbf{j} = -\frac{q^2|\psi|^2}{m^*}\mathbf{A} \quad (1.28)$$

which is analogous to 1.16. Assuming that the order parameter represents the bound state of two electrons in a BCS fashion, we can set $q = -2e$, the charge of a Cooper pair, and $m^* = 2m_e$, twice the electron mass, which implies $2|\psi|^2 = n_s$.

Ginzburg-Landau's theory is, therefore, a generalization of London's theory, where the superconducting density is allowed to be non-homogeneous in space. In the current formalism, setting $|\psi|^2 = -\alpha/\beta$ in Equation 1.14, the penetration depth can be redefined as

$$\lambda := \sqrt{-\frac{m^*\beta}{\mu_0 q^2 \alpha}} \quad (1.29)$$

So far, two typical lengths have appeared: the coherence length ξ and the penetration length λ . They represent the typical lengths over which the superfluid and the magnetic field, respectively, appreciably change. Both scale as $\approx (T_c - T)^{1/2}$ near T_c and their ratio

$$\kappa := \lambda/\xi \quad (1.30)$$

is therefore temperature independent. It is called the *Ginzburg-Landau parameter* and, as shown in the following subsection, determines the behavior of superconductors in a magnetic field.

In order to compute the response of the superconductor to externally applied magnetic fields, it is convenient to consider the Gibbs Free Energy density G instead of the Helmholtz Free Energy F , since experimentally it is easier to control \mathbf{H} than \mathbf{M} . The two are related by a Legendre transformation

$$G = F - \int dr^3 \mu_0 \mathbf{H} \cdot \mathbf{M} \quad (1.31)$$

For simplicity, we neglect demagnetizing effects and assume the magnetization to be directed along \mathbf{H} , so to consider the magnetic fields as scalars. We neglect surface effects for the moment and consider only the energy inside the superconductor. This assumption is valid for extended systems where the surface energy is negligible compared to the bulk. In this case, $|\psi|^2$ is uniform and equal to $-\alpha/\beta$. Due to the Meissner effect, the magnetic field \mathbf{B} and the vector potential \mathbf{A} (in the London gauge) both vanish, and $M = -H$. In this situation, the energy density of the superconductor is

$$g_s = f_s - HM = \alpha|\psi|^2 + \frac{\beta}{2}|\psi|^4 + \mu_0 H^2 = -\frac{\alpha^2}{2\beta} + \mu_0 H^2 \quad (1.32)$$

In the normal state, the condensation energy of the superconductor vanishes, and the material does not respond to the magnetic field, so that $M = 0$, and we have

$$g_n = \frac{B^2}{2\mu_0} - \mu_0 HM = -\mu_0 \frac{H^2}{2} \quad (1.33)$$

The condition $g_n = g_s$ defines the phase boundary between superconducting and normal states. Thus, above the critical field

$$H_c := \sqrt{\frac{\alpha^2}{\mu_0 \beta}} \quad (1.34)$$

superconductivity is not energetically favorable anymore. This analysis is valid only for the case of a homogenous superconducting order parameter in the bulk of the material.

Accidentally, using Equations 1.29 and 1.34, we can now express the two phenomenological parameters of the Ginzburg-Landau theory in terms of the experimentally measurable quantities H_c and λ

$$\alpha = -\frac{\mu_0^2 q^2 \lambda^2 H_c^2}{m^*} \quad \beta = \frac{\mu_0^3 q^4 \lambda^4 H_c^2}{m^{*2}} \quad (1.35)$$

1.4.4 Type-I and Type-II superconductors

The energy cost of expelling the magnetic field can become significant, especially for unfavorable geometries. Therefore, it is often more convenient for the superconductor to “surrender” a fraction of the condensate to the normal state, allowing the magnetic field to thread that portion of the material, lowering the overall energetic cost of the system.

This trade-off can be quantified by computing the energy of a domain wall between superconductor and normal state. We perform a simplified one-dimensional analysis that can provide a good amount of physical insight. We assume the domain wall to be centered around $x = 0$ and the external magnetic field H to be tuned to have the energy density of the normal state g_n , situated on the negative side of the x-axis, equal to that of the superconductor g_s , situated on the positive side. As in Equation 1.33, deep inside the superconductor, we have

$$g(x \rightarrow \infty) = g(x \rightarrow -\infty) = f_n + \mu_0 \frac{H_c^2}{2} \quad (1.36)$$

The additional Free Energy per unit area γ due to the domain wall is

$$\gamma = \int_{-\infty}^{\infty} dx [g(x) - g(x \rightarrow \infty)] \quad (1.37)$$

By using Equations 1.26 and 1.36, after some algebra, we get

$$\gamma = \mu_0 \frac{H_c^2}{2} \int_{-\infty}^{\infty} dx \left[\left(1 - \frac{B}{\mu_0 H_c}\right) - \frac{|\psi|^4}{|\psi_\infty|^4} \right] \quad (1.38)$$

As anticipated, the energy density per unit area to form a domain wall is a balance between two contributions: the *energy cost* required to exclude the magnetic field (first term of the integrand) and the *energy gain* to form the condensate (second term of the integrand).

Deep inside the superconductor $B \rightarrow 0$ and $|\psi| \rightarrow |\psi|_\infty$, so the integrand vanishes. The same happens deep inside the normal region, where $B \rightarrow \mu_0 H_c$ and $|\psi| \rightarrow 0$. Therefore, as expected, the only contribution to the surface energy comes from regions around the domain wall. Based on the considerations discussed in Subsection 1.4.3, we can rewrite this expression as a function of the penetration depth λ and the coherence length ξ

$$\gamma \approx -\mu_0 \frac{H_c^2}{2} (\lambda - \xi) \quad (1.39)$$

Type-I superconductors are defined by having a positive energy cost γ associated with the formation of a domain wall. From Equation 1.39 it is clear that this is the case for $\xi \gg \lambda$ ($\kappa \ll 1$). In this limit, the superconductor prefers to maintain a homogenous phase until the external field reaches the critical value H_c . At this point, superconductivity is not energetically favorable anymore, and there is a phase transition to the normal state¹⁴.

Type-II superconductors, on the other hand, are defined by having a negative γ , which happens for $\xi \ll \lambda$ ($\kappa \gg 1$). In this case, there is an instability towards the formation of domain walls¹⁵. This process has to be counterbalanced by some other effect. Otherwise, ψ would vary wildly over short-length scales, ultimately invalidating the order parameter description. This regulatory effect is the fluxoid quantization introduced in the following subsection.

1.4.5 Fluxoid quantization

Flux quantization is a direct consequence of the coherence properties of the wave function used to describe a macroscopic system. These can be made more apparent by expressing ψ as a product of an amplitude and a phase

$$\psi := |\psi| e^{i\theta} \quad (1.40)$$

In these variables, the current density 1.27 reads

$$\mu_0 \mathbf{j} = \frac{q\hbar}{m^*} |\psi|^2 \nabla \theta - \frac{q^2}{m^*} |\psi|^2 \mathbf{A} \quad (1.41)$$

Normalizing 1.41 by $\frac{q^2}{m^*} |\psi|^2$ and taking the line integral around a closed loop yields

$$\frac{m^*}{q^2} \oint d\mathbf{l} \cdot \frac{\mu_0 \mathbf{j}}{|\psi|^2} + \oint d\mathbf{l} \cdot \mathbf{A} = \frac{\hbar}{q} \oint d\mathbf{l} \cdot \nabla \theta \quad (1.42)$$

¹⁴A more detailed analysis [24] shows that, for external fields close to H_c and depending on the sample shape, type-I superconductors possess an intermediate phase. This phase is called *mixed state* because superconducting and normal regions coexist close to one another, and the cost of forming domain walls is compensated by lowering the magnetic energy outside the sample.

¹⁵This analysis has been carried out in the simplified assumption of g_n equal to g_s deep inside the respective regions. Therefore, this instability *does not* happen for arbitrarily low values of the external field, as expected.

Since the order parameter must be single-valued, the integral on the right can only take values multiple of 2π . Additionally, the integral on the right vanishes for simply connected paths since ψ is analytical.

It does not necessarily vanish for topologically non-trivial paths as the one shown in Figure 1.7. The hole in the center can be engineered or represent a physical vacancy. Alternatively, the system can decide to suppress the superfluid density in that region to allow the magnetic field to penetrate through that area, as discussed in Subsection 1.4.4 in connection with type-II superconductors.

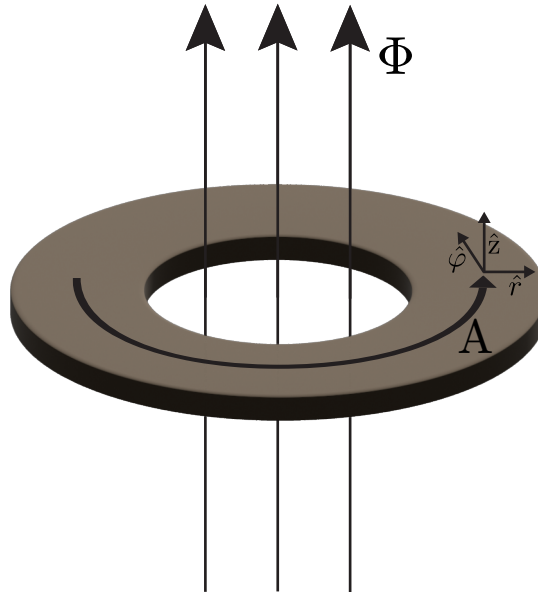


FIGURE 1.7: A magnetic flux Φ through a superconducting ring generates a vector potential \mathbf{A} even inside the superconductor, where there cannot be a magnetic field \mathbf{B} .

Using Stokes' theorem, we recognize the second integral on the left as the magnetic flux Φ through the area we considered. Equation 1.42 then becomes

$$\frac{m^*}{q^2} \oint d\mathbf{l} \cdot \frac{\mu_0 \mathbf{j}}{|\psi|^2} + \Phi = n\Phi_0 \quad (1.43)$$

where n is an integer, and we defined the *quantum of flux* as

$$\Phi_0 = \frac{h}{q} \quad (1.44)$$

The left-hand term in Equation 1.43 is named *fluxoid* and is the quantity that is quantized. It differs from the magnetic flux Φ by $\frac{m^*}{q^2} \oint d\mathbf{l} \cdot \frac{\mu_0 \mathbf{j}}{|\psi|^2}$. In type-I superconductors, this integral can be taken over a region where the magnetic field has been fully screened, and the current has vanished. In that case, the magnetic flux Φ is also quantized.

This quantization has been experimentally demonstrated [26], where it was observed that the charge q appearing in the expression for the flux quantum 1.44 was

close to twice the charge of the electron. This observation provided further evidence for the mechanism of two-electron pairing that leads to superconductivity in the BCS framework.

As mentioned in the previous section, type-II superconductors spontaneously form an inhomogeneous distribution of the order parameter that allows the magnetic field to thread through the superconductor. Fluxoid quantization limits this effect and leads to the creation of vortices, each of which carries a quantum Φ_0 of magnetic field flux.

This vortex phase forms for a sufficiently large external magnetic field $H_{c1} < H_c$, referred to as *first critical field*. Given their quantum nature, vortices can be considered topological defects of the superconducting phase, of size proportional to the coherence length of the superconductor ξ . For even higher fields $H_{c2} > H_c$, the density of vortices becomes so high that there is no more energetic gain from having a superconducting condensate, and there is a transition to the normal state. In type-II superconductors, no significant change happens at H_c .

1.4.6 Anisotropic formulation

The standard formulation of the Ginzburg-Landau theory assumes an isotropic material. This assumption is valid for most elemental superconductors but not for layered superconductors such as high- T_c cuprates. In order to capture their intrinsically anisotropic nature, the scalar mass term in Free Energy functional 1.21 has to be replaced by a tensor so that

$$F[\psi] \approx \int d^3r \left[F_0 + \alpha|\psi|^2 + \frac{\beta}{2}|\psi|^4 + \sum_i \frac{1}{2m_i^*} \left| \frac{\hbar}{i} \nabla_i \psi \right|^2 \right] \quad (1.45)$$

where $1/m_i^*$ represents the principal values of the tensor of the inverse effective mass. In layered superconductor, this results in an *in-plane mass* $m_{//}$ and an *out-of-plane mass* m_{\perp} , where $m_{\perp} < m_{//}$. This distinction leads to redefining accordingly the penetration depth λ and the coherence length ξ in Equations 1.29 and 1.24. For example, in cuprates, the penetration depth of a magnetic field applied along the planes λ_{\perp} is greater than that of a field applied perpendicular to them $\lambda_{//}$. The effect of anisotropy on other thermodynamic quantities is discussed in [27], Chapter 9.

1.4.7 Time-dependent formulation and vortex motion

Ginzburg-Landau's theory is normally applied to equilibrium systems. It can, however, be extended to study dynamics. In this case the order parameter becomes time-dependent $\psi \equiv \psi(\mathbf{r}, t)$ and the Lagrangian of the system reads

$$L = \int d^3r i\hbar \psi^* \frac{\partial \psi}{\partial t} - F[\psi] \quad (1.46)$$

where $F[\psi]$ is the Ginzburg-Landau functional.

From the *least action principle*, we obtain the equation of motion by minimizing the action $S = \int_{t_i}^{t_f} dt L$, which leads to

$$i\hbar \frac{\partial \psi}{\partial t} = \frac{1}{2m^*} \left(\frac{\hbar}{i} \nabla - q\mathbf{A} \right)^2 \psi + \alpha \psi + \beta |\psi|^2 \psi + \frac{B^2}{2\mu_0} \quad (1.47)$$

This is a non-linear version of the time-dependent Schrödinger equation.¹⁶ In practice, it is typically solved numerically and by adding phenomenological parameters related to model non-idealities, such as flux pinning by defects.

The initial conditions depend on the problem at hand. The onset of superconductivity can be modeled by imposing a time dependence on the sign of α to make superconductivity favorable at a given instant in time. It is possible, then, to study the magnetic dynamics that follows. In the case of type-II superconductors such as $\text{YBa}_2\text{Cu}_3\text{O}_{7-\delta}$, the dominant physical aspect is vortex motion [28].

1.5 Fluctuations above critical temperature

In Section 1.4, we have considered only the state ψ_0 that minimizes the Ginzburg-Landau functional given by Equation 1.25. In the many-body formalism, this is equivalent to the *mean-field* state, where the interaction between particles is incorporated as an average field acting on independent particles.

In this section, we first overview corrections to the mean-field state and then highlight how, in low-dimensional systems, fluctuations alone can lead to the instability of the superconducting state.

1.5.1 Gaussian fluctuations

At finite temperatures, the system fluctuates around its minimum Free Energy. Assuming a bulk system with uniform ψ_0 , the order parameter of the system is then

$$\psi(\mathbf{r}) = \psi_0 + \delta\psi(\mathbf{r}) \quad (1.48)$$

In order to extract the thermodynamic properties of the system, we need its Hamiltonian. As discussed in more detail in [29], the use of the Free Energy functional $F[\psi]$ for such a role is justified by recognizing ψ as the macroscopic wave function of the system. The partition function \mathcal{Z} then reads

$$\mathcal{Z} = \int D^2\psi e^{-F[\psi]/k_B T} \quad (1.49)$$

where $\int D^2\psi$ represents integration over the infinitely many possible realizations of $\psi(\mathbf{r})$.

The integral 1.49 is, generally, hard to compute. Since we are interested in the situation $T > T_c$, we can simplify the expression by noting that ψ_0 vanishes in this

¹⁶This equation is known as the time-dependent Gross-Pitaevskii equation in the context of superfluid condensates.

regime and by neglecting in $F[\psi]$ the terms higher than second order in $|\psi|$. This assumption is justified since, at high temperatures, the term proportional to β is not needed to stabilize the theory. This approach is called *Gaussian approximation*¹⁷.

Within this limit, the Free Energy in a zero magnetic field reads

$$F[\psi] \approx \int dr^3 \left[\alpha \psi^*(\mathbf{r})\psi(\mathbf{r}) + \frac{1}{2m^*} \left(\frac{\hbar}{i} \nabla \psi(\mathbf{r}) \right)^* \cdot \frac{\hbar}{i} \nabla \psi(\mathbf{r}) \right] \quad (1.50)$$

In the Fourier basis, where

$$\psi(\mathbf{r}) = \frac{1}{\sqrt{V}} \sum_{\mathbf{k}} e^{i\mathbf{k}\cdot\mathbf{r}} \psi_{\mathbf{k}} \quad (1.51)$$

the Free Energy becomes

$$\begin{aligned} F[\psi] &\approx \frac{1}{V} \sum_{\mathbf{k}'\mathbf{k}} \int dr^3 e^{-i(\mathbf{k}-\mathbf{k}')\cdot\mathbf{r}} \left[\alpha \psi_{\mathbf{k}'}^* \psi_{\mathbf{k}} + \frac{1}{2m^*} (\hbar \mathbf{k} \psi_{\mathbf{k}})^* \cdot \hbar \mathbf{k} \psi_{\mathbf{k}} \right] \\ &= \sum_{\mathbf{k}} \left(\alpha + \frac{\hbar^2 k^2}{2m^*} \right) \psi_{\mathbf{k}}^* \psi_{\mathbf{k}} \end{aligned} \quad (1.52)$$

By recognizing the term within parenthesis as the energy of the fluctuations

$$\epsilon_{\mathbf{k}} = \alpha + \frac{\hbar^2 k^2}{2m^*} \quad (1.53)$$

we see that, for every \mathbf{k} , there are two degenerate fluctuation modes corresponding, for example, to the amplitude and phase degrees of freedom of ψ . Additionally, since α is positive and temperature dependent, the dispersion has a finite energy gap, which is also temperature dependent.

By inserting the Free Energy 1.52 into the definition of partition function 1.49, we get

$$\begin{aligned} \mathcal{Z} &\approx \int \left(\prod_{\mathbf{k}} d^2 \psi_{\mathbf{k}} \right) \exp \left(-\frac{1}{k_B T} \sum_{\mathbf{k}} \epsilon_{\mathbf{k}} \psi_{\mathbf{k}}^* \psi_{\mathbf{k}} \right) \\ &= \prod_{\mathbf{k}} \left[\int_{\mathbb{C}} d^2 \psi_{\mathbf{k}} \exp \left(-\frac{1}{k_B T} \epsilon_{\mathbf{k}} \psi_{\mathbf{k}}^* \psi_{\mathbf{k}} \right) \right] \\ &= \prod_{\mathbf{k}} \pi \frac{k_B T}{\epsilon_{\mathbf{k}}} \end{aligned} \quad (1.54)$$

where, in the last step, we used the analytical solution for a Gaussian integral.

With the partition function at hand, all thermodynamic properties follow. For example the heat capacity reads

$$C = T \frac{\partial^2}{\partial T^2} k_B T \ln \mathcal{Z} \quad (1.55)$$

¹⁷The name is due to the appearance of a Gaussian integral in the later derivation.

By inserting the expression 1.54, and keeping only the term which is singular at T_c and gives the strongest contribution, after some algebra, we find

$$C \approx \text{constant} \cdot \frac{1}{\sqrt{\alpha}} \propto (T - T_c)^{-1/2} \quad (1.56)$$

Similar temperature dependencies can be extracted for other thermodynamic quantities.

This derivation shows that, due to thermal agitation, the system “feels” the presence of a phase transition even above its critical temperature. In superconductors, however, the fast decaying $-1/2$ exponent limits the observability range of these Gaussian fluctuations to a few Kelvin above T_c .

1.5.2 BKT instability

In low dimensional systems ($d \leq 2$), the Mermin-Wagner theorem prevents the onset of long-range order. This applies specifically to 2-dimensional superconductors. In this case, the system can at best establish a *quasi-long-range order*, where its correlation function decays with some critical exponent η as

$$\langle \psi(\mathbf{r})^* \psi(\mathbf{0}) \rangle \approx \psi_0^2 \left(\frac{r}{r_0} \right)^{-\eta} \quad (1.57)$$

The reason is that the system is unstable towards the proliferation of fluctuations, which tends to lower its Free Energy by maximizing the entropy. These effects are particularly severe in systems with a low density of superconducting carriers, which implies very high fluctuations in their number. Below a critical concentration of carriers, the system is, therefore, subject to a phase transition where the superconducting state is destroyed by fluctuations despite being favorable in a mean-field sense.

These concepts have been formalized for a 2-dimensional neutral superfluid by Berezinskii, Kosterlitz and Thouless [30]. In their theory, based on the Ginzburg-Landau formalism, the critical exponent in Equation 1.57 is given by

$$\eta = \frac{1}{2\pi} \frac{k_B T \beta m^*}{\hbar^2 \alpha} > 0 \quad (1.58)$$

Close to the *mean-field critical temperature* T_{MF} , $\alpha \rightarrow 0$ and the correlation length diverges. The system, therefore, cannot attain the superconducting order. Superconductivity is restored only below a certain *fluctuation critical temperature* T_{fl} , where the formation of vortices becomes energetically unfavorable. The threshold for the formation of non-interacting vortices can be shown to correspond to the temperature at which $\eta = 1/4$. Interactions between vortices lead to screening effects, further lowering T_{fl} . Finally, no fluctuations can be thermally excited at zero temperature, and $\eta = 0$ (see Figure 1.8).

Strictly speaking, the BKT formalism applies only to 2-dimensional systems. However, they are often qualitatively applied also to quasi-2-dimensional systems, such as

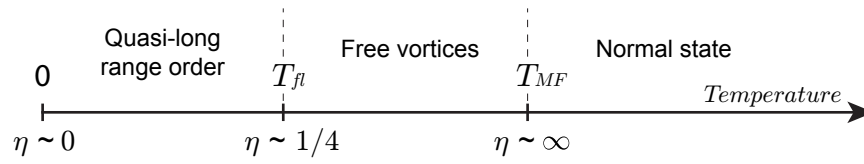


FIGURE 1.8: Due to the generation of free vortices, the quasi-long-range order in a 2-dimensional condensate is not attained at T_{MF} but rather at a lower temperature denoted T_{fl} .

cuprates. Indeed, as discussed in Subsection 1.4.6, these systems can be thought of as weakly coupled 2-dimensional layers. A related discussion can be found in [31]. The role of fluctuations in determining the superconducting properties in layered cuprates is still under debate.

Chapter 2

The unconventional Superconductor $\text{YBa}_2\text{Cu}_3\text{O}_{7-\delta}$

Historically, $\text{YBa}_2\text{Cu}_3\text{O}_{7-\delta}$ was the first discovered high-temperature superconductor with a $T_c \sim 90\text{K}$ higher than the boiling point of nitrogen. Variation of the oxygen doping strongly influences its electronic properties and, less drastically, its crystal structure. More recently, the atypical properties of the pseudogap phase found in the underdoped region sparked new interest in this compound, particularly for their correlation with light-induced superconductivity.

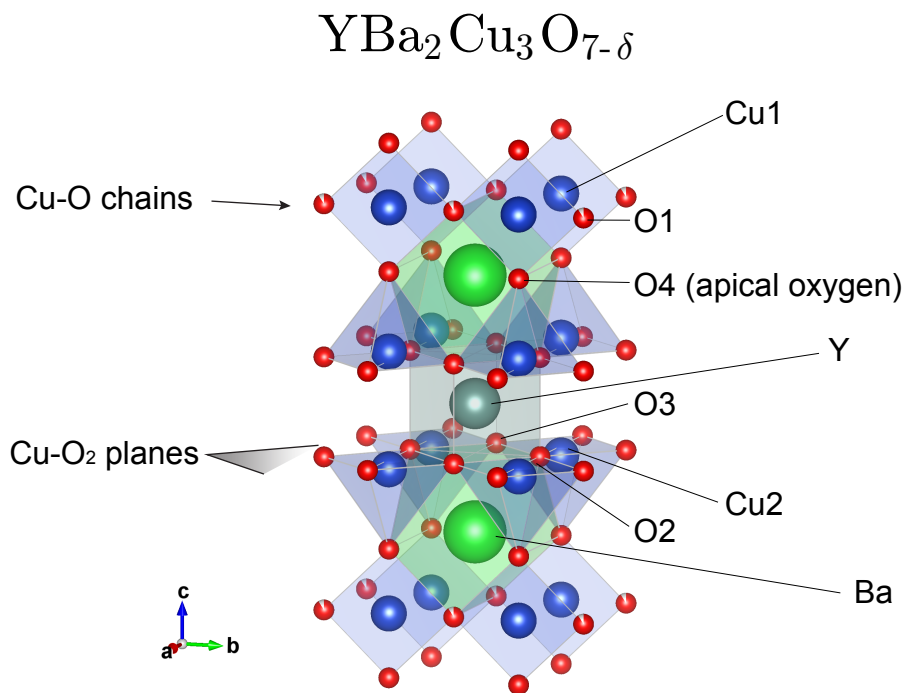


FIGURE 2.1: Crystal structure of $\text{YBa}_2\text{Cu}_3\text{O}_{7-\delta}$. The partial filling of O1 indicates non-stoichiometric occupancy of the oxygens, where $\delta = 0$ (orthorhombic phase) corresponds to full occupancy and $\delta = 1$ (tetragonal phase) to complete vacancy. In the intermediate case, the oxygens are organized in chains. “VESTA 3 for three-dimensional visualization of crystal, volumetric and morphology data”.

2.1 Crystal Structure and lattice modes

$\text{YBa}_2\text{Cu}_3\text{O}_{7-\delta}$ crystals are arranged in a perovskite structure, shown in Figure 2.1. Depending on the oxygen doping δ and the temperature of synthesis, the crystal symmetry is either the orthorhombic $Pmmm(D_{2h}^1)$ or the tetragonal $P4/mmm(D_{4h}^7)$. In the orthorhombic phase, typical dimensions of the unit cell are $a = 3.83 \text{ \AA}$, $b = 3.89 \text{ \AA}$, $c = 11.65 \text{ \AA}$.

Contrary to most cuprates consisting of single layers, $\text{YBa}_2\text{Cu}_3\text{O}_{7-\delta}$ organizes in a bilayer structure composed of alternating Cu-O_2 planes normal to the c -direction and Cu-O chains along the b -direction. The latter are responsible for the orthorhombic distortion of the structure, where the O_2 and O_3 oxygens are slightly shifted along c . The Cu-O_2 planes are highly conducting, and the chains act as charge reservoirs. On the other hand, hopping across the planes is much less likely, and conductivity in the c -direction is one order of magnitude lower. A satisfactory model describing the system needs to include this anisotropic character (for example, see Subsection 1.4.6).

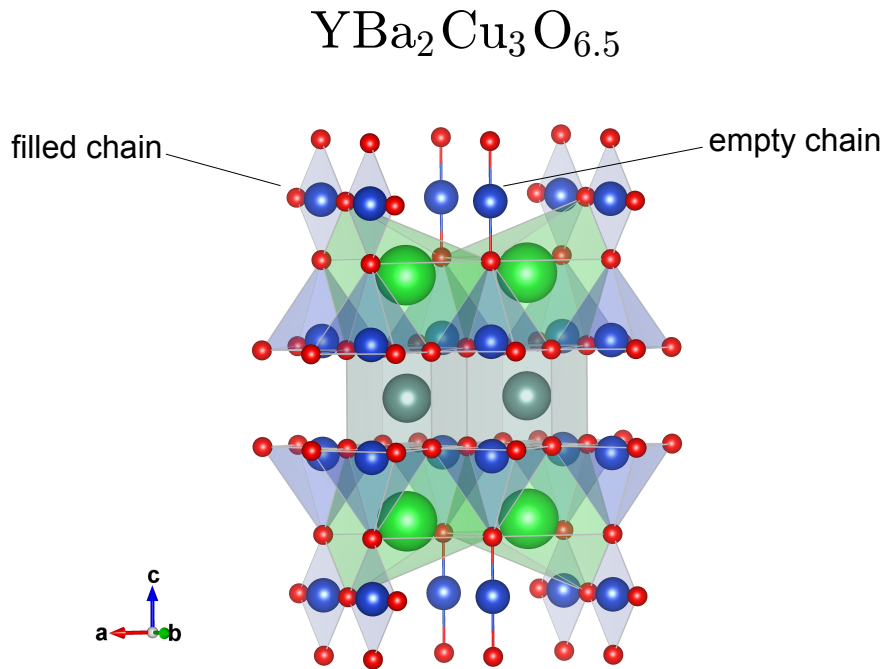


FIGURE 2.2: Crystal structure of $\text{YBa}_2\text{Cu}_3\text{O}_{6.5}$. For this range of doping, the Cu-O chains are alternatively filled and vacant. The unit cell is doubled along the a -axis compared to $\text{YBa}_2\text{Cu}_3\text{O}_7$. “VESTA 3 for three-dimensional visualization of crystal, volumetric and morphology data”.

By heating the sample above 500° , the weakly coupled O_1 oxygens in the chains diffuse away, increasing the oxygen vacancies δ . It is then possible to continuously tune the doping from $\text{YBa}_2\text{Cu}_3\text{O}_7$ ($\delta = 0$), where the chains are fully occupied, to $\text{YBa}_2\text{Cu}_3\text{O}_6$ ($\delta = 1$), where they are completely vacant. For $0 < \delta < \sim 0.6$, some chains are missing while others remain unaffected, meaning all the vacancies tend to

self-organize along the same chain over macroscopic distances. The chemical formula is non-stoichiometric, and the structure in Figure 2.1 no longer represents the unit cell of the system. This inhomogeneity leads to intermediate properties between $\text{YBa}_2\text{Cu}_3\text{O}_7$ and $\text{YBa}_2\text{Cu}_3\text{O}_6$. In particular, in $\text{YBa}_2\text{Cu}_3\text{O}_{6.5}$, the chains are alternatively filled and empty, and the unit cell is doubled along the a-direction (see Figure 2.2). This phase is denoted orthorhombic-II to distinguish it from the one manifested by $\text{YBa}_2\text{Cu}_3\text{O}_7$, denoted as orthorhombic-I. Above $\delta \sim 0.6$, there is a structural phase transition to the tetragonal phase where the a and b axes become equivalent. The orthorhombic phase can be retained up to $\delta \sim 0.8$ by removing the oxygen with the low-temperature Zr-gettered annealing technique [32].

The position of the O4 apical oxygen atom varies significantly with oxygen doping, and, as a consequence, the intralayer distance is modified. For example, in $\text{YBa}_2\text{Cu}_3\text{O}_{6.5}$, the unit cell is elongated along the c-direction by 3% with respect to $\text{YBa}_2\text{Cu}_3\text{O}_7$. Band structure studies covering almost all hole-doped cuprates have suggested a correlation between their intralayer distance and the T_c manifested in the superconducting state [33]. In the community of ultrafast science, this prompted the question of whether one could influence the superconducting properties of $\text{YBa}_2\text{Cu}_3\text{O}_{7-\delta}$ by selectively altering its atomic structure with light.

2.1.1 Infrared active modes in $\text{YBa}_2\text{Cu}_3\text{O}_{6.5}$

From the orthorhombic-II structure of $\text{YBa}_2\text{Cu}_3\text{O}_{6.5}$, 72 different phonon modes are present, 33 Raman-active and 39 IR-active. Here, we focus on the 7 IR-active modes polarized along the c-direction. These can be observed in Fourier Transform Infrared (FTIR) spectroscopy experiments. As an indicator of the presence of these modes, the top panel of Figure 2.3 shows the real part of the optical conductivity σ_1 as a function of photon wavenumber. The peaks of the four predominant frequencies are marked with dashed lines, and the corresponding atomic motions are shown below.

The modes at 16.4 THz and 19.2 THz correspond to the apical oxygen motions of the oxygen-filled and oxygen-vacant chains. The former is the only one present in $\text{YBa}_2\text{Cu}_3\text{O}_7$ and the latter in $\text{YBa}_2\text{Cu}_3\text{O}_6$, and therefore are often referred to with the respective compound names. The intermediate systems present both in a ratio proportional to their doping δ .

2.1.2 Transient displacement of the lattice via nonlinear phononics

The classical approach to modifying the lattice spacing relies on applying pressure along a preferential direction. This can be performed either mechanically (e.g., with a diamond anvil cell), epitaxially, or by chemical substitution. However, the maximum lattice distortion achievable is ordinarily limited to about 1% of the lattice spacing. On the other hand, resonant driving of phonons modes with intense pulses can lead to much higher displacements. As an upper limit, Lindemann's criterion estimates a maximum atomic mean-squared displacement of about 10%.

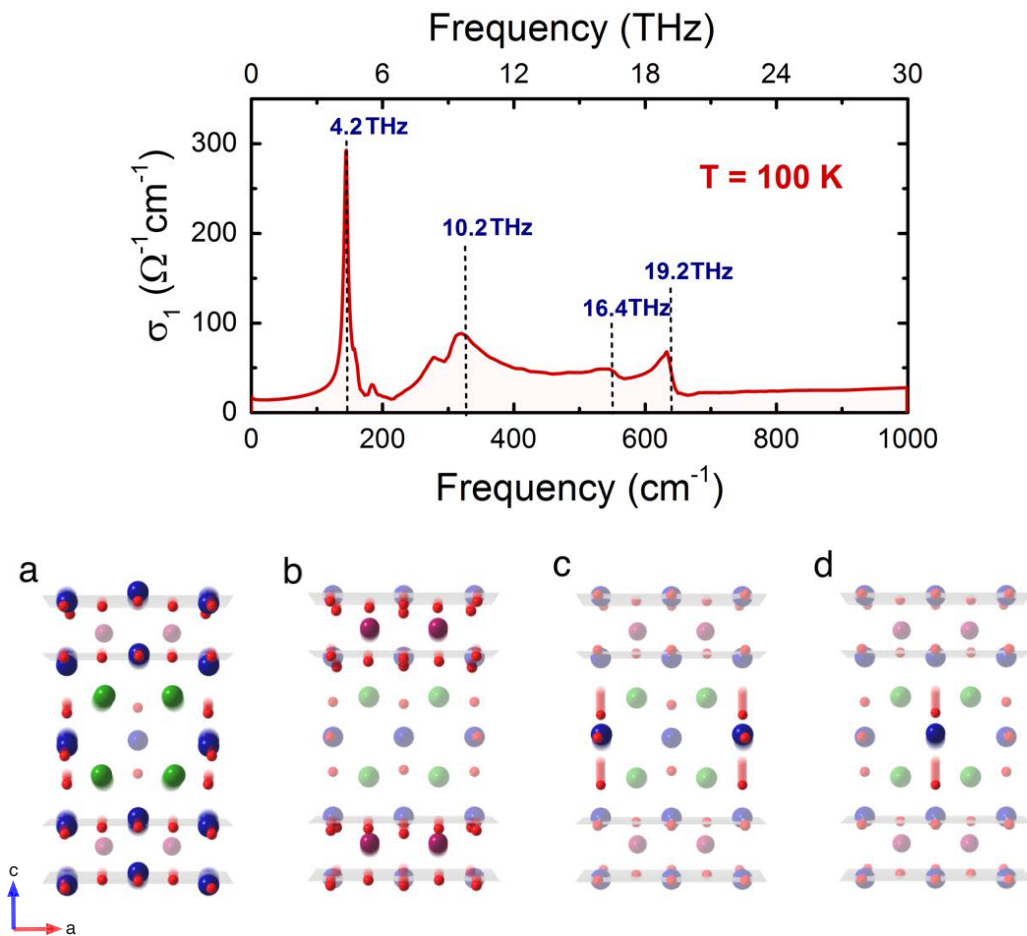


FIGURE 2.3: The top panel shows the infrared active modes of $\text{YBa}_2\text{Cu}_3\text{O}_{6.5}$ measured from FTIR spectroscopy. The bottom diagrams represent the four predominant modes (a) 140 cm^{-1} , (b) 337 cm^{-1} , (c) 547 cm^{-1} and (d) 640 cm^{-1} . The quasi-static atoms have been grayed out. Adapted from [16].

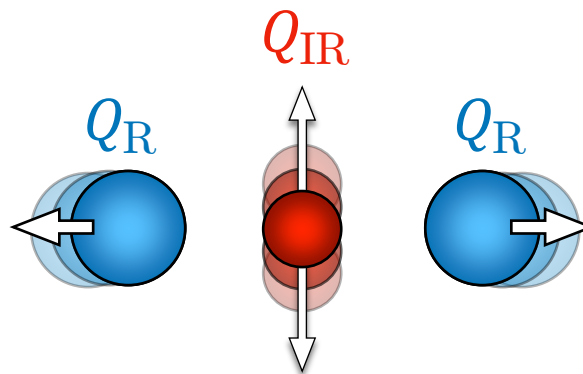


FIGURE 2.4: Comparison between infrared (red) and Raman (blue) modes in a centrosymmetric crystal.

In a centrosymmetric solid, the phonon modes can be classified based on whether the atomic displacement is symmetry-odd or symmetry-even with respect to their inversion center (see Figure 2.4). Symmetry-odd modes, also known as *IR-active*, are the only ones that can be driven with an electric field¹. Symmetry-even modes, also known as *Raman-active*, are not set in motion by the driving field.

This is no longer true when the intensity of the electric field is strong enough to access the nonlinear regime. In this case, the IR-active mode will transfer part of its energy to other modes. The simplest potential allowed by symmetry that can describe this process is

$$\begin{aligned}
 V = & \frac{1}{2} \sum_i \omega_{IR,i}^2 Q_{IR,i}^2 + \frac{1}{2} \sum_i \omega_{R,i}^2 Q_{R,i}^2 + E(t) \cdot \sum_i Z_i^* Q_{IR,i} \\
 & + \sum_{i,j,k} f_{i,j,k} Q_{R,i} Q_{R,j} Q_{R,k} + \sum_{i,j,k} g_{i,j,k} Q_{IR,i} Q_{IR,j} Q_{R,k} \\
 & + \sum_{i,j,k,l} h_{i,j,k,l} Q_i Q_j Q_k Q_l + \dots
 \end{aligned} \tag{2.1}$$

where ω , Q , and Z^* represent the eigenfrequency, coordinate, and effective charge of the mode [35]. The IR and R suffixes differentiate between infrared and Raman modes, and the summation indices run over the respective modes. The first line describes the linear regime, where the first two terms account for the harmonic energy of the modes and the third one for the energy transferred from the electric field.

The second line introduces third-order nonlinearities. The first term accounts for self-anharmonicities, where the Raman modes are the only symmetry-allowed. The second term accounts for the coupling between different modes. Finally, the third line represents the fourth and higher orders. The material-dependent parameters f , g , and h indicate the strength of the nonlinearity.

In Figure 2.5, an example of a nonlinear regime is presented. The first plot represents the time-dependent driving field $E(t)$. The second plot shows a resonantly driven IR-active mode. As can be observed from the plot, its average displacement over the whole transient $\langle Q_{IR} \rangle = 0$. On the contrary, the non-linearly driven Raman mode presented in the third plot has an effective driving force proportional to the square of the IR-active mode. Consequently, its average displacement $\langle Q_R \rangle \neq 0$. Due to the nonlinear coupling, the crystal lattice is transiently deformed over time scales comparable with the decay time of the Raman mode. In systems with very few electronic carriers, the decay time is set by the strength of the phonon-phonon coupling itself.

By employing first-principles density function theory (DFT) calculation, the geometries of the modes in $\text{YBa}_2\text{Cu}_3\text{O}_{6.5}$ and their respective couplings were computed [36]. The observed dynamics, tracked with femtosecond X-ray diffraction, matched the theoretical predictions well. In particular, it was confirmed that driving

¹Strictly speaking, this requirement is not sufficient. In addition, the displacement needs to induce a non-zero electrical dipole. These modes are called ‘‘polar’’. For the distinction, see, for example, [34], Subsection 1.5.14.

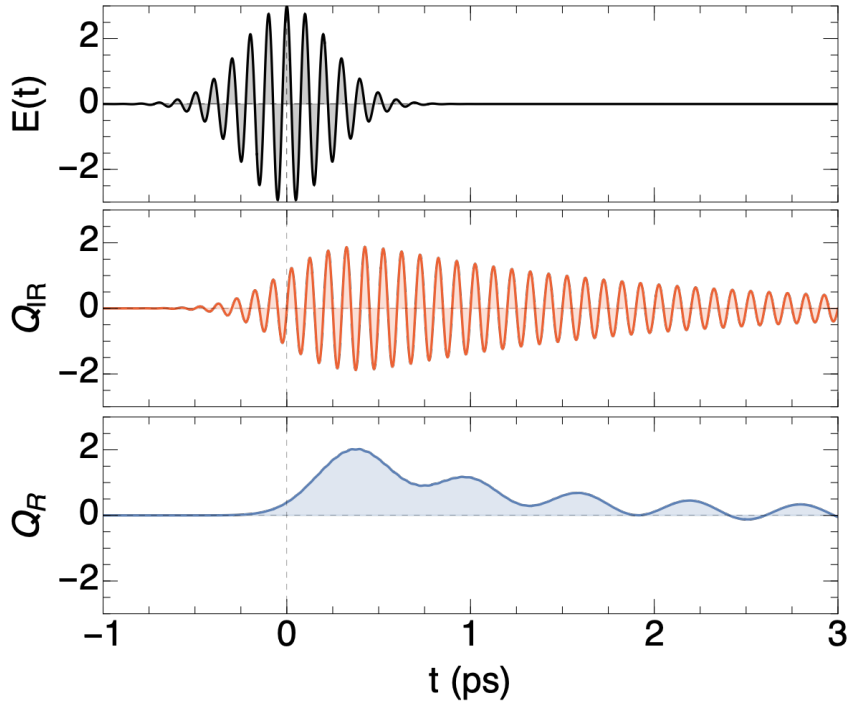


FIGURE 2.5: Comparison between infrared (red) and Raman (blue) modes in a centrosymmetric crystal. Kindly provided by M. Fechner.

the apical-oxygen modes of the material influences both the inter- and intra-bilayer spacing, strongly correlated with the onset of superconductivity in cuprate systems.

2.2 Phase diagram and electronic properties

The study of the phase diagram of $\text{YBa}_2\text{Cu}_3\text{O}_{7-\delta}$ and other cuprates has been central to condensed matter research for the past half-century. The coexistence of different and often competing orders, with behavior contradicting well-established physical paradigms, made it a theoretical challenge pushing forward the development of modern many-body theories.

Figure 2.6 presents the experimentally determined phase diagram of $\text{YBa}_2\text{Cu}_3\text{O}_{7-\delta}$. For $\delta = 1$, the system presents an antiferromagnetic order with a Néel temperature of $T_N \sim 420$ K. From a band theory perspective, the Cu_2O planes contain an odd number of electrons per unit cell and, consequently, should be conductive. This prediction contradicts the experiments, where an insulating gap of $\sim 1 - 2$ eV is observed and highlights the importance of electron correlations in describing the system. Indeed, it is found that the typical Coulomb repulsion energy $U \sim 9$ eV is significantly larger than the bandwidth of the conduction band $W \sim 3$ eV, thus leading to the opening of a Mott bandgap determined by spin fluctuations. The much lower gap found in experiments suggests an additional mechanism. The energy of the charge transfer $\Delta \sim 3$ eV is indeed found to sit at an intermediate value, $W < \Delta < U$, and acts as the lowest energy excitation of the electronic system. For this reason, $\text{YBa}_2\text{Cu}_3\text{O}_6$ is

said to be a *charge-transfer insulator* (see [37], Chapter 5 for a more detailed discussion on the electronic properties and band structure of cuprates).

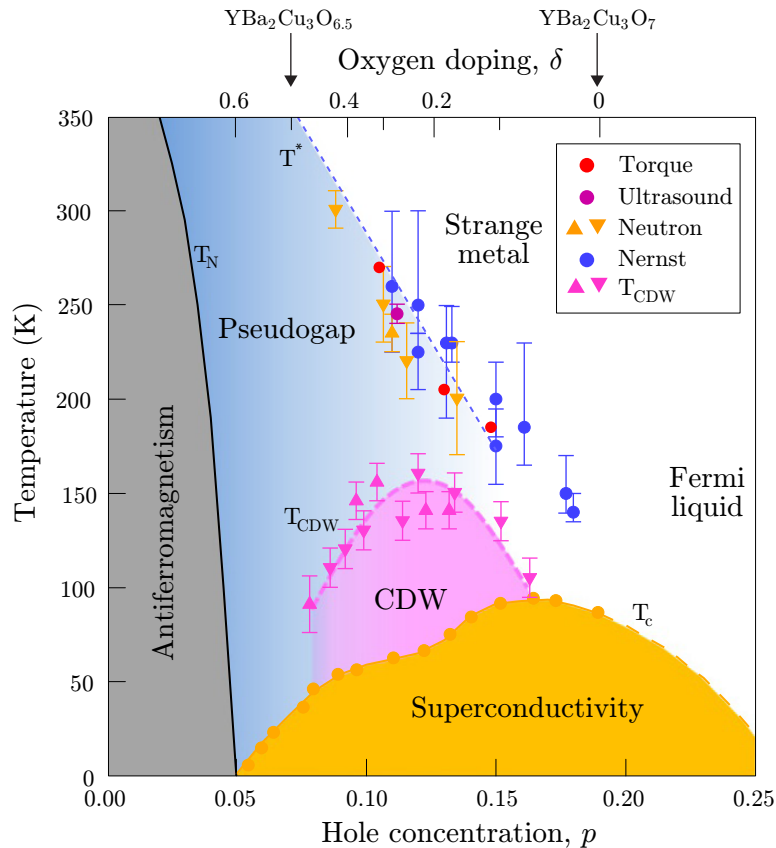


FIGURE 2.6: Phase diagram of $\text{YBa}_2\text{Cu}_3\text{O}_{7-\delta}$ as a function of hole concentration showing at least four different orders. The dashed line indicates the transition from the strange metal to the pseudogap phase, as determined by in-plane torque magnetometry [38], Nernst coefficients [39], ultrasound spectroscopy [40] and polarized neutron scattering [41]. T_{CDW} represent the phase boundary of the charge density wave phase, as measured by x-ray resonant measurements [42, 43]. Adapted from [38].

Similarly to ionic semiconductors, metallic conductivity appears with a change of stoichiometry, which in this case amounts to oxygen doping. As outlined in Section 2.1, the additional oxygens sit in the Cu-O chains and act as charge reservoirs for the $\text{Cu}_2\text{-O}$ planes. The hole doping p is proportional to the oxygen concentration in the chains. At a critical value of $p \sim 0.05$ at zero temperature, the antiferromagnetic order is disrupted. This critical value appears at a progressively lower hole doping p as the temperature increases.

For $p > 0.05$, a superconducting phase emerges, with a monotonically increasing T_c up to an optimal value $p_{opt} \sim 0.18$. The two plateaus observed in the phase diagram are associated with the two orthorhombic phases, I and II (see Section 2.1). Above this optimal value and up to $p \sim 0.25$, T_c progressively lowers, closing the so-called

superconducting dome. Phases realized for hole doping below and above the optimal value p_{opt} are said to belong to the *underdoped* and *overdoped* regime, respectively.

In the underdoped regime, for temperature ranging from 100 K to 200 K, it has been recently observed the appearance of static charge-stripe order [44], a feature previously believed as exclusive to the $La_2Sr_{2-x}CuO_4$ family. Subsequent experiments confirmed that the short-ranged charge order is incommensurate and predominantly localized at defects pinning the correlated charge fluctuations [45]. Interestingly, these features gradually set in at the charge ordering temperature T_{CDW} , reach a maximum at the superconducting critical temperature T_c , and drastically drop below, indicating strong competition between these two orders.

For even higher temperatures, the underdoped region of the phase diagram presents the pseudogap phase. This name originates from angle-resolved photoemission spectroscopy (ARPES) measurements that showed a partial suppression of the electronic density of states in the “antinodal” region of the Brillouin zone [46]. Many other features reminiscent of superconductivity, such as an anomalous Nernst effect [39] or anomalous diamagnetism [47, 48], have been observed in this regime, remarkably extending up to room temperature. These observations suggest that pairs already form at these high temperatures, at least locally, but phase fluctuations prevent the superconducting order from setting in until much lower temperatures.

All these features emerge from the least understood of the phases presented so far, which, due to its atypical properties, has been termed *Strange Metal*. The most striking feature is the absence of quasiparticles, which lie at the center of the description of standard metals. This absence leads to significant deviations in the temperature dependence of the electrical [49] and Hall conductivity [50]. Many new theories were developed trying to capture these phenomena, spanning from the description as a *marginal Fermi liquid* [51], in connection with quantum criticality and even as parallelisms with string theory [52]. Owing to the arduous mathematical formalism required, a comprehensive theory capable of capturing the strong interactions in the strange metal phase is still lacking to this day.

This little understanding of the electronic properties in the normal state lies at the core of the difficulties in formulating a comprehensive theory for high- T_c superconductivity in cuprates. Indeed, in conventional superconductors, a good knowledge of the normal metallic state is a prerequisite for a successful theoretical formulation of the attractive interaction between electrons that leads to superconductivity.

For even higher hole dopings, the standard Fermi liquid behavior is finally retained. There is no sharp boundary between the two regimes.

2.2.1 Fluctuations in the pseudogap phase

Currently, most many-body theories for high- T_c superconductivity assume that the attractive potential in cuprates is mediated by spin fluctuations² As confirmed by

²More recently, the discovery of the charge density wave phase opened the debate on charge fluctuations as an alternative or concomitant mechanism.

both inelastic neutron scattering and resonant inelastic x-ray scattering, these magnetic fluctuations survive for hole doping past the antiferromagnetic phase. They are nevertheless stronger towards zero doping, so one would naively expect T_c to increase towards the antiferromagnetic phase. This expectation is, however, contradicted by experiments featuring a superconducting dome. The critical aspect is that the superfluid density in cuprates is extremely low, leading to a very weak phase stiffness of the superconducting condensate. This aspect starkly contrasts conventional BCS superconductors, where phase fluctuations are hardly relevant.

In connection with the discussion on the BKT instability presented in Subsection 1.5.2, we can expect that what increases towards lower dopings is the mean-field temperature T_{MF} of the superconducting state. In contrast, the fluctuation temperature T_{fl} , correlating with the number of carriers, follows the superfluid density and increases with it. The experimentally manifested critical temperature T_c is the minimum of the two, forming the superconducting dome as shown in Figure 2.7. Furthermore, this behavior justifies the linear increase of T_c with superfluid density for lower dopings, known as Uemura's law [53].

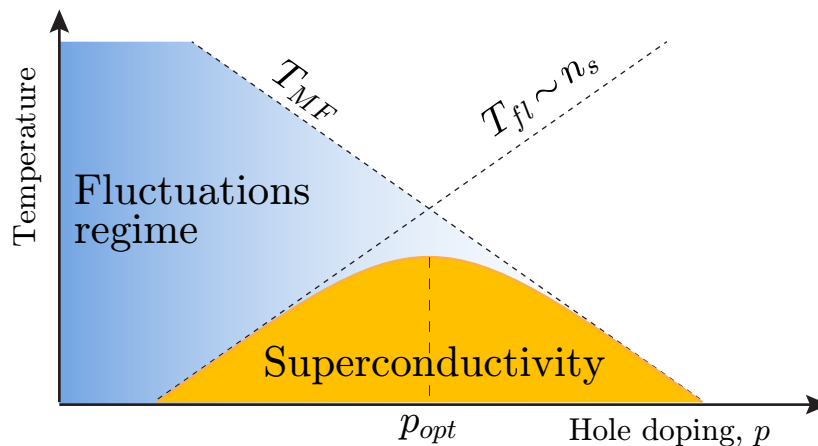


FIGURE 2.7: Towards lower hole dopings, both the amplitude of the pairing and the instability due to fluctuations increase. These two opposite tendencies result in the superconducting dome observed in the phase diagram of most cuprates.

In the underdoped region, for the range of temperatures $T_c < T < T_{MF}$, we therefore expect superconductivity to form locally, just to be shortly after disrupted by fluctuations. This fluctuations-dominated regime corresponds to the pseudogap phase, where signatures of superconductivity without long-range coherence are observed.

Finally, it is important to stress that the concept of BKT instability is, strictly speaking, applicable only to two-dimensional neutral superfluids. The hopping across the Cu_2O layers, even though it is much smaller than in the plane, is still not negligible. Additionally, the interaction with the electromagnetic field, key for superconductors, has to be included in the description. For these reasons, the concepts presented so far

can be applied only qualitatively, and a more comprehensive theory to fully capture the properties of high- T_c cuprates is of utmost importance.

2.3 Superconducting signatures in THz reflectivity

The standard probes for equilibrium superconductivity rely on DC measurements of the electrical resistivity or the magnetic susceptibility. Ultrafast experiments, however, require AC probes with enough time resolution to follow picosecond-fast dynamics. THz frequencies are the ideal range, offering enough time resolution without disrupting the low-energy superconducting condensate.

Experiments are performed by generating short pulses with a carrier frequency in the THz range (e.g., by optical rectification of femtosecond pulses) and guiding them on the material. Using electro-optic sampling (EOS), measuring the reflected electric field in the time domain, it is possible to retain the amplitude and phase information of the frequency-dependent reflectivity without the need for Kramers-Kronig reconstructions. Additionally, knowledge of the absolute value of the impinging electric field is required to derive the sample reflectivity. This calibration can be achieved by self-referencing the incoming THz pulse by having it reflect on a gold mirror, whose response is assumed to be featureless and temperature-independent, placed next to the sample. This practice is often experimentally challenging because, since the EOS measures the pulse in the time domain, it requires a control of the mirror position with an error lower than the pulse wavelength. In practice, it is often sufficient to reference the reflection measured from the superconductor with that measured just above T_c on the same sample. This differential reflectivity is then added to the reflectivity of the normal state obtained by other experimental techniques, such as FTIR spectroscopy. A similar scheme is adopted for the pump-probe experiments presented in Subsection 2.4.2, where the reflectivity induced upon photo-excitation is instead referenced to the non-driven state.

Figure 2.8 shows the optical properties measured along the c -axis of $\text{YBa}_2\text{Cu}_3\text{O}_{6.5}$. σ_1 and σ_2 represent the in-phase and quadrature conductivity, respectively, extracted from the reflectivity with Fresnel relations. Upon superconducting transition, σ_1 , associated with dissipation, is strongly suppressed. All the lost spectral weight (whose integral over all frequencies, according to sum rules, should be conserved) is expected to be shifted to a delta peak at zero frequency, indicative of the DC infinite conductivity typical of superconductors. Since σ_1 and σ_2 are Kramers-Kronig related, the presence of this peak in the former can be inferred from the $\sim 1/\omega$ divergence that appears in the latter. Furthermore, from Equation 1.9, the superfluid density n_s can be obtained from the prefactor of this divergence. Finally, since the measurements are performed along the c -axis, capacitive coupling between the planes gives rise to an additional mode at a finite frequency: the Josephson plasma resonance. In $\text{YBa}_2\text{Cu}_3\text{O}_{6.5}$, its eigenfrequency lies at around 1 THz and is responsible for the edge centered at the same frequency in the reflectivity.

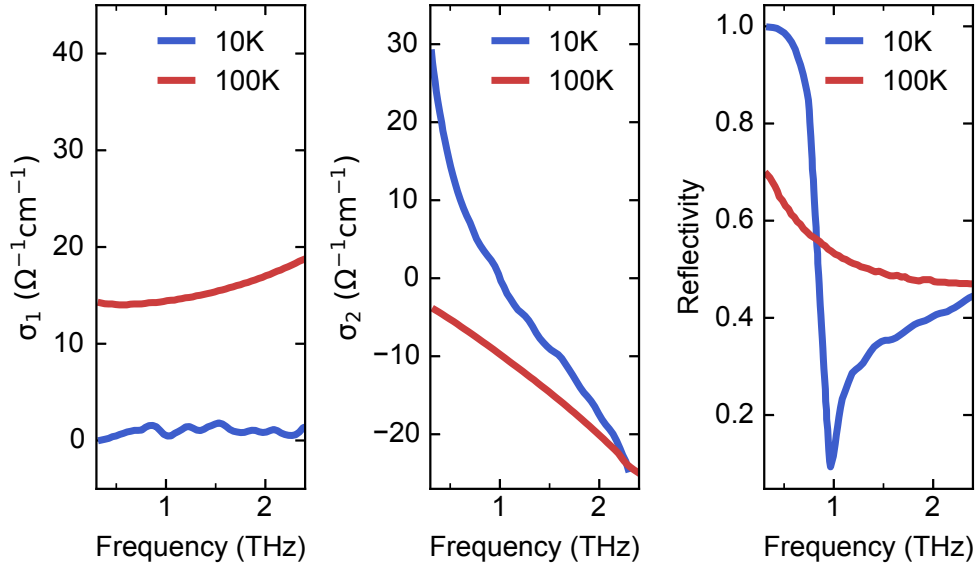


FIGURE 2.8: THz optical features of equilibrium $\text{YBa}_2\text{Cu}_3\text{O}_{6.5}$ measured along the c -axis, in the normal state ($T = 100\text{ K} > T_c$, red curve) and in the superconducting state ($T = 10\text{ K} < T_c$, blue curve). Adapted from [16].

Two important remarks are needed at this stage. First, THz reflectivity is weakly sensitive to changes at DC, which lie outside its bandwidth f_{bw} . For example, instead of a superconductor with delta peak-like conductivity, the photo-excitation could induce a conductor with an atypically high scattering time $\tau \gg 1/f_{bw}$ and a correspondingly narrow Drude peak of width $\sim 1/\tau \ll f_{bw}$. In this case, its optical properties above the peak width would be identical to those of a superconductor. This ambiguity is illustrated in Figure 2.9 by showing the behavior of σ_2 for a superconductor (dashed blue line) and an enhanced conductor (solid red line) with scattering time τ . The observation of a $\sim 1/\omega$ diverging σ_2 in THz reflectivity rather sets a lower limit to the Drude scattering time of a metal to about 1 ps. This value is still remarkable, especially considering that the same quantity in room temperature copper is about two orders of magnitude higher.

Second, to explain the delta peak in the σ_1 and corresponding $\sim 1/\omega$ divergence in the σ_2 , a Drude metal with infinite (or very high) scattering time is sufficient. This is the same scenario leading to the derivation of the *First London Equation* 1.9, whereas the Meissner effect appears only in the *Second London Equation* 1.11. Contrary to a common misconception, no notion of the Meissner effect or other magnetic-related properties is required to reproduce these optical features. For this reason, THz reflectivity can be considered analogous to transport measurements, and the ultrafast magneto-optical techniques introduced in Chapter 3 are required to characterize the magnetic properties of driven superconductors.

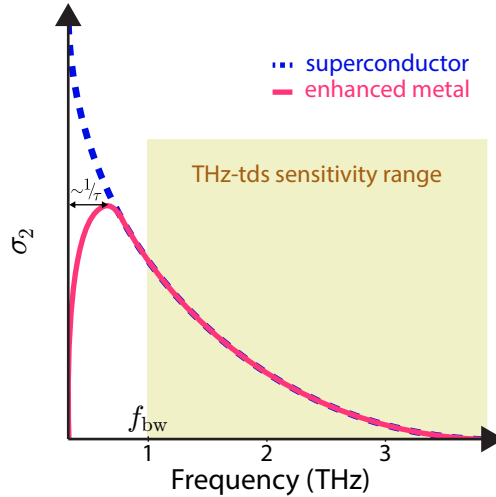


FIGURE 2.9: Ambiguity of THz measurements in discerning superconductors from metals with enhanced scattering time. THz-tds: THz time-domain spectroscopy.

2.4 Ultrafast control of superconductivity

Since the early days of ultrafast physics, the control of the superconducting order (and other quantum phases) has been at the heart of this field. This research was uncharted territory, especially considering that superconductivity is a state that is almost exclusively described at equilibrium, and little is known regarding the laws determining its dynamical onset.

2.4.1 Disruption of superconductivity with optical pulses

On the left of Figure 2.10, the experimental configuration of the study in [54] is shown. A $\text{YBa}_2\text{Cu}_3\text{O}_7$ sample is irradiated with optical light ($\lambda = 800 \text{ nm}$), and the evolution of its optical properties is tracked with a THz pulse in a pump-probe fashion. Both pulses are polarized in-plane, and the pump is expected to strongly couple to the electronic degree of freedom of the system.

The measured σ_2 at equilibrium (red) and on the peak of pump-probe response (blue) are shown in the middle panel. The base temperature is 10 K, well below the critical temperature $T_c \sim 90 \text{ K}$. Upon photo-excitation, there is a clear quench of the $\sim 1/\omega$ divergence, indicative of disruption of the superconducting state. As mentioned in Section 2.3, from the prefactor of the divergence, it is possible to extrapolate the superfluid density $n_s \propto \omega \sigma_2(\omega)|_{\omega \rightarrow 0}$. The right panel shows this quantity for different pump-probe delays, where the zero of the delay is referenced with the arrival of the pump. It is clear that, upon excitation, the superfluid density is suddenly lowered and then slowly recovers over a few picoseconds. The time constant of the recovery has been shown to progressively increase from 1.5 ps at 4 K to 3.5 ps near T_c , correlating well with the closing of the superconducting gap.

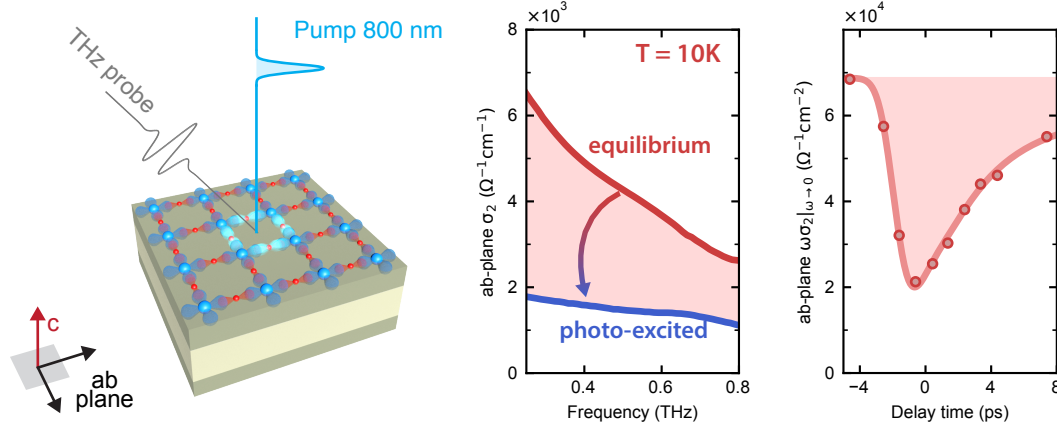


FIGURE 2.10: Disruption of superconductivity with optical pulses. Data extracted from [54]. Material from [55].

2.4.2 Light-induced superconductivity

More recently, a series of experiments attempted to enhance the superconducting state rather than disrupt it [14, 15, 16, 17]. In Figure 2.11 one such representative experiment on $\text{YBa}_2\text{Cu}_3\text{O}_{6.5}$ is shown. In this case, the drive lies in the MIR frequency range and is resonant with the apical oxygen modes of the system (see Section 2.1.1). As mentioned in Section 2.1, the position of these atoms is strongly related to the onset of superconductivity. The pump is then polarized out-of-plane, and the THz optical properties are measured along the same direction (see left panel). In the middle and right panel, the same quantities as in Figure 2.10 are shown. In this case, however, the base temperature is $T = 100 \text{ K} > T_c$. Upon photo-excitation, σ_2 develops the $\sim 1/\omega$ divergence typical of equilibrium superconductors. The extracted superfluid density n_s increases from zero to a finite value and then decays back to the equilibrium value over a few picoseconds. It is important to notice that the driven state does not possess intrinsic rigidity, meaning it immediately decays back once the drive is over.

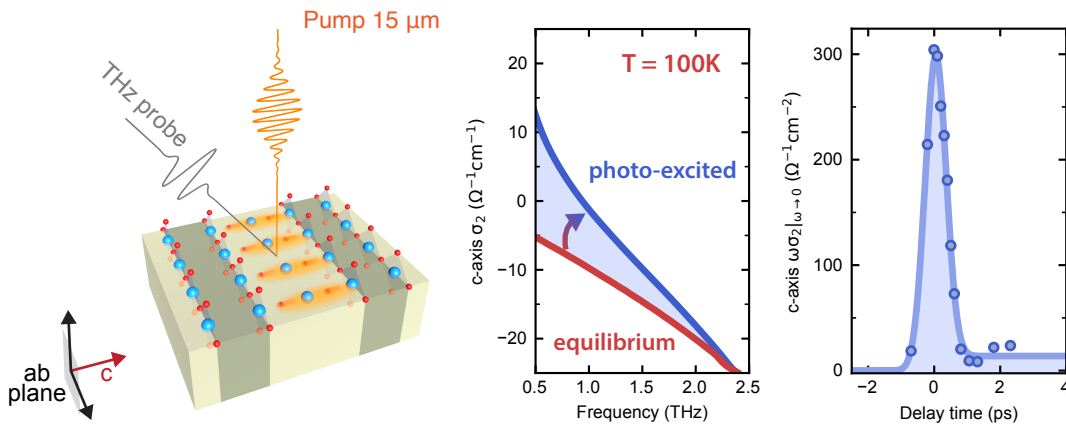


FIGURE 2.11: Enhancement of superconductivity with MIR pulses. Data extracted from [16]. Material from [55].

Qualitatively similar transient optical features were also detected in other cuprate compounds [6, 7, 8] and two families of organic superconductors: the charge-transfer salt κ -(BEDT-TTF) $_2\text{Cu}[\text{N}(\text{CN})_2]\text{Br}$ (abbreviated as κ -Br) [9, 10] and the alkali-doped fullerene K_3C_{60} [11, 12, 13]. The proposed mechanism leading to light-induced superconductivity depends on the system under study. For the single layer cuprates $\text{La}_{2-x}\text{Ba}_x\text{CuO}_4$ and $\text{La}_{1.675}\text{Eu}_{0.2}\text{Sr}_{0.125}\text{CuO}_4$, the current evidence points towards a “melting” of a competing order. In this scenario, the light selectively disrupts the stripe order, which would otherwise suppress the superconducting T_c .

This mechanism is less applicable to $\text{YBa}_2\text{Cu}_3\text{O}_{7-\delta}$. Indeed, the charge order disappears above 200 K (see phase diagram 2.6), whereas the light-induced superconducting features are present up to room temperature and above. Doping and temperature dependencies [56] correlate this effect with the pseudogap phase. In this case, the role of light might be to impart coherence to the fluctuating superconducting order that is made unstable in the underdoped region of this compound. A similar scenario seems to apply to K_3C_{60} and κ -Br. In both systems, observing a vortex Nernst effect above T_c indicates the presence of preformed superconducting pairs, which seems to be a prerequisite for observing light-induced superconductivity.

At this point, two questions arise naturally: “How does driving the phonons lead to superconductivity?” and “Does it work with any phonon?”. The first question is more complicated because it is related to the microscopic mechanism in action, but the second can be straightforwardly verified in experiments.

2.4.3 Pump frequency dependence

In order to understand which phonons were responsible for light-induced superconductivity, the pump frequency dependence of the response in $\text{YBa}_2\text{Cu}_3\text{O}_{7-\delta}$ has been carefully investigated in [16]. This study has been possible upon the development of a high amplitude, narrowband band MIR source continuously tunable between 4 THz and 20 THz [57].

In this study, the pump fluence and duration have been kept constant at a value of 8 mJ cm^{-2} and 600 fs, respectively, corresponding to an electric field peak amplitude of $\sim 3 \text{ MV cm}^{-1}$. On the top panel of Figure 2.12, the spectrally integrated dissipative component of the pump-probe differential response $\int \Delta\sigma_1(\omega) d\omega$ is plotted. As a comparison, the dashed line represents the same quantity computed at equilibrium between the base temperatures of 100 K and 200 K. As expected, the different peaks visible match with the IR-active phonon modes of the material (see Figure 2.3). As figure of merit for the superconducting response, we take again the extrapolated superfluid density $n_s \propto \omega\sigma_2(\omega)|_{\omega \rightarrow 0}$, which is plotted on the bottom panel of Figure 2.12. In this case, the dashed line represents the value of the superfluid density measured at equilibrium well below T_c , at 10 K. Quite remarkably, signatures of superconducting transport are present only when driving the apical oxygen phonon modes. This observation suggests the non-thermal origin of the effect since it shows how it is not

enough to deposit energy in the system. Instead, the selective drive of specific phonon modes is required.

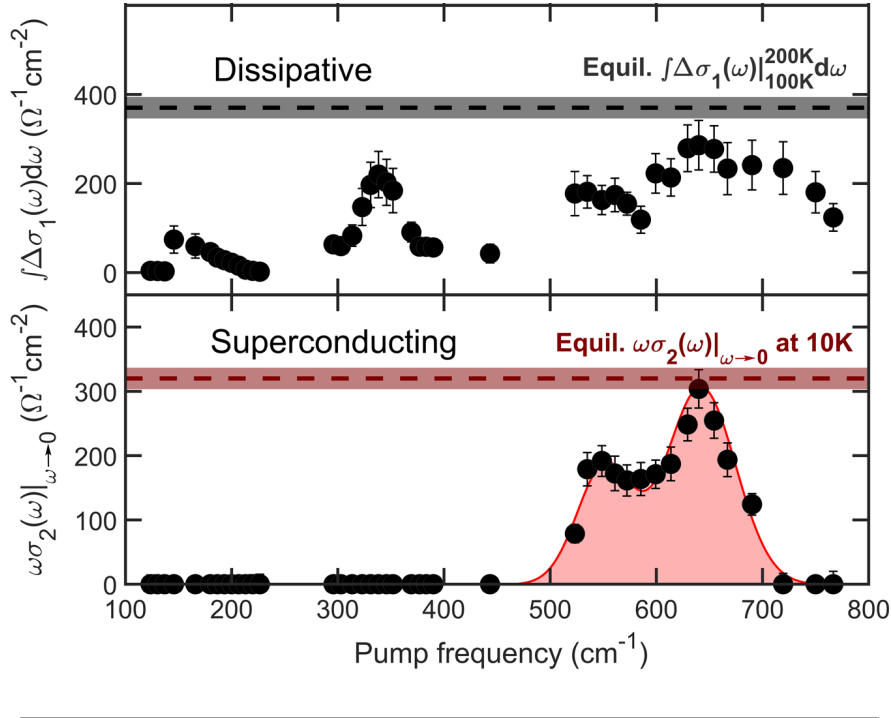


FIGURE 2.12: Pump frequency dependence of optical properties of $\text{YBa}_2\text{Cu}_3\text{O}_{6.5}$. From [16].

2.4.4 Josephson plasmons amplification

A step forward in understanding the microscopic mechanism leading to the observed THz properties in $\text{YBa}_2\text{Cu}_3\text{O}_{6.48}$ was provided by a series of beautiful studies regarding Josephson plasmons amplification in this same system [56, 58].

Instead of investigating the low-energy properties of the driven state with THz light, these experiments measured the Second Harmonic Generation (SHG) of an optical pulse reflecting off the sample. Since the material is centrosymmetric, this should be zero by symmetry³.

The action of the MIR pump breaks this symmetry. Its frequency is tuned to drive the same IR-active modes that led to the transient THz properties presented in Subsection 2.4.2. The nonlinear coupling between the driven IR mode at frequency ω_{IR} , and the probe field at frequency ω_{pr} , generates a hyper-Raman polarization

$$P^{(3)}(2\omega_{pr} \pm \omega_{IR}) \propto \frac{\partial \chi^{(2)}}{\partial Q_{IR}} Q_{IR}(\omega_{IR}) E_{pr}^2(2\omega_{pr}) \quad (2.2)$$

If the probe beam duration τ is shorter than the driven mode period $T_{IR} = 2\pi/\omega_{IR}$, for every pump-probe delay t , the probe interrogates a snapshot of the

³This argument is no longer valid when considering that, for a finite angle of incidence, the surface boundary breaks this symmetry. However, this effect, known as Surface SHG, is ordinarily small and can be neglected.

medium where the inversion symmetry has been broken. In this limit, we can define an effective second-order susceptibility

$$\chi_{eff}^{(2)}(t) := \frac{\partial \chi^{(2)}}{\partial Q_{IR}} e^{i\omega_{IR}t} \quad (2.3)$$

oscillating at the frequency of the driven mode and generating a delay-dependent field close to the second harmonic of the probe pulse $2\omega_{pr}$. This field is then detected in a heterodyned or homodyned configuration by, respectively, overlapping it or not with a reference second harmonic beam generated before the sample. In the former configuration, the time-delay-dependent intensity measured on the photodetector is proportional to the amplitude of the driven modes, whereas in the latter to its square. Depending on the intensity of the reference beam, both contributions can be present at the same time.

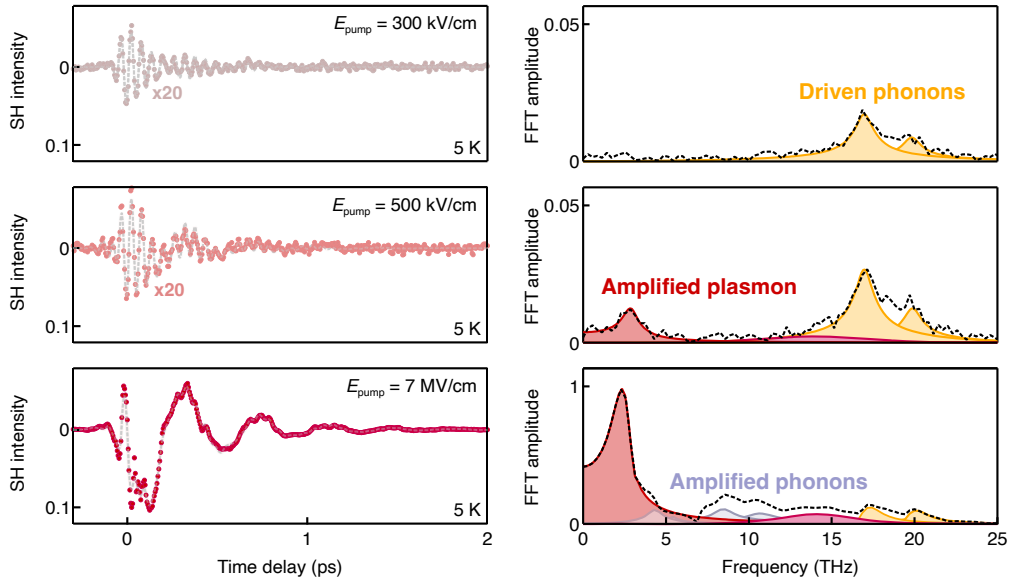


FIGURE 2.13: IR-active modes coherently driven by the pump observed with SHG. As the driving field is increased, an amplification of the phonon and plasmon modes is observed. From [56].

On the left side of Figure 2.13, the time-dependent effective second harmonic is plotted for three different driving fields: 300 kV cm^{-1} , 500 kV cm^{-1} and 7 MV cm^{-1} . The plots on the right show the corresponding Fourier transforms. For low values of the driving fields, only the phonon modes resonant with the pump are observed. As the amplitude of the field is increased, different IR-active modes at lower frequencies, of either phononic or electronic nature, appear. Of particular interest are the low-energy electronic modes, which are associated with tunneling between the superconducting CuO_2 layers and known as *Josephson plasmons*.

The intensity dependence of the conversion from high-energy phonons to low-energy plasmons suggests a nonlinear coupling between modes similar to the one described by Equation 2.1. As interaction Hamiltonian V_i , two choices are possible,

corresponding to two different pathways for this conversion. The first possibility corresponds to a three-way mixing between one driven phonon Q_{IR} and pairs of intra- and inter-layer Josephson plasma polaritons at finite and opposite momenta J_{P1}^{+qJP} and J_{P2}^{-qJP}

$$V_i^{3w} \propto q_x^2 Q_{IR} J_{P1}^{+qJP} J_{P2}^{-qJP}$$

where the plasmons are excited with a finite in-plane momentum q_x , which is determined by energy and momentum conservation. Alternatively, the coupling to the plasmons can be explained by a four-way mixing between the two apical phonon modes (see Subsection 2.1.1), resonantly excited by the MIR pump, and pairs of finite-momentum interlayer Josephson plasma polaritons. The interaction Hamiltonian, in this case, reads

$$V_i^{4w} \propto (Q_{IR1} + Q_{IR2})^2 J_P^{+qJP} J_P^{-qJP}$$

These two scenarios, which are not distinguishable in the measurements presented so far, can be disentangled by driving the system with two MIR pulses instead of one. By controlling their relative delay, it is possible to investigate the coherent response of the system to different excitation colors. This approach, closely related to 2D spectroscopy, has proven that the mechanism responsible for the observed amplification of Josephson plasmons is based on four-wave mixing [58].

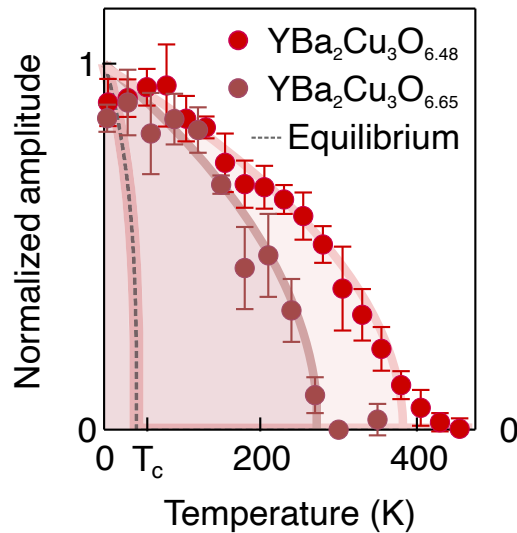


FIGURE 2.14: Temperature dependence of the Josephson plasmon amplification for selected dopings. From [56].

In the proposed theoretical model [59], this effect arises as an amplification of pre-existing fluctuations of the Josephson plasmons polaritons. Experimental observations corroborate this picture. Figure 2.14 shows the temperature dependence of the amplitude of the effect, performed on two different dopings: $\text{YBa}_2\text{Cu}_3\text{O}_{6.48}$ and $\text{YBa}_2\text{Cu}_3\text{O}_{6.65}$. Remarkably, they exhibit a mean-field behavior scaling with the respective pseudogap temperature T^* (see Section 2.2).

Chapter 3

Ultrafast Optical Magnetometry

The core of this thesis work is the development of the Ultrafast Optical Magnetometry (UOM) experimental technique. The idea of sampling the magnetic field with light pulses to track magnetic dynamics is not new, and in some cases, it has also been applied to the study of superconductors [60, 61, 19]. In these studies, a laser pulse is propagating through a Faraday-active material, which acts as detector. The polarization rotation of the beam encodes the magnetic field inside the detector in the instant that the pulse is traversing it. By delaying the probe pulse with respect to the pump pulse that triggers the dynamics, it is possible to reconstruct the time evolution of the magnetic field.

However, the time resolution is limited by the type of detector used, whose properties determine the onset of the Faraday response. All the measurements performed so far on superconductors have been carried out with ferrimagnetic detectors, with a time resolution of order ~ 100 ps. This resolution is two orders of magnitude slower than the typical dynamics of light-induced superconductivity, which develops over time scales of order ~ 1 ps (see THz measurements in Subsection 2.4.2). On the other hand, diamagnetic detectors have proven effective at following THz dynamics [62]. Their use comes at the expense of a significantly lower sensitivity, requiring more careful experimental techniques to suppress all other spurious contributions that may conceal the magnetic signal.

3.1 Origin of the Faraday effect

In the following section, we discuss the origin of the Faraday effect¹. We consider a plane wave propagating along z and linearly polarized along x . On the negative half of the z -axis, the medium is vacuum, and the wave electric field can be expressed as the superposition of two circularly polarized components

$$\mathbf{E}(z, t) = E_0 \mathbf{e}_x e^{i(\omega t - kz)} = E_0 [\mathcal{O} + \mathcal{O}] e^{i(\omega t - kz)} \quad z < 0 \quad (3.1)$$

¹To understand magneto-optic sampling, knowing what causes the Faraday effect is not needed. It is sufficient to believe the experimental observation that the polarization rotation is linear in a magnetic field, and this effect is stronger in some materials than others. However, knowledge regarding the physical origin of this effect can help design more sensitive and faster detectors.

where the right circular polarization (RCP) and left circular polarization (LCP) basis vectors are defined as

$$\mathbf{O} := \frac{1}{2}(\mathbf{e}_x + i\mathbf{e}_y) \quad \mathbf{O} := \frac{1}{2}(\mathbf{e}_x - i\mathbf{e}_y) \quad (3.2)$$

At $z = 0$, the light enters a medium with a *magnetic circular birefringence*, that is a difference between the refractive index for the RCP and LCP components, indicated as $n_{\mathbf{O}}$ and $n_{\mathbf{O}}$, respectively. We ignore Fresnel reflections, which are more relevant to the magneto-optic Kerr effect (MOKE). After propagation over a distance z , the RCP component picks up a phase delay δ relative to the LCP one equal to

$$\delta(z) = \frac{2\pi(n_{\mathbf{O}} - n_{\mathbf{O}})z}{\lambda} \quad (3.3)$$

The electric field at a distance z inside the medium reads

$$\mathbf{E}(z, t) = E_0 \left[\mathbf{O}(z, t)e^{-i\delta(z)/2} + \mathbf{O}(z, t)e^{+i\delta(z)/2} \right] e^{i(\omega t - \frac{2\pi n}{\lambda}z)} \quad (3.4)$$

where n now represents the average refractive index. Transforming back to the linear basis with relations 3.2 yields

$$\mathbf{E}(z, t) = E_0 \left[\cos \frac{\delta(z)}{2} \mathbf{e}_x + \sin \frac{\delta(z)}{2} \mathbf{e}_y \right] e^{i(\omega t - \frac{2\pi n}{\lambda}z)} \quad (3.5)$$

The polarization state obtained is still linear. Upon exiting the medium of length L , the polarization plane is rotated, compared with the initial one 3.1, by an angle

$$\theta_F = \frac{\delta(L)}{2} = \frac{\omega L}{2c}(n_{\mathbf{O}} - n_{\mathbf{O}}) \quad (3.6)$$

Linear birefringence in the crystal, so far neglected, can introduce a phase delay between light linearly polarized along different directions instead, introducing ellipticity in the beam. Furthermore, circular dichroism can have similar effects by attenuating differently right and left circular polarized light. We neglect both these effects for the moment.

Becquerel gave a classical justification for the difference in refractive index ($n_{\mathbf{O}} - n_{\mathbf{O}}$). He considered that an applied magnetic field affects the electrons responsible for the refractive index by setting them in a circular motion at the Larmor frequency

$$\omega_L = \frac{q_e}{2m_e c} B \quad (3.7)$$

In their reference system, the incoming electric field appears red-shifted for circular co-rotating waves and blue-shifted for circular counter-rotating waves. This Doppler-like frequency shift for the electrons accounts for the difference in refractive index for RCP and LCP light. To first approximation, the frequency-shifted refractive index can be expressed as

$$n_{\mathbf{O}/\mathbf{O}} = n(\omega \pm \omega_L) \approx n(\omega) \pm \frac{dn}{d\omega} \omega_L \quad (3.8)$$

which, for typical magnetic fields, implies a relative shift much smaller than unity. Plugging expressions 3.7 and 3.8 back into 3.6 gives

$$\theta_F = -\frac{q_e \omega}{2m_e c^2} \frac{dn}{d\omega} BL = \frac{q_e \lambda}{2m_e c^2} \frac{dn}{d\lambda} BL \quad (3.9)$$

where the last expression is written in terms of the vacuum wavelength $\lambda := 2\pi c/\omega$. As confirmed by experiments, the Faraday rotation is then proportional to the magnetic field and the length of the medium. The proportionality constant, and figure of merit for the sensitivity of magneto-optic detectors, is the *Verdet* constant V . In the Becquerel derivation, it is equal to

$$V = \frac{q_e \lambda}{2m_e c^2} \frac{dn}{d\lambda} \quad (3.10)$$

This derivation applies qualitatively well for diamagnetic materials, where the Larmor precession assumed here is also at the origin of the material magnetization. Faraday rotation and magnetization are indeed closely related. In practice, material-dependent multiplicative or additive factors are included in the Verdet constant in 3.10 to account for deviations in experiments. These can be interpreted in terms of a renormalization of the mass of the electrons m_e in band theory. This derivation fails completely for ferro- and ferrimagnetic materials, where a full quantum description is required to even qualitatively capture the magnetization of the medium.

3.1.1 Ferrimagnetic, diamagnetic, and paramagnetic detectors

When designing an experiment, a number of factors have to be taken into account for an optimal choice of Faraday detector. Ferrimagnetic crystals, such as Bi:Y₃Fe₅O₁₂, EuS, or EuSe, offer by far the highest sensitivity ($V \sim 10^5$ rad) [18, 61]. Due to the presence of ferrimagnetic domains, their sensitivity can have strong spatial gradients. Their main drawback is the limited time resolution, down to 100 ps at best, due to the presence of low-lying magnetic excitations (e.g. ferromagnetic resonance) at sub-THz frequencies. For this reason, they are best suited for equilibrium or slow-dynamics measurements.

Diamagnetic II-VI and III-V semiconductors such as ZnSe, ZnTe, and GaP have two to three orders of magnitude smaller sensitivity than ferrimagnetic materials. For example, in Figure 3.1, the Faraday angle of an 800 nm laser pulse traversing in double pass a 70 μ m-thick GaP crystal at 100 K is plotted as a function of an external magnetic field. These conditions are relevant for the experiments presented in Chapter 4. As expected, the dependence is linear, and from the slope of the curve, the Verdet constant of the material is estimated as $V \sim 120$ rad T⁻¹ m⁻¹, comparable with literature values [63]. This significantly lower Verdet constant imposes severe limitations in experiments. First, the crystal thickness needs to be significant to accumulate a higher Faraday angle, with negative repercussions on the spatial and temporal resolutions (see Sections 3.3 and 3.4). Second, due to the weak signal,

great care must be invested into suppressing all other spurious contributions that may overwhelm the small Faraday rotation (see Subsection 3.2.3). The great advantage of diamagnetic detectors lies in their fast response. Careful studies with THz pulses in GaP detectors showed a response time lower than ~ 1 ps [64, 62]. Therefore, despite the lower sensitivity, they are the preferred choice in the study of magnetic fields changing over ultrafast timescales.

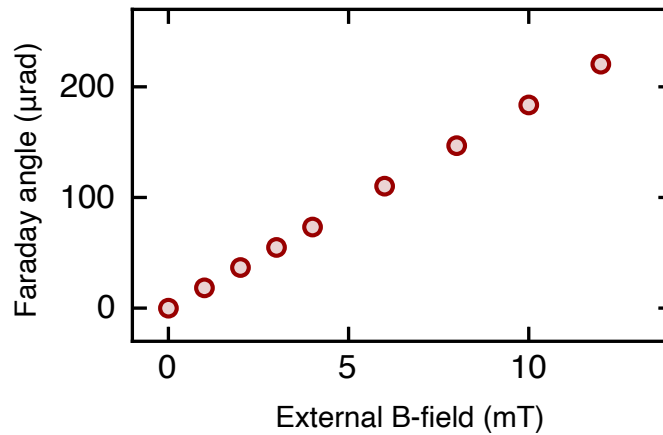


FIGURE 3.1: Faraday rotation measured in a 70 μm -thick GaP crystal, in double pass, for different values of the external magnetic field. Material from [55].

Paramagnetic detectors, such as Terbium Gallium Garnet (TGG), Gadolinium Gallium Garnet (GGG), $\text{Cd}_{1-x}\text{Mn}_x\text{Se}$ (CMS) or $\text{Cd}_{1-x}\text{Mn}_x\text{Te}$ (CMT) lie somewhere in between ferrimagnetic and diamagnetic detectors. Due to the presence of diluted magnetic ions, their magnetization can be significantly stronger than diamagnets, yielding Verdet constants up to two order magnitudes higher in absolute value. This difference is evident when comparing the Faraday rotation measured in two paramagnetic crystals with that of a standard diamagnetic detector such as ZnTe (see Figure 3.2). For the 800 nm wavelength used, the Verdet constant is seen to be comparable (TGG) or significantly higher (CMT), on top of being of opposite sign. Furthermore, since they do not present magnetic domains, their Faraday rotation is spatially flat and reliably controllable with external fields. They are, therefore, frequently used in applications as Faraday isolators in conjunction with a permanent magnet.

Their time response is, however, debated. For example, theoretical studies on CMT predicted that its time response is set by spin-spin interaction [65], which for a Mn doping $x > 0.5$ should be $\sim 1 - 10$ ps. A subsequent experimental study claimed the magneto-optical tracking of a short pulse with ~ 1 ps time resolution [66, 67]. However, further polarization studies showed how the probe beam was rather sampling the electric field component of the pulse, with a negligible magnetic sensitivity at those high frequencies [68]. Electric and magnetic field sampling can be discerned based on symmetry, as shown in Subsection 3.2.4. This initial mistake underscores the strong

frequency dependence of the Verdet constant in ordered magnetic media and the importance of polarization analysis in magneto-optic sampling.

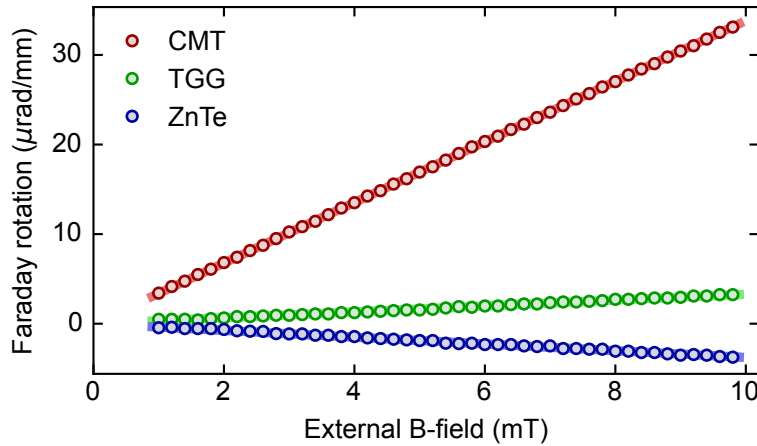


FIGURE 3.2: Comparison of Faraday rotation in CMT and TGG paramagnetic crystals at 800 nm, with that of the diamagnetic ZnTe.

3.1.2 Frequency dependence of the Verdet constant

From the expression 3.10, we expect the Verdet constant to dramatically increase close to an absorption edge, where the refractive index abruptly changes from positive to negative. This feature is indeed observed in experiments. However, in that same frequency range, the strong absorption of light, which lowers the transmitted signal, and the strong circular dichroism, which makes it elliptical, are often detrimental to measurements. These two opposite tendencies are summarized in Figure 3.3. The polarization rotation and transmission of a continuous-wave (CW) linearly polarized beam through a 300 μm -thick GaP crystal are characterized for three different wavelengths. The lowest ($\lambda = 532 \text{ nm}$) presents the highest Verdet constant, but only 0.1% of the light is transmitted. For the other two wavelengths ($\lambda = 635 \text{ nm}$ and 785 nm), the absorption is already negligible, but there is still a substantial difference in their Faraday rotations. Indeed, applying Equation 3.10 to a Lorentz model describing the medium, close to resonance the Verdet constant scales as $\sim (\lambda_0 - \lambda)^{-1}$, where λ_0 in GaP is at 553 nm, whereas the absorption scales as $\sim (\lambda_0 - \lambda)^{-2}$. The latter decays faster than the former. In practice, the ideal implementation consists of a probe frequency close enough to the absorption edge to benefit from the enhanced Verdet constant but far enough to avoid significant absorption.

3.2 Magneto-optic sampling

Magneto-optic sampling (MOS) is the magnetic analogous of the better known electro-optic sampling (EOS). As the name suggests, this technique encodes the instantaneous value of the magnetic field in the probe beam polarization state. The latter is linearly

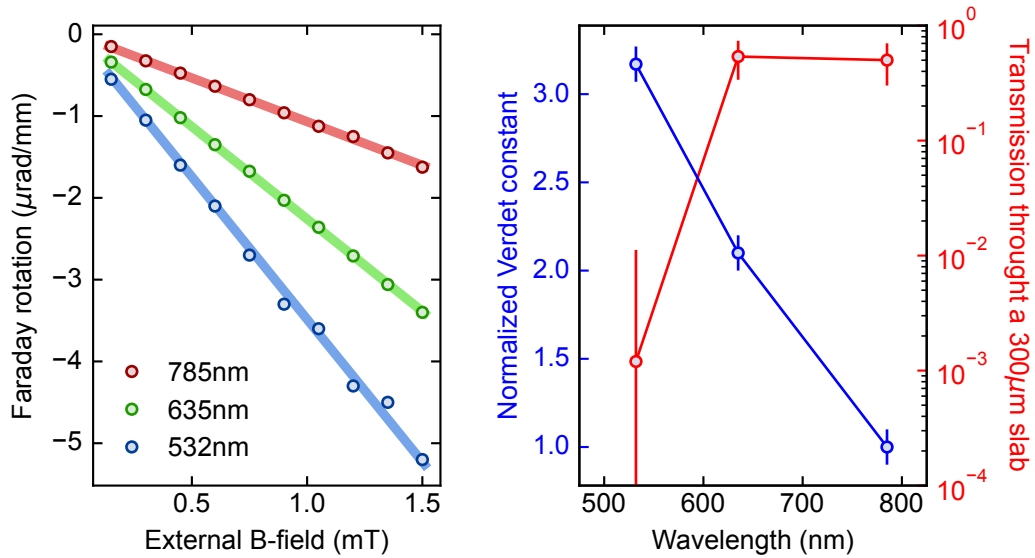


FIGURE 3.3: Faraday rotation and transmission measured in GaP for three different wavelengths. The Verdet constant increases closer to the absorption edge $\lambda_0 = 553$ nm, whereas the transmission significantly decreases.

proportional to the former by virtue of the Faraday effect discussed in Section 3.1. To maximize the sensitivity of the technique, it is advantageous to sample the magnetic field inside a medium with a strong Verdet constant, referred to as “detector”. The small contribution to the polarization rotation due to air is negligible. Therefore, the magnetic field is sampled only in a region delimited by the detector. This detector is usually placed in proximity to the sample to study near-field effects since a free propagating wave would be more readily studied by sampling its electric field component with EOS.

In some cases, the polarization rotation can be measured directly in the sample instead of a separate detector. This arrangement offers an experimentally simpler configuration, especially advantageous for thin films since it lowers the effect of demagnetizing fields (see Subsection 1.1.5). It is, however, more ambiguous, especially in pump-probe experiments, where it is much harder to disentangle changes in magnetic field from those to the Verdet constant of the material. Furthermore, having a separate detector is required in the study of superconductors since they do not present a Faraday effect due to the time-reversal symmetric Meissner state.²

3.2.1 Reflection and transmission configurations

In experiments, two main configurations are customarily employed. These are shown in Figure 3.4. They differ in whether the outgoing sampling beam exits the crystal on

²This statement is correct in the bulk of type-I superconductors, where the field is completely screened. Shielding currents at the edges or vortices in type-II superconductors break this symmetry and can give rise to a finite Verdet constant. The magnetic field associated with the superconducting diamagnetic response discussed in the following sections has the same origin.

the same or opposite side as the incoming one. If the Faraday rotation is measured directly in the sample and not in a separate detector, the most convenient arrangement is in transmission. This arrangement allows the beam to enter the crystal at normal incidence and does not require any precise alignment between the sample and the detector. In order to filter out undesired reflections that may lower the magnetic contrast of the measurement, a wedge is often introduced in the sample. As discussed previously, this configuration is often ambiguous or unsuited for some experiments.

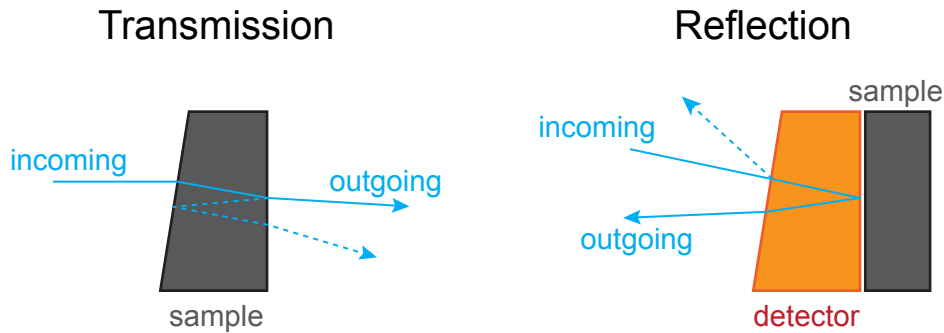


FIGURE 3.4: Transmission and reflection configuration for MOS. The presence of a wedge allows for the filtering of undesired reflections.

Alternatively, in the reflection geometry, the probe beam traverses twice the detection crystal by getting reflected from its back surface. In the reference frame of the propagating beam, both the accumulated Faraday rotation and the direction of the magnetic field are reversed upon reflection. Consequently, the additional Faraday rotation in the second pass adds to that acquired in the first, yielding twice the polarization rotation compared to the transmission case. The great advantage of this configuration is that it requires optical access only on one side of the detector and allows the placement of the sample on the other. Similarly to the previous case, a wedge allows filtering out undesired reflections.

Anti-reflection and high-reflection coatings can significantly increase the amount of probe light collected, especially in the reflection geometry where most of the light is typically lost in undesired reflections. Ideally, this solution makes the wedge superfluous. This simpler design comes, however, with great risks. Dielectric coatings may introduce significant strain upon cooling, which can introduce strong birefringence and affect the polarization state of light in a non-controllable way. Metallic coatings, due to the presence of free electrons, build up eddy currents in response to magnetic fields. As a result, they behave as low-pass filters for the magnetic signal. Ultimately, the use of coatings depends on the application at hand. None were used in this thesis work.

Finally, it is important to note that, despite the confusion that their name may cause, both reflection and transmission configurations rely on the Faraday effect and not on the magneto-optic Kerr effect. Indeed, in both cases, the polarization rotation accumulated from the beam happens by propagating in transmission through the

medium. In comparison, the reflection from the back surface has negligible effects on the polarization state of the sampling beam.

3.2.2 Polarization analysis

In order to analyze the Faraday polarization rotation, different methods are available (see [69], Section 4.2). One of the most sensitive relies on balanced detection. In this configuration, the Faraday rotation accumulated in the detection crystal is measured by splitting the beam into two orthogonal components with a Wollaston prism and measuring their intensity difference (see Figure 3.5).

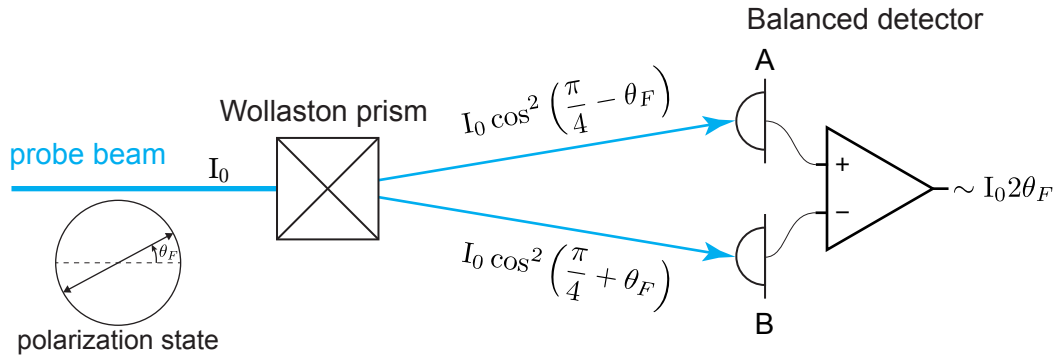


FIGURE 3.5: Polarization analysis for MOS. The Faraday angle θ_F is quantified by splitting the beam into two orthogonal components and measuring their intensity difference.

The incoming beam, of intensity I_0 , has its polarization referenced with a polarizer placed before the detector. Its polarization lies along the diagonal of the Wollaston prism so that, without the detector, the beam would be equally split into the two orthogonal branches, which we call A and B, and their difference would be zero. For this reason, this arrangement is called *quasi-balancing* configuration. By adding the detector, the Faraday rotation θ_F changes the balance between the two branches so that

$$I_A = I_0 \cos^2\left(\frac{\pi}{4} - \theta_F\right) \quad I_B = I_0 \cos^2\left(\frac{\pi}{4} + \theta_F\right) \quad (3.11)$$

For $\theta_F \ll 1$, which is the typical case in experiments, their difference can be expressed as

$$I_A - I_B = I_0 \left[\cos^2\left(\frac{\pi}{4} - \theta_F\right) - \cos^2\left(\frac{\pi}{4} + \theta_F\right) \right] \approx I_0 2\theta_F \quad (3.12)$$

This quantity is normally measured by a balanced photodetector, which computes this difference electronically with great precision, optionally with a gain G . The balanced detector also outputs the sum of the two channels, equal to I_0 , which can be used to normalize the difference signal 3.12. This way, the output signal is independent of

intensity fluctuations on the probe signal

$$\frac{I_A - I_B}{I_A + I_B} \approx 2\theta_F \quad (3.13)$$

For probe polarization-dependent measurements, the polarization state of the incoming light can be controlled by rotating the polarizer placed before the detector. In these cases, the light entering the polarizer can be set circular with a quarter-wave plate to have a flat intensity profile for every polarization. Remaining in the quasi-balanced configuration would require to rotate the Wollaston prism for every incoming polarization. This solution is not practical because it affects the beam alignment past it. Instead, a half-wave plate with its major axis aligned at half the angle of the incoming polarization and placed before the Wollaston prism can be used to set the light polarization back to the quasi-balancing configuration. The joint half-wave plate and Wollaston prism can be thought of as splitting the light along two new orthogonal axes, rotated with respect to the original configuration by the same angle as the incoming polarization.

In reality, the Faraday effect also introduces a small ellipticity in the probe beam due to circular dichroism, which has so far been neglected. Strain in the detection crystal is also a source of ellipticity, which is important to monitor because it can compromise the assumption of linear polarized light required for MOS. For these reasons, measuring the probe beam ellipticity is also highly desirable. This inspection can be achieved, similarly to EOS, by placing a quarter-wave plate between the half-wave plate and the Wollaston prism, with its major axis aligned along the diagonal of the Wollaston prism. The joint effect of the quarter-wave plate and Wollaston prism is to split the beam in ratios proportional to its right and left circular intensity components. This configuration is not sensitive to Faraday rotation since the latter predominantly adds a relative phase between the two circular components. Instead, it is sensitive to ellipticity, which originates from a phase delay between the linear components.

3.2.3 Suppression of spurious contributions

The balanced detection scheme introduced in the previous section routinely allows measuring Faraday angles with a precision of $\sim 10^{-8}$ rad. In order to push its sensitivity even further, numerous technical measures are possible. They rely on removing all the possible sources of polarization noise from the measurement, either random or systematic.

A significant improvement is obtained when performing the experiment in a vacuum chamber rather than a simple cryostat. This approach is beneficial when applying an external field with a coil. The reason is that the cryostat windows also possess a Verdet constant, and if they are close to the coil, they can contribute to the Faraday rotation. This source of noise is particularly troublesome because it appears at the

same modulation frequency of the coil. Furthermore, when subject to vacuum pressure, the windows can develop significant strain-induced birefringence, adding to the polarization noise of the probe beam.

Similarly, another source of polarization noise is due to the mirrors between the reference polarizer and the Wollaston prism, respectively setting and analyzing the beam polarization state. In this case, pointing noise can change the angle of incidence of the beam, which is converted into ellipticity noise. All these contributions can be removed by placing the polarizer and Wollaston prism inside the vacuum chamber directly before and after the detection crystal, as shown in Figure 3.6. This allows to clearly define the polarization state of the light prior to MOS and analyze it before the mirrors can influence its polarization state. The intensity noise of the light source is less of a problem since, as noted above, the intensity is monitored by the balanced detector and is used to normalize the balancing signal.

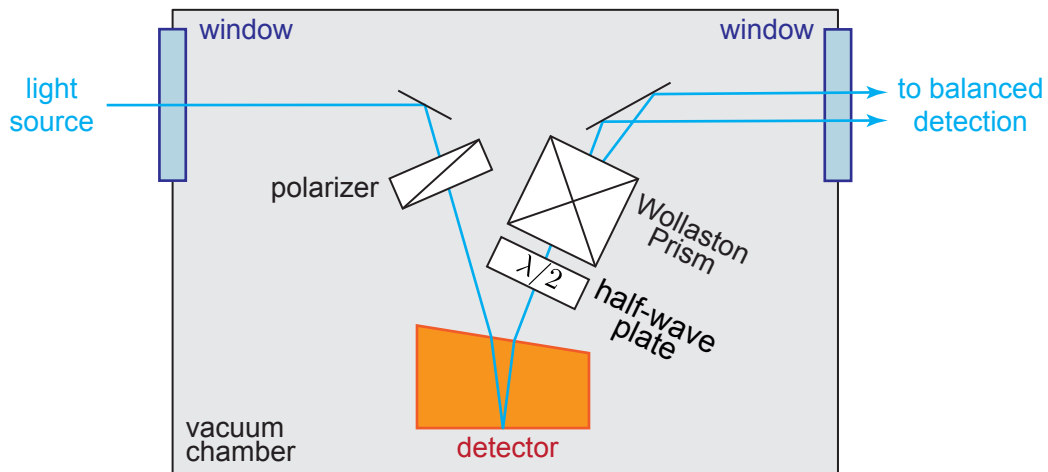


FIGURE 3.6: Experimental configuration to minimize spurious contributions to the Faraday rotation. The polarizer, setting the incoming polarization, and the Wollaston prism, analyzing it, are placed immediately before and after the detection crystal, respectively. The entrance and exit windows are placed away from the detector location, where the magnetic field is negligible.

In pump-probe experiments, there is another significant influence to the polarization state of the beam that is important to take into account. Placing the detection crystal in proximity to the sample often causes the pump beam to interact with the detector as well. The high intensity of the pump beam can strongly influence MOS even if its wavelength falls in the transparency window of the detection crystal. This influence is most evident when the two beams are overlapped both spatially and temporally in the detector. Due to the electro-optic Kerr effect, the pump beam induces a strong transient birefringence, which is a source of ellipticity for the probe beam. The Faraday rotation and birefringence then happen in parallel, significantly complicating the analysis of the polarization state of the outgoing beam.

As discussed in Subsection 3.2.5, these contributions could, in principle, be accounted for by analyzing the full polarization state of the beam. This approach is, however, made unpractical when the spurious contributions of the pump beam are orders of magnitude stronger than those of the pump-induced Faraday rotation. In these cases, it is wiser to remove the effects of the pump altogether by preventing it from entering the detection crystal. If the two beams have a different wavelength, this can be achieved by a frequency filter. Dielectric coatings are, in principle, the ideal solution, but they may induce strain, as mentioned previously. Alternatively, a different material that selectively lets the probe through but reflects the pump can be used to cover the detector. This solution was the one adopted for the dynamical measurements presented in Chapter 4, where the 15 μm wavelength pump was filtered out by a thin slab made of sapphire, whose Reststrahlen band covers completely.

Finally, modulation of the signal at high frequency helps remove all the noise due to slow drifts in the experimental apparatus. When measuring responses due to an applied magnetic field, this can be periodically inverted to subtract all magnetic field-even contributions to the polarization rotation. In pump-probe measurements, the high-frequency differential signal helps filter the noise further. As an example, Appendix C presents the data acquisition scheme employed for this thesis work.

3.2.4 Polarization dependence

The Faraday effect arises as a consequence of a magnetic field applied parallel to the propagation of the electromagnetic wave. For this reason, it possesses axial symmetry with respect to the same propagation direction, and the Faraday rotation θ_F is *independent* of the polarization plane of the incoming light. In contrast, the Pockels effect manifests as a transient birefringence along an axis perpendicular to the light propagation direction. Consequently, the amount of ellipticity it introduces is *dependent* on the initial polarization state of the beam. In a configuration such as the one depicted in Figure 3.5, designed to sample Faraday rotations, the ellipticity can produce a signal that can be mistaken for a polarization rotation. This spurious contribution is of higher order compared to the Faraday rotation (see Equation 3.15), so it is normally negligible. However, if the Verdet constant is negligible or the magnetic field is much smaller than the electric field, the ellipticity contribution can become significant. In these cases, confusion can arise regarding the origin of the measured signal, as outlined in Subsection 3.1.1. This situation is particularly relevant for ultrafast phenomena since the Verdet constant at THz frequencies can be significantly different compared to DC and even completely vanish. In these cases, the Pockels contribution may become dominant.

The ellipticity contribution can be minimized by employing detectors with an exposed surface along crystal cuts that do not present a Pockels effect by symmetry. For this thesis work, the choice was the (100) plane of GaP. Nevertheless, finite angles of incidence, wedges, or alignment errors can contribute to deviating from this ideal configuration.

For this reason, it is good practice in experiments to ensure that the polarization rotation is constant when rotating the incoming polarization. This “sanity check” can be performed by rotating the polarizer responsible for setting the polarization before the detector. In Figure 3.7, two different cases are compared. The first represents the expected dependence if the polarization rotation is due to the Faraday effect. The second shows what would be obtained if the measured signal is instead due to the Pockels effect, i.e., a sampling of the electric field similar to EOS. In this case, the signal inverts sign multiple times during a full rotation of the incoming polarization. The absence of this distinctive feature is a strong indicator in favor of MOS, confirming that the effect indeed originates from a sampling of the magnetic field.

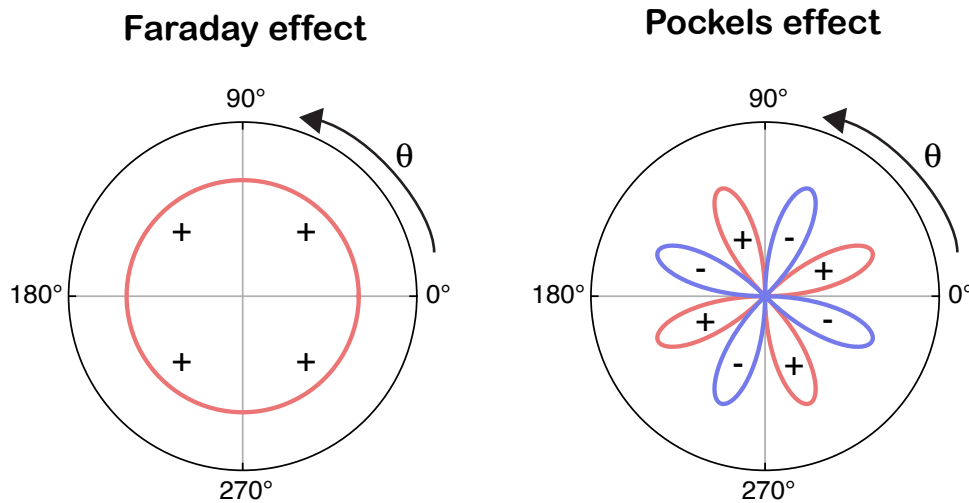


FIGURE 3.7: Comparison of the balancing signal measured in the presence of Faraday or Pockels effect as a function of input polarization θ . Material from [55].

3.2.5 Reconstruction of the full polarization state

As discussed in the previous sections, strain, circular dichroism, pump-induced Kerr and Pockels effects, non-ideal mirrors, and more can all contribute to introducing ellipticity in the probe beam. These non-idealities dramatically complicate the analysis of Faraday rotations, especially when the signal is small. In Section 3.2.3, we introduced a technique aimed at removing all these spurious contributions. In the following, we show how to characterize all those left to extract the Faraday rotation required for MOS.

We start by assuming that, in the detection crystal, the probe beam is both subject to polarization rotation and ellipticity without specifying its origin for the moment. The first is modeled by δ , the phase delay between circularly polarized components, and the latter by η and α , the phase delay between the linear components and principal axis of the birefringence, respectively. Up to now, we introduced a single observable,

shown in Equation 3.13, and therefore, it is not possible to solve the model in a closed form since it has three unknowns.

In order to extend the number of observables, it is possible to alternate the polarity of the applied field and measure both the difference between the two signals and their average. The first quantity, which we call *Normalized Magnetic* (NM), is mostly sensitive to effects that invert with the applied field, such as the Faraday effect, and the second, which we call *Normalized Balancing* (NB), is mostly sensitive to effects that do not invert with the applied field, such as birefringence. By denoting the *Normalized difference* in Equation 3.13 as ND^\pm , where the sign indicates the polarity of the applied field, we have

$$NM = \frac{ND^+ - ND^-}{2} \quad NB = \frac{ND^+ + ND^-}{2} \quad (3.14)$$

Furthermore, in order to increase our sensitivity to ellipticity, we perform the measurement both with and without a quarter-wave plate, placed before the Wollaston prism and with a principal axis along its diagonal (see Subsection 3.2.2). We indicate the respective observables obtained in this ellipticity-sensitive configuration with an additional Q. With these additions, we have four independent observables: NM, NB, NBQ, and NMQ. The latter is often zero since it is sensitive to ellipticity due to magnetic fields. We ignore it to simplify the expressions, but it should be included when circular dichroism is not negligible.

We now express the polarization state and optical elements with Jones formalism (see [69]). The input vector $|IN\rangle$ is circularly polarized, as

$$|IN\rangle = \frac{1}{\sqrt{2}} \begin{bmatrix} 1 \\ -i \end{bmatrix}$$

This beam interacts with the following optical elements (in this order):

- a polarizer setting the incoming polarization linear and at an angle θ_0 with respect to the horizontal

$$POL = \begin{bmatrix} \cos^2 \theta_0 & \cos \theta_0 \sin \theta_0 \\ \cos \theta_0 \sin \theta_0 & \sin^2 \theta_0 \end{bmatrix}$$

- the detector, whose Jones matrix can be obtained by composing that for a circular phase retarder δ with that for a linear phase retarder η with principal axis at α with respect to the horizontal

$$DET = e^{-\frac{i\eta}{2}} \begin{bmatrix} \cos^2 \alpha + e^{i\eta} \sin^2 \alpha & (1 - e^{i\eta})e^{-i\delta} \cos \alpha \sin \alpha \\ (1 - e^{i\eta})e^{i\delta} \cos \alpha \sin \alpha & \sin^2 \alpha + e^{i\eta} \cos^2 \alpha \end{bmatrix}$$

- a half-wave plate with principal axis at $\theta_0/2$ with respect to the horizontal

$$HWP = e^{-\frac{i\pi}{2}} \begin{bmatrix} \cos^2(\theta_0/2) - \sin^2(\theta_0/2) & 2 \cos(\theta_0/2) \sin(\theta_0/2) \\ 2 \cos(\theta_0/2) \sin(\theta_0/2) & \sin^2(\theta_0/2) - \cos^2(\theta_0/2) \end{bmatrix}$$

- optionally, a quarter-wave plate with principal axis at $\pi/4$ with respect to the horizontal

$$QWP = e^{-\frac{i\pi}{4}} \begin{bmatrix} (1+i)/2 & (1-i)/2 \\ (1-i)/2 & (1+i)/2 \end{bmatrix}$$

- a Wollaston prism placed with its diagonal along the horizontal, so that the A and B beams are composed of the projections along $\pm\pi/4$, respectively

$$WOL_A = \frac{1}{2} \begin{bmatrix} 1 & 1 \\ 1 & 1 \end{bmatrix} \quad WOL_B = \frac{1}{2} \begin{bmatrix} 1 & -1 \\ -1 & 1 \end{bmatrix}$$

The Jones vector in the two branches can then be obtained as

$$|A\rangle = WOL_A (\times QWP) \times HWP \times DET \times POL \times |IN\rangle$$

$$|B\rangle = WOL_B (\times QWP) \times HWP \times DET \times POL \times |IN\rangle$$

Finally, the balanced detector BDP measures the intensity of each branch and gives as output their normalized difference

$$\text{BPD}(A, B) = \frac{\langle A|A\rangle - \langle B|B\rangle}{\langle A|A\rangle + \langle B|B\rangle}$$

To model the change in polarity of the magnetic field, we reverse the sign to the circular retardation $\delta \rightarrow -\delta$. The quarter-wave plate is added only for the ellipticity measurements.

By solving this model and computing the relevant quantities defined in 3.14, we obtain the relations linking the three observables to the three unknowns, expressed as a function of the input polarization θ_0 .

$$\text{NM} = +2\delta \frac{\sin(\sqrt{\delta^2 + \eta^2})}{\sqrt{\delta^2 + \eta^2}} \quad (3.15)$$

$$\text{NBQ} = -2\eta \frac{\sin(\sqrt{\delta^2 + \eta^2})}{\sqrt{\delta^2 + \eta^2}} \sin(2(\alpha - \theta_0)) \quad (3.16)$$

$$\text{NB} = -2\eta^2 \frac{\sin^2(\frac{1}{2}\sqrt{\delta^2 + \eta^2})}{\delta^2 + \eta^2} \sin(4(\alpha - \theta_0)) \quad (3.17)$$

A few comments are of order at this stage. Relation 3.15 for NM is a generalization of expression 3.13, valid outside the small angle approximation and in the presence of birefringence. The latter reduces the absolute value of the measured signal, but NM remains independent of the input polarization. Therefore, in experiments, aligning the input polarization along one of the principal axes of the birefringence does not help in reducing its effects, as one may naively expect.³ Relation 3.16 for NBQ is the

³For example, any linear wave plate, despite possessing a significant linear retardation, does not influence the polarization state of a beam whose polarization is aligned along one of its principal axes.

(static) birefringence counterpart of the previous expression. For small angles and circular retardation, it is indeed linear in linear retardation. In this case, by changing the input polarization, maxima and minima are observed periodically depending on the birefringence principal axis. Finally, relation 3.17 for NB is similar to the previous one but is instead proportional to the square of the linear retardation. It is, therefore, much less sensitive to it. Also, its periodicity with input polarization is doubled with respect to NBQ.

As a remark, it is important to remember that the current simplified analysis leading to the relations 3.15-3.17 relied on the assumption that the linear retardation in the detection crystal does not invert with the applied magnetic field, whereas the circular retardation does. This assumption is based on the physical interpretation that the former is due to pump-induced or static birefringence in the detection crystal and the latter to a magnetic field-induced magnetization. This situation is valid for the vast majority of applications. However, it is not in the presence of spontaneous magnetization, such as in ferromagnets, or of an inverting electric field, for example, linked to the induced magnetic field. In this case, further observables must be included to account for both inverting and non-inverting parameters. For instance, it is possible to perform a Fourier analysis of the observables with the incoming polarization angle. Alternatively, it is possible to add electric field measurements with EOS in a separate detector close to the detector for MOS or in the same detector, presenting both Faraday and Pockels effect [70].

Finally, for cases in which $\delta \ll \eta$, it is often needed to include further non-idealities in the analysis. These can include mirror imperfections, finite angles of reflection, non-ideal or misaligned half and quarter-wave plates, finite extinction ratios of the polarizer and Wollaston prism, and not perfectly matched gain in the balanced detector. Most of these imperfections can be characterized before the experiment and included in the model. In particular, polarization dependencies are useful in disentangling different sources of non-idealities manifesting with different periodicity in input polarization. However, the introduction of more complicated optical elements requires the use of numerical methods in order to solve the model, which makes the physical interpretation more abstract.

3.3 Spatial resolution

Contrary to EOS, MOS is almost exclusively employed in the near-field. In this configuration, it is crucial to retain a good spatial resolution in order to resolve small features such as magnetic domains or superconducting vortices. For this task, there are two characteristic lengths to consider: the lateral and the vertical resolutions, which determine the smallest magnetic feature transversal and longitudinal to the propagation of the beam, respectively, that can be resolved.

The geometrical dimensions of the detector determine the vertical resolution. The Faraday angle is indeed the result of an accumulation of the Faraday rotation along

the thickness of the medium. This can be expressed mathematically by writing the Faraday equation in its differential form

$$d\theta_F(z) = V B_z(z) dz \quad (3.18)$$

where we assumed a constant Verdet constant V inside the medium and B_z is the component of the B-field along the propagation of the beam. Then, the total Faraday rotation is obtained as an integral over the thickness L of the detector

$$\theta_F = V \int_0^L B_z(z) dz = V \bar{B}_z L \quad (3.19)$$

where \bar{B}_z is the average of the magnetic field along the detector thickness.

For the reflection configuration (see Subsection 3.2.1), the integral 3.19 has to be performed in both its passes through the detector, and the total rotation is twice what is measured in the transmission configuration. For finite angles of incidence β , two modifications are required. First, the total distance traversed inside the detection crystal has to be modified as $L \rightarrow L / \cos(\beta/n_{det})$, where n_{det} is the relative refractive index from outside to inside the medium, and we computed the internal angle with Snell's law (for small angles for simplicity). Second, the sampled component of the magnetic field is no longer perpendicular to the plane of the detector, but it has an angle instead. These corrections are usually minor and can often be neglected.

The transversal resolution is instead limited by the properties of the beam and the detection scheme. In a confocal configuration, the beam is focused in the detection crystal and then directed towards a photodiode. A magnetic field map can then be obtained by scanning the position of the probe beam relative to the detector⁴. In this case, the lateral resolution is determined by the region to which the beam is confined in the detection crystal. In Figure 3.8, the case for the reflection geometry is presented. For normal incidence, this corresponds to the spot size of the beam D_0 . For a finite angle of incidence β , the lateral area explored by the beam corresponds to $D = D_0 / \cos \beta$.

For visible light, the typical lateral resolution obtained by these means is of order $50 \mu\text{m}$, which can be further increased by improving the quality of the focus and reducing its dimensions.

Alternatively, a magnetic field map can be obtained by wide-field techniques, where, usually, a much larger beam is driven in the detector. The polarization spatial profile of the probe beam is then analyzed using one or multiple CCD cameras positioned in the detector image plane. In this case, the resolution is given by the pixel size times the magnification of the optical system. This approach offers a better resolution, of the order of a few micrometers, and the possibility of capturing a whole

⁴In experiments, it is not convenient to move the probe beam since then the following optics should account for this change. Moving the detection crystal, sample, and pump beam, if present, all by the same amount is usually simpler.

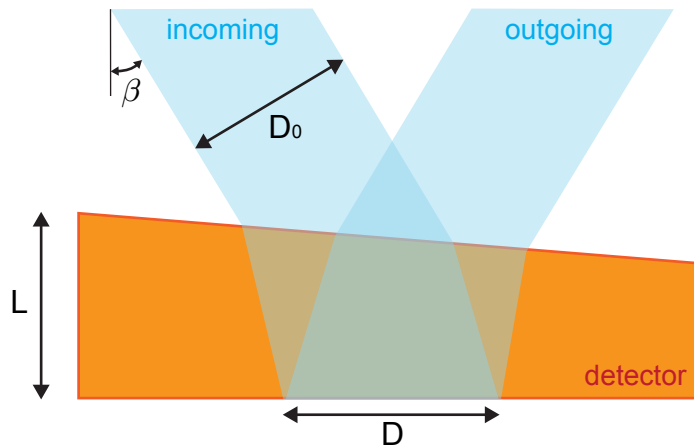


FIGURE 3.8: Spatial resolution in MOS.

map in a single shot. These advantages come at the expense of a much more complicated optical setup and a lower resolution per point. It is, therefore, advisable only when the magnetic field spatial profile is relevant.

3.3.1 Equilibrium measurements of $\text{YBa}_2\text{Cu}_3\text{O}_7$ thin films

As an example of the spatial resolution in MOS, we show measurements of the near-field magnetic response of a $\text{YBa}_2\text{Cu}_3\text{O}_7$ thin film. The sample-detector arrangement is shown in Figure 3.9. The sample has a thickness of 150 nm and is shaped as a half-disk of 400 μm . This shape, obtained with optical lithography, is specifically chosen to mimic that of the light-induced superconducting region studied in Section 4.3.

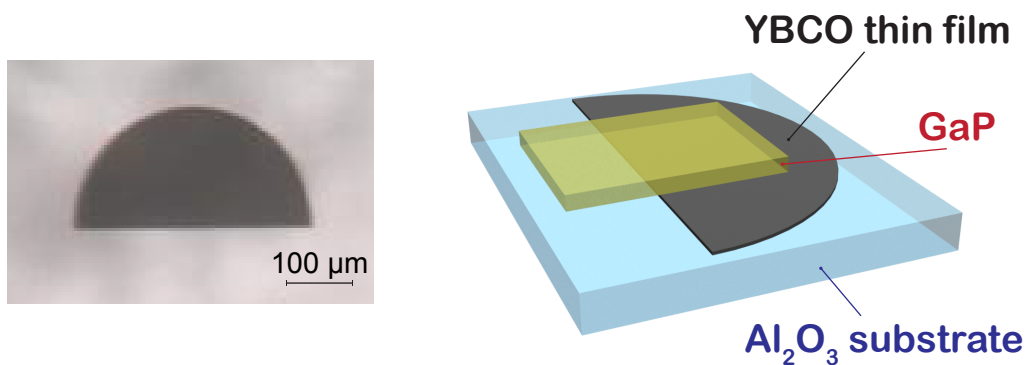


FIGURE 3.9: MOS characterization: sample detector geometry. Material from [55].

The detector is composed of a $\sim 50 \mu\text{m}$ -thick GaP (100) crystal. This diamagnetic detector is not the ideal choice for an equilibrium measurement, where ferrimagnetic detectors would yield much higher sensitivities (see Subsection 3.1.1). It will, however, be useful for its time resolution in the dynamics experiments of Section 3.4.

The detector is placed on top of the sample and in close contact with it. An external magnetic field is applied perpendicular to their planes. Upon superconducting transition, the strong diamagnetic response of the sample induces an enhanced field at its edge and a screened field on its top, as discussed in Section 1.2. These features can be observed by scanning the probe beam over the detector. The accumulated Faraday rotation is then proportional to the magnetic field in a plane immediately above the sample, averaged over the thickness of the detector. This proportionality constant represents the *sensitivity* of a given MOS apparatus.

In principle, by knowing the temperature-dependent Verdet constant of the detector and its thickness, it would be possible to compute the sensitivity directly. In practice, if the value of the applied field is known, for example, by measuring it with a Gauss-meter, it is more accurate to calibrate the detector response by measuring the Faraday rotation without the sample. In this situation, the applied field is homogeneous through the detector, and the measurement output, divided by the applied field, corresponds to the sensitivity. In most cases, this approach offers a much lower uncertainty compared to the error introduced by a detector thickness estimate, especially if it presents a wedge.

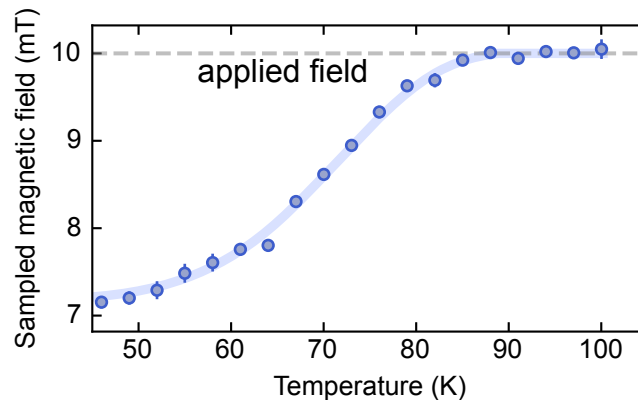


FIGURE 3.10: The sampled magnetic field on the top of the sample shows a superconducting transition at ~ 90 K.

3.3.2 Superconducting transition

In Figure 3.10, the temperature dependence of the magnetic field sampled on top of the $\text{YBa}_2\text{Cu}_3\text{O}_7$ thin film is presented. The external field is 10 mT and is indicated by the dashed line. Upon cooling the sample below $T_c \sim 90$ K, a deviation from the applied field is observed. Due to the specific acquisition scheme, as outlined in Appendix C, the sampled field is sensitive to the ZFC Meissner effect. Even though the magnetic field should go to zero immediately outside the sample, the measured screening field is only reduced to $\sim 70\%$ of the applied one. This apparent discrepancy originates from the finite thickness of the detector, which leads to the averaging of the sampled field (see expression 3.19).

Indeed, if the measurement is repeated with a much thinner (~ 100 nm) ferrimagnetic detector, the measured field does go to zero. This same measurement with a thin diamagnetic detector would be experimentally impractical because of the negligible Faraday rotation it would yield.

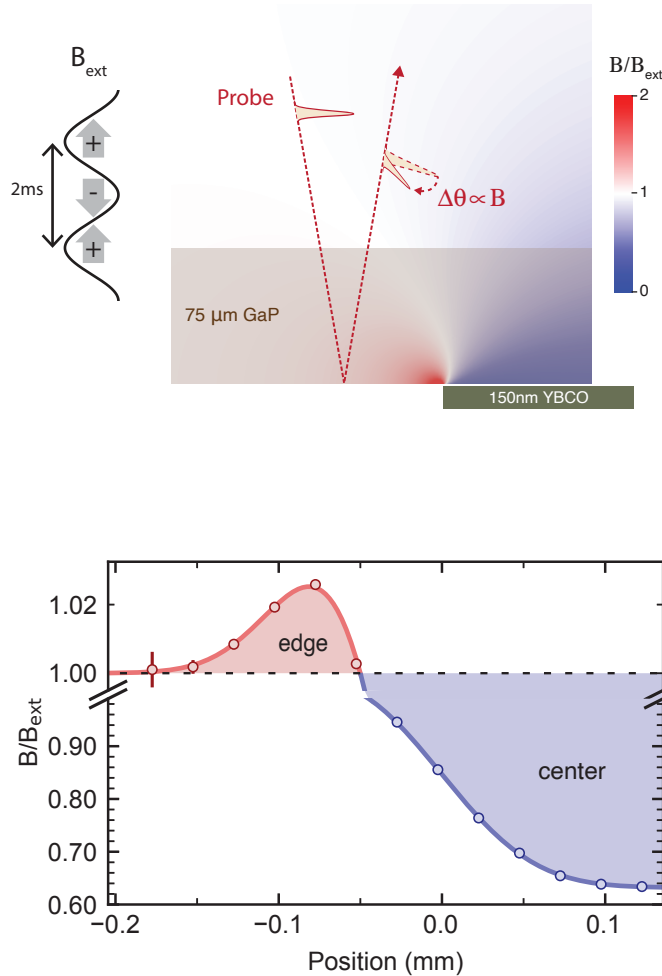


FIGURE 3.11: Spatial dependence of the magnetic field expulsion, presenting an increased field on the edge and a reduced field in the center. Material from [55].

3.3.3 Spatial dependence

After having cooled down the sample, it is possible to reconstruct the magnetic field spatial features in its vicinity by scanning the probe beam across the edge of the sample, as shown in Figure 3.11. In the figure, the color map represents the simulated magnetic field obtained according to the finite elements techniques discussed in Section 1.2. The diagram on the left indicates the alternated magnetic field scheme employed for the measurement, explained in more detail in Appendix C. As the probe beam is scanned over the sample (from left to right in the figure), the sampled magnetic field is seen to increase on its edge and decrease in its center.

Magneto-static simulations (see Appendix D) match the measured curve well with that calculated for a thin film with the same dimensions as the sample and an ideal diamagnetic response $\chi = -1$. In these simulations, the field is averaged vertically over the detector thickness and laterally over the beam spotsize. Both have a typical length of order $\sim 50 \mu\text{m}$, corresponding to the lateral and vertical resolution of the apparatus.

This equilibrium measurement validates the technique and highlights the two *equivalent* signatures of a superconducting diamagnetic response: enhanced field on the edge of the sample and reduced field in its center.

3.4 Time resolution

In this section, we test whether the MOS developed so far also has sufficient temporal resolution to track ultrafast dynamics. We assume initially that the magnetization in the material is realized instantaneously upon change of the local field. This assumption is valid for diamagnetic detectors, whose magnetic dynamics is significantly faster than the probe pulse duration τ (see Subsection 3.1.1). In this limit, the Faraday signal, originating from the material magnetization, can be modeled as proportional to the instantaneous magnetic field experienced by the probe pulse. In the following, we consider the effects of the difference in the velocity of propagation of the probe beam and of the magnetic signal. In analogy to EOS sampling of THz pulses (see for example [34], Section 2.12), since the duration of the probe beam is typically much shorter than the magnetic signal, we employ the group velocity v_g for the former and the phase velocity for the latter V_p , at the respective carrier frequencies.

As shown in Figure 3.12, we assume the magnetic signal to be generated from the sample and directed vertically against the incoming beam. The relative time t is defined as zero when the probe and magnetic pulse meet at the base of the detection crystal. In the reflection configuration considered here, the probe beam meets the magnetic pulse twice in its propagation through the crystal: in the first pass, where the two pulses are counter-propagating with relative velocity $v_{counter} = v_g + V_p$, and in the second pass after being reflected from the back face of the crystal, where the two pulses are co-propagating with relative velocity $v_{co} = v_g - V_p$.

In the counter-propagating interaction, the two pulses walk entirely past each other in a short time. At negative time delays, the sampled signal is, therefore, small and proportional to the integral of the magnetic pulse. This negative offset is often hardly measurable and considered an artifact of the measurement. For delays $t < -L/V_p$, where L is the detector thickness, the two pulses never overlap inside the medium, and the signal is zero.

In the ideal co-propagating interaction, $v_{co} \sim 0$. In this case, the sampled signal is dependent on the relative delay t and equal to the magnetic signal $B(s)$ convolved

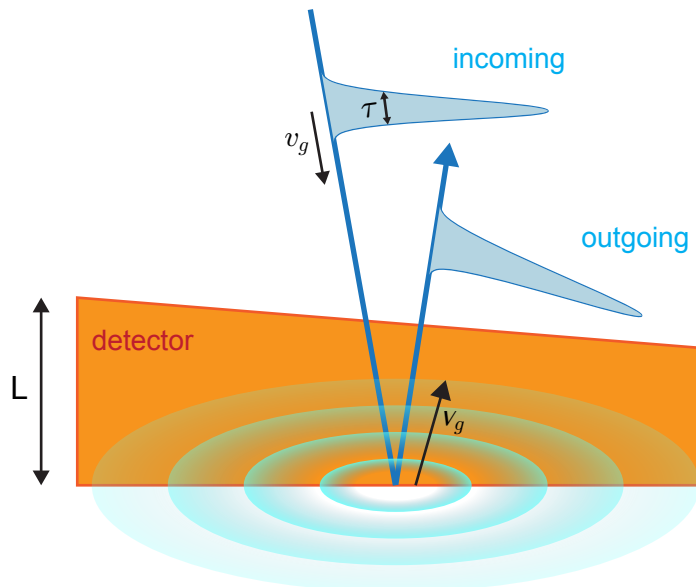


FIGURE 3.12: Temporal resolution in MOS. The magnetic signal is assumed to be generated at the detector base and to propagate away from it with velocity V_p .

with the time profile of the probe pulse $p(s)$, which here we assume as Gaussian

$$\theta_F(t) \propto \int_{det} ds B(s) p(s-t) = \int_{det} ds B(s) e^{(s-t)^2/2\tau^2} \quad (3.20)$$

where the crystal boundaries determine the integration limits. The time resolution is then set by pulse duration τ , which is normally known. In this thesis work, as outlined in Appendix B, the duration of the probe pulse was 35 fs.

If $v_{co} \neq 0$, the probe and magnetic pulses slowly walk off with respect to one another. The longer the crystal, the longer the walk-off experienced. This effect can be accounted for by increasing the width of the convolving Gaussian in Equation 3.20 so that

$$\tau^2 \rightarrow \tau^2 + \left(\frac{L v_{co}}{v_g V_p} \right)^2 \quad (3.21)$$

This correction leads to an effectively broader beam and poorer time resolution. Other factors that may negatively influence the reconstruction of $B(s)$ are the strong dispersion of either the probe or magnetic beam in their propagation. Given the crystal thickness, these are usually negligible for the former but not for the latter. The magnetic signal is indeed often not well represented by a plane wave and can possess significant angular dispersion.

Finally, we hint at how this analysis can be extended when the response time of the detector is relevant. This correction is specifically important when employing ferrimagnetic detectors, whose response time (~ 100 ps) is significantly longer than the typical pulse duration (~ 100 fs). In these situations, the magnetization in the

detector, responsible for the Faraday effect, does not depend only on the instantaneous field inside the material but rather on the field applied in the previous time interval R . This delayed response of the magnetization M upon application of a magnetic field B can be expressed as

$$M(s) = \int_{-\infty}^s ds' \chi(s-s')B(s') \quad (3.22)$$

where $\chi(s-s')$ represents the time-delayed magnetic susceptibility of the medium. In its simplest form, it corresponds to

$$\chi(s-s') = \frac{\chi_0}{R} e^{-\frac{s-s'}{R}} \quad (3.23)$$

where χ_0 represents the DC magnetic susceptibility. Due to the exponential term, the sampled field is averaged over a time-interval R . In the frequency domain, this averaging corresponds to applying a low-pass filter to the magnetic field $B(s)$ below the frequency $1/R$. The detector is, therefore, not sensitive to these higher frequencies.

3.4.1 Dynamical measurements of $\text{YBa}_2\text{Cu}_3\text{O}_7$ thin films

As previously discussed, pulse duration, probe and signal walk-off, detector geometry and response time, can all contribute to worsening the crystal time resolution. Often, they are not all known a priori, and it is therefore important to characterize the time resolution of the detector experimentally. This characterization can be achieved by creating an ultrafast magnetic field change and sampling it with the detector. The faster frequency the detector can follow sets an upper limit on its time resolution. This resolution may be even lower if the bottleneck lies in the generated magnetic field change.

For this thesis work, the time resolution has been characterized employing the same $\text{YBa}_2\text{Cu}_3\text{O}_7$ thin film studied in Subsection 3.3.1, embedded in a 2 mT magnetic field. By irradiating it with an ultraviolet ($\lambda = 400$ nm) pulse below T_c , the superconducting state was promptly disrupted, and the following ultrafast magnetic dynamic was tracked. This dynamics is generated by the sudden transition from the superconducting to the normal state and the concomitant disappearance of the Meissner effect, similar to the thermal transition depicted in Figure 1.4.

As shown on the left side of Figure 3.13, the external field was inverted with every probe pulse to yield a ZFC-like signal (see Appendix C). The pump was also mechanically chopped to obtain a pump-induced magnetic field differential ΔB . In order to avoid spurious contribution from the presence of the pump inside the detection crystal (see Subsection 3.2.3), the pump and probe beams were approaching the sample-detector assembly from opposite directions (see schematics in Figure 3.13). The pump was shaped as a half disk with the same dimensions as the sample by placing a mask in the sample complementary plane of a 4-f system. The remaining radiation was then completely absorbed from the opaque $\text{YBa}_2\text{Cu}_3\text{O}_7$ thin film

and did not reach the detector, traversed only by the probe beam and the generated magnetic signal. Given this favorable configuration, the analysis did not require the advanced techniques of full polarization reconstruction discussed in Subsection 3.2.5.

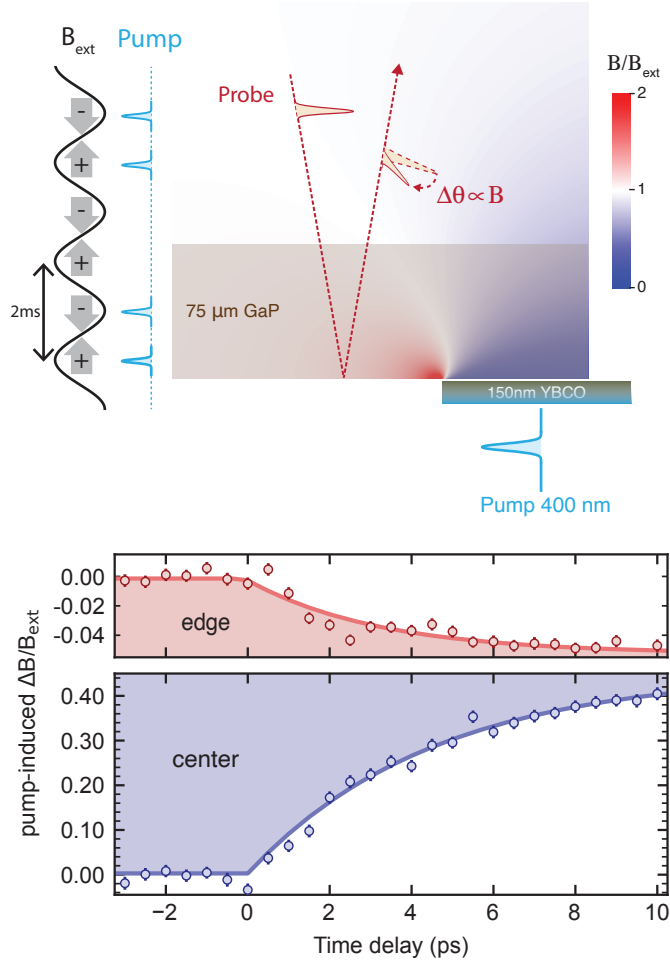


FIGURE 3.13: MOS characterization: temporal dependence dynamics. Material from [55].

The plot in Figure 3.13 represents the time evolution of the sampled magnetic field in two representative positions: on the edge of the sample (red curve) and in its center (blue curve). Upon disrupting superconductivity, we measured a negative magnetic field differential on the edge and a positive one in the center. This change is compatible with a transition from a strong diamagnetic response to a non-magnetic state. The transition, of the order of a few picoseconds, confirms that the GaP detector can track ultrafast dynamics. More careful studies focused on controlling the speed of this transition were able to obtain even faster ramps, with time constants as low as ~ 1.3 ps [22].

In conclusion, we show a complementary analysis of the results just presented. In Figure 3.14, the plot of the magnetic field differential between negative delays and 10 ps is plotted as a function of position across the edge of the sample, defined at

0 mm on the horizontal axis. The finite thickness of the detector, which averages the magnetic field above the sample, causes the crossover from a positive to a negative differential to happen slightly away from the edge of the thin film. It is also evident that the positive differential signal extends away from the edge for only $\sim 200 \mu\text{m}$. This will be relevant for the edge measurements presented in the next section, where, due to a different pump configuration, exclusively edge measurements were performed.

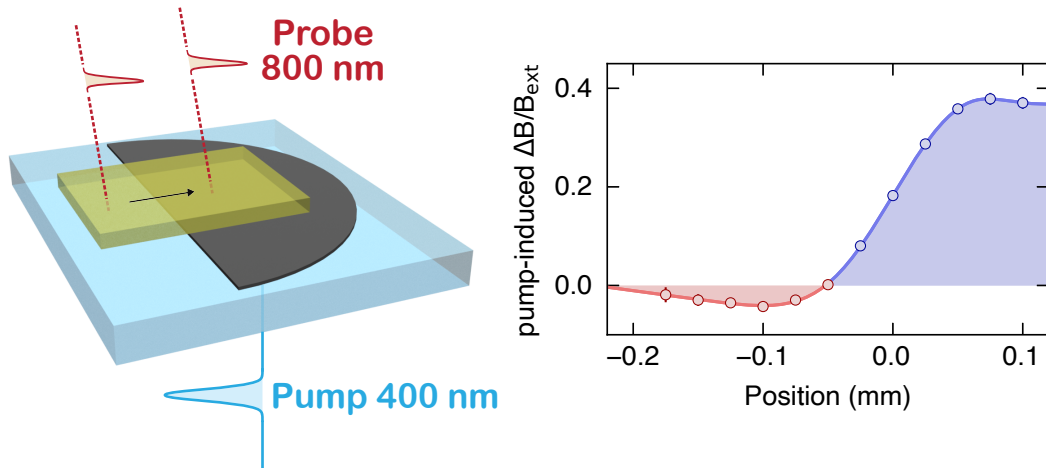


FIGURE 3.14: MOS characterization: spatial dependence dynamics. Material from [55].

Chapter 4

Magnetic properties of equilibrium and driven $\text{YBa}_2\text{Cu}_3\text{O}_{6.48}$

This chapter presents the main experimental results of this thesis work. It applies the techniques of MOS developed in Chapter 3 to study the light-induced superconducting state of $\text{YBa}_2\text{Cu}_3\text{O}_{6.48}$ presented in Chapter 2. Before this work, its transient properties had been investigated exclusively with THz reflectivity and SHG, and nothing was known related to its magnetic dynamics.

4.1 Sample and detector arrangement

The sample is a single crystal of approximate dimensions $2\text{ mm} \times 2\text{ mm}$ in the ab-plane and 0.5 mm along the c-axis. The details related to the sample synthesis and equilibrium characterization are outlined in Appendix A.

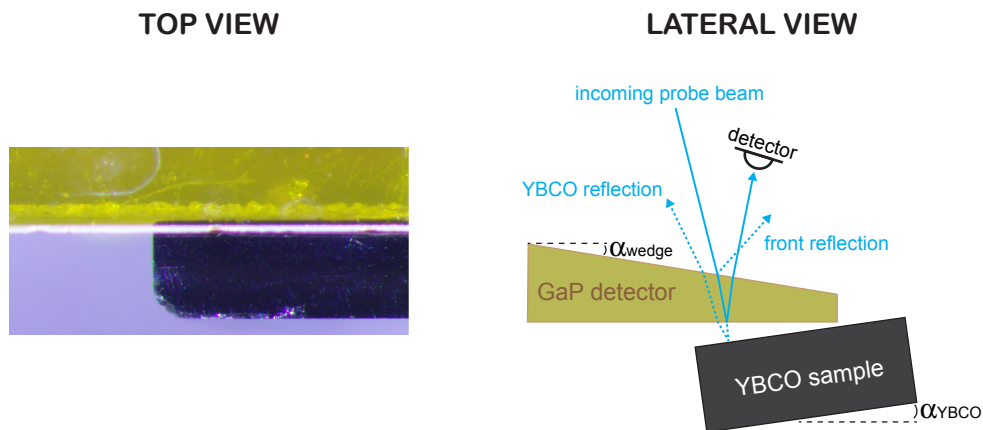


FIGURE 4.1: Top view (left) — micrograph of the sample (black) and detector (orange) arrangement. Lateral view (right) — wedge angle $\alpha_{\text{wedge}} \sim 1.5^\circ$ and YBCO angle $\alpha_{\text{YBCO}} \sim 1^\circ$ introduced to spatially filter undesired reflections. Material from [55].

In view of the dynamical experiments presented later, the sample is mounted retaining optical access to its c-axis, aligned along the incoming pump beam polarization (vertical direction in Figure 4.1, top view). Unlike the experiments on thin films presented in Chapter 3, the arrangement with the pump and probe beams approaching

from different sides was not possible. The photo-excited superconducting region has a thickness proportional to the pump penetration depth ($\sim 1 \mu\text{m}$), and its diamagnetic response decays over distances much shorter than the sample thickness ($\sim 2 \text{mm}$). Therefore, the signal would not be detectable on the other side of the sample. Standard synthesis techniques produce thin films with the c -axis normal to the plane, a geometry not suitable for optically driving the apical-oxygen phonon mode.

The external magnetic field is applied along the beam propagation direction, along the ab -planes of the crystal. A $70 \mu\text{m}$ -thick GaP (100) detector is placed in close proximity on top of the sample. As shown in Figure 4.1, lateral view, a small angle $\alpha_{\text{YBCO}} \sim 1^\circ$ between the detector and sample planes is introduced to filter out probe beam reflections coming from the sample surface.

4.2 Equilibrium measurements

In this Section, we present a series of measurements characterizing the equilibrium state of $\text{YBa}_2\text{Cu}_3\text{O}_{6.48}$. The left plot in Figure 4.2 shows a temperature dependence of the magnetic field sampled on top of the sample, with an external field of 1mT . At $T_c \sim 55 \text{K}$, a progressive field screening is observed, indicative of the onset of the diamagnetic response associated with the superconducting state. The field screening saturates to about 50% of the applied field due to the finite thickness of the detector.

Magneto-static simulations can link the sampled magnetic field to the intrinsic properties of the superconductor. A uniform magnetic susceptibility χ is assigned to a volume of the same dimensions of the sample. Then, Maxwell equations are numerically solved in the surrounding area with the boundary condition that the field further away from the sample corresponds to the value of the applied field. Finally, the field is integrated over the detector thickness to account for its averaging effects (see Equation 3.19). By varying χ between ~ 0 (weak metallic response) and ~ -1 (ideal diamagnetic response), magnetic field maps in the volume surrounding the sample are computed.

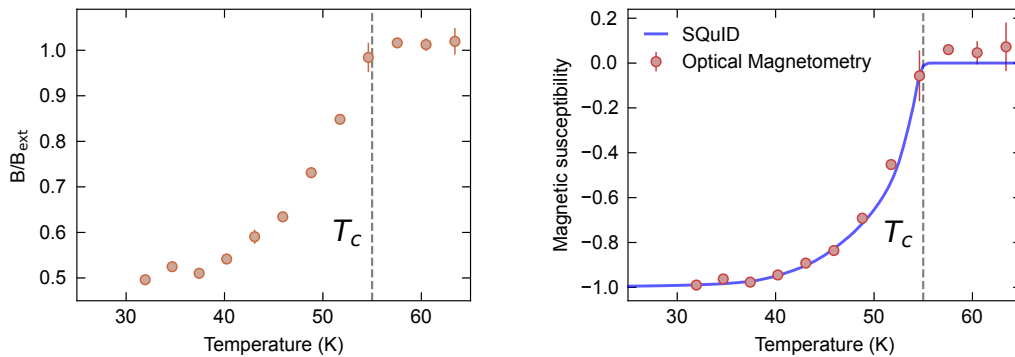


FIGURE 4.2: Temperature dependence of diamagnetic response at equilibrium. Material from [55].

As a comparison, the plot on the right of Figure 4.2 compares the susceptibility extracted from MOS measurements (red circles) with that obtained from a conventional SQUID magnetometer (blue line) performed on the same sample. The two agree almost perfectly. Appendix D presents in more detail the magneto-static simulations and the related analysis to compute the conversion function.

4.2.1 Spatial dependence

As presented in Subsection 3.3.3, the onset of the superconducting diamagnetic response entails an enhancement of the magnetic field on the edge of the sample and a reduction on the center. The two are complementary observables since the total magnetic flux is conserved. Both features can be resolved by scanning the probe beam across the edge of the sample, as shown in Figure 4.3, at a fixed temperature $T = 25 \text{ K} < T_c$.

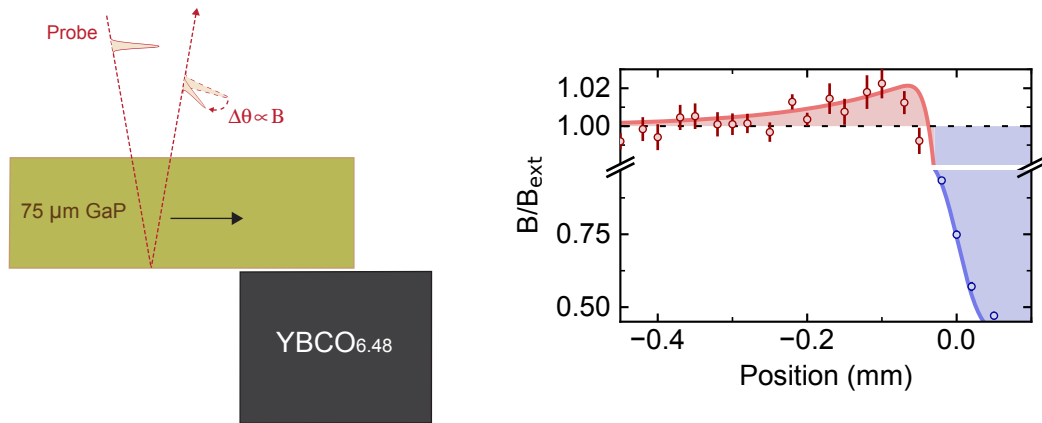


FIGURE 4.3: Equilibrium magnetic field enhancement on the edge of the sample (red) and reduction (blue) on the center. The solid line is a guide to the eye. Material from [55].

4.2.2 Applied magnetic field dependence

The dependence of the magnetic field measured on top of the sample as a function of the externally applied field is shown in Figure 4.4. The differential ΔB is defined as the magnetic field measured with the sample, referenced to the field measured without. In practice, the latter case is achieved by shifting the probe beam in a position of the detector far away from the sample where its contributions are negligible (see sketch in the figure). For zero applied field, the superconductor does not have a magnetization, and the differential is zero. Upon increasing the field, there is a linear increase in screening, corresponding to the Meissner state of the superconductor. Upon reaching the first critical field $B_{c1} \sim 2 \text{ mT}$ ¹, the superconductor enters its vortex state,

¹The effects of internal fields can be estimated by computing the demagnetizing factor of the sample [71]. The value of $N \sim 0.17$, according to Equation 1.5, corresponds to a correction factor of ~ 1.2 in the critical field estimate.

and the expelled field is reduced. This nonlinear behavior is typical of equilibrium superconductors.

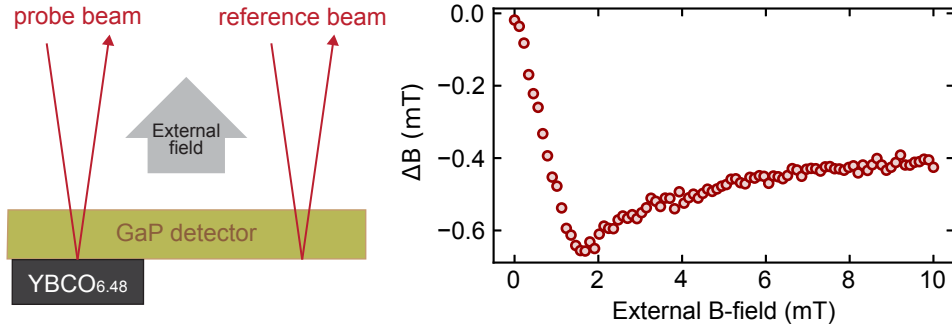


FIGURE 4.4: Magnetic field dependence at equilibrium.

4.3 Driven magnetic field expulsion

In this Section, we present measurements of the transient properties in the photo-excited state of $\text{YBa}_2\text{Cu}_3\text{O}_{6.48}$. The dynamics is driven by a 1 ps-long, 15 μm MIR pulse, polarized along the c-axis of the sample and resonant with the apical-oxygen phonon modes responsible for the transient superconducting-like optical features observed with THz spectroscopy. The base temperature is $T = 100 \text{ K} > T_C$, and we expect to induce a diamagnetic response upon photo-exciting the system. In Appendix B, the optical setup developed to generate the MIR radiation and the probe beam are presented in detail.

Opposite to the measurements on thin films presented in Subsection 3.4.1, the sample is initially in its normal state, and we expect to induce a superconducting transition. We track the magnetic response by sampling the field on the edge of the photo-excited region, as shown in Figure 4.5. The GaP detector is placed immediately adjacent to the focus of the pump beam. The radiation of the MIR pump is prevented from interacting with the detection crystal by two 30 μm -thick z-cut Al_2O_3 , highly reflective at 15 μm , placed above the detector and on its side. Ellipticity measurements performed by adding a quarter-wave plate before the Wollaston analyzer (see Subsection 3.2.2), highly sensitive to the presence of the pump, confirmed its total exclusion from the interior of the detector. Consequently, these measurements did not require the advanced analysis techniques of full polarization reconstruction presented in Subsection 3.2.5.

Importantly, the Al_2O_3 mask creates a sharp edge in the photo-excited region, a prerequisite to maximizing the magnetic field changes in its vicinity. The 375 μm -wide spotsize of the MIR pump is shaped into a half-disk with the same dimensions as the thin film characterized in Chapter 3. The applied magnetic field is cycled, and the pump pulses reach the sample at half the repetition rate as the probe, yielding double differential pump-probe measurements. Time zero is defined as the instant in

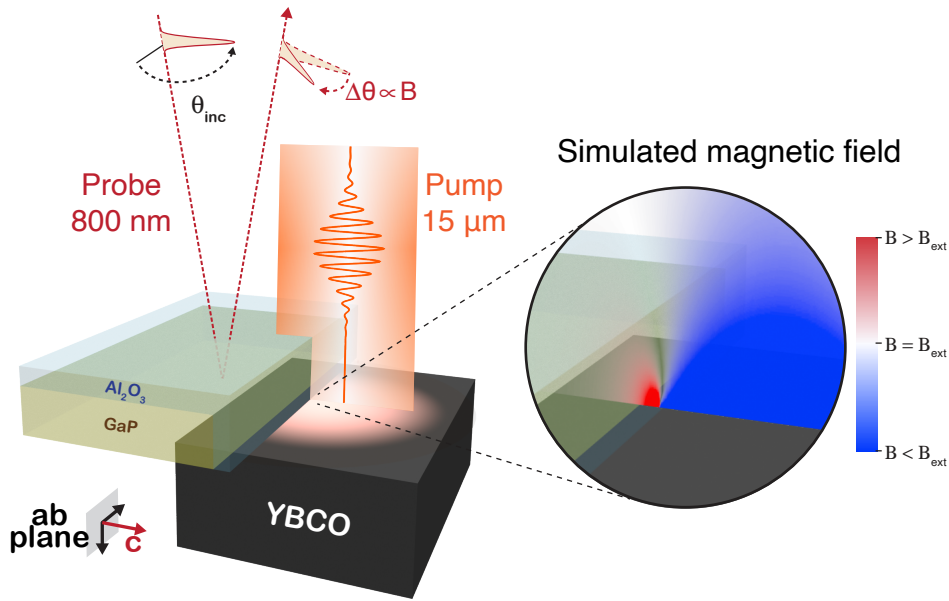


FIGURE 4.5: Geometry of the experiment. The color scale in the magnified area indicates the expected magnetic field change upon superconducting transition. Material from [55].

which the probe and pump beam reach the second interface of the detector and the sample surface, respectively. Their relative delay and position are carefully optimized and monitored in situ by maximizing the electro-optic Kerr effect in a portion of the detector not covered by the Al_2O_3 mask. As a reference, the top plot in Figure 4.6 shows the time profile of the pump pulse.

The lower plot shows the transient magnetic field, sampled approximately $50\ \mu\text{m}$ away from the edge of the photo-excited region, for an external field of 10 mT and two base temperatures: 100 K (red) and 300 K (yellow). Upon driving the system, a prompt increase of the magnetic field is observed, peaking at around $10\ \mu\text{T}$ ($B_{\text{ext}}/1000$) at 100 K and $3\ \mu\text{T}$ ($B_{\text{ext}}/3000$) at 300 K. The sign of the magnetic field change is opposite compared to the disruption of superconductivity presented in Subsection 3.4.1, indicating the onset of a diamagnetic response, compatible with a transient *induction* of superconductivity.

A prompt diamagnetic response is observed upon driving the system, increasing as long as the pump field is present. Once the drive is over, the system decays to the initial state over $\sim 1\ \text{ps}$, a time comparable with the lifetime of the driven phonons [36]. This observation indicates that the photo-excited state does not possess intrinsic rigidity, in agreement with THz measurements.

The measured magnetic field expulsion can be converted into a quasi-static susceptibility by simulating the response originating from a sample of dimensions of the photo-excited volume with a uniform χ (see Appendix D). In view of the dynamical nature of the response discussed in Section 4.4, this assumption is not entirely justified, although it provides a good estimate for the size of the effect. The amount of

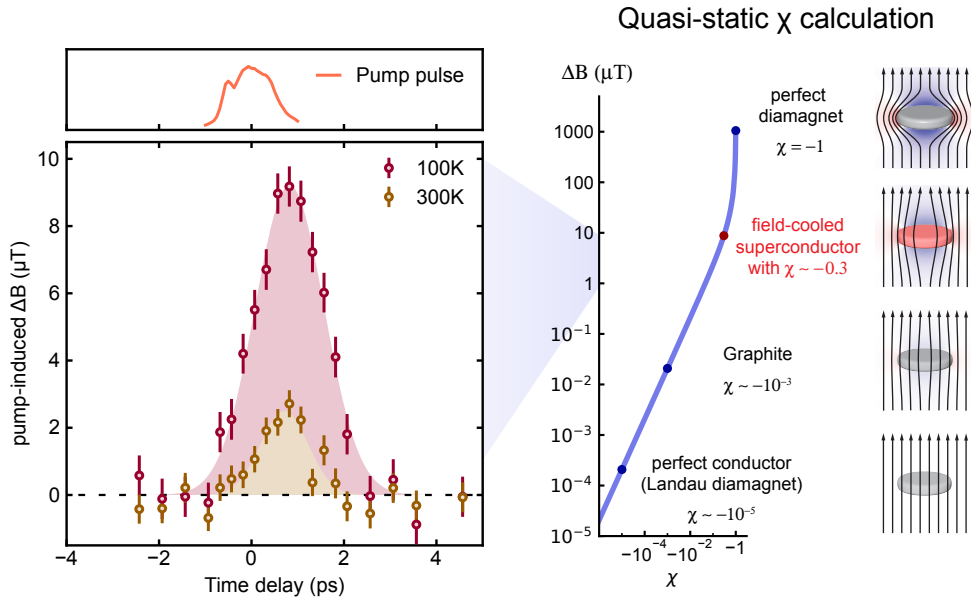


FIGURE 4.6: Pump probe time dependence. Material from [55].

the induced magnetic susceptibility at 100 K is shown in red on the right of Figure 4.6 and corresponds to approximately -0.3 . As a comparison, this value is orders of magnitude higher than what is realized in Landau diamagnets. Remarkably, it is at least two orders of magnitudes stronger than that observed in the planes of graphite, the strongest known metallic diamagnet. Rather, the colossal photo-induced diamagnetic response is reproduced at equilibrium only by type-II superconductors.

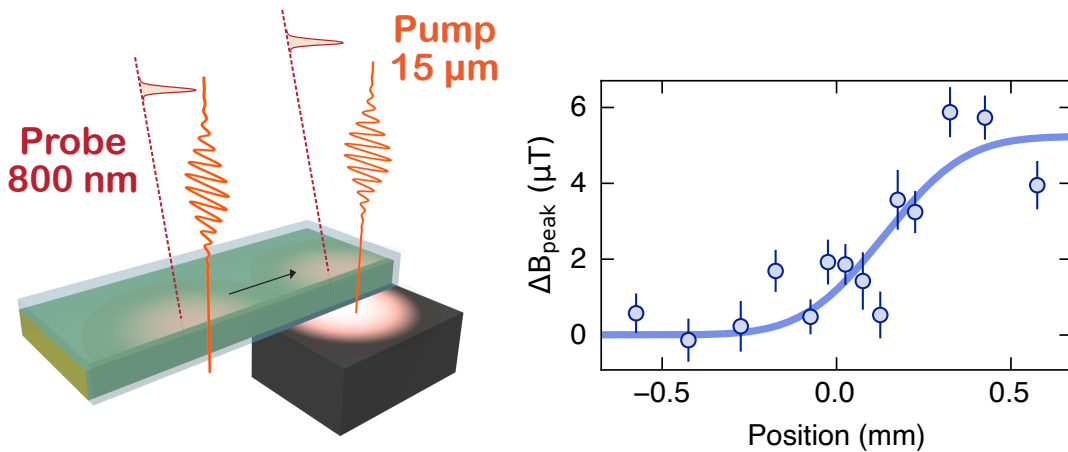


FIGURE 4.7: Spatial dependence away from sample. Material from [55].

4.3.1 Spatial dependence

As a first control experiment, in Figure 4.7 we show how the effect varies as the field is sampled in a position of the detector where there is no sample. The base temperature is 100 K, and the applied field is 10 mT. In this dependence, the pump beam is shifted accordingly to follow the probe beam. The edge of the sample is located at 0 mm on the horizontal axis.

As shown in the plot, the effect gradually disappears as the magnetic field is measured away from the sample. Since the pump position with respect to the probe beam is unchanged, this observation confirms that the effect originates from the sample and not from a spurious contribution of the pump beam inside the detection crystal.

4.3.2 Probe pulse polarization dependence

As a second control experiment, we study the dependence of the effect on the incoming probe pulse polarization. This study is important in ruling out EOS as the origin of the measured signal. As discussed in Subsection 3.2.4, the Faraday effect is independent of incoming polarization, whereas the Pockels effect strongly depends on it. The latter should be zero due to the crystal cut, but the finite angle of incidence or minor misalignments may prevent its complete cancellation.

In Figure 4.8, the differential magnetic field at the peak of the pump-probe ΔB_{peak} is plotted as a function of incoming polarization. The base temperature is 100 K, and the applied field is 10 mT. The flat dependence confirms the Faraday effect as the origin of the measured signal.

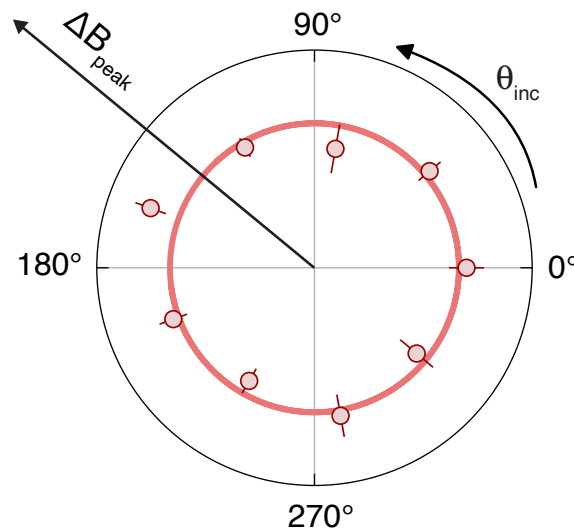


FIGURE 4.8: Probe pulse polarization dependence. Material from [55].

4.3.3 Applied magnetic field dependence

In order to gain insight into the origin of the effect, we study its dependence on the value of the applied magnetic field. In Figure 4.9, the differential magnetic field at the peak of the pump-probe ΔB_{peak} is plotted as a function of the externally applied magnetic field. The base temperature is 100 K. The observed dependence does not show signs of deviation from linearity for fields as high as those achievable with the Helmholtz coil employed for this experiment ($B_{\text{max}} = 12.5$ mT).

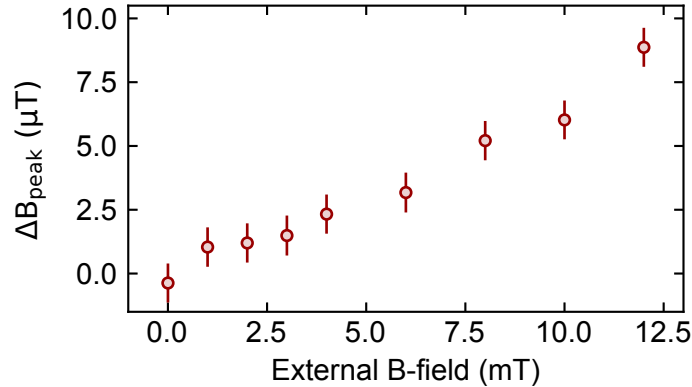


FIGURE 4.9: External magnetic field dependence. Material from [55].

The absence of the effect with no applied magnetic field further rules out alternative mechanisms as the origin of the measured signal, such as the sampling of the magnetic field carried by the MIR pump pulse. We note that the lack of nonlinear behavior is in contrast with the equilibrium measurements presented in Figure 4.4. Therefore, this deviation could imply that the effective critical field of the photo-excited state has been pushed to higher magnetic field values, similarly to the increase in effective critical temperature. As a comparison, the critical field of optimally doped $\text{YBa}_2\text{Cu}_3\text{O}_7$ is of order ~ 20 mT [72].

4.3.4 Fluence dependence

Figure 4.10 shows the dependence of the effect with the fluence of the driving field, for 1 ps-long pulse centered at $15 \mu\text{m}$. The base temperature was 100 K, and the applied field 10 mT.

Remarkably, the scaling is *not* proportional to the fluence but rather sublinear. The data in all other dependencies were acquired at a fluence of $\sim 14 \text{ mJ cm}^{-2}$. Considering a pulse duration of ~ 1 ps, the peak electric field was approximately $\sim 2.5 \text{ MV cm}^{-1}$. These correspond to the optimal conditions for light-induced superconductivity in $\text{YBa}_2\text{Cu}_3\text{O}_{6.48}$ obtained from THz studies [17].

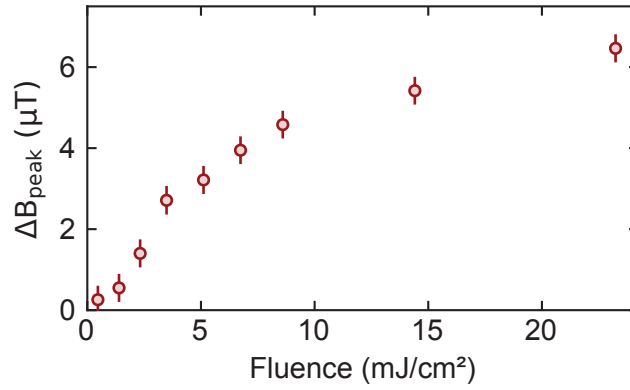


FIGURE 4.10: Fluence dependence. Material from [55].

4.3.5 Temperature dependence

Finally, we analyze how the effect scales with temperature. Pump-probe traces in the same conditions as those presented in Figure 4.6 were repeated for a range of base temperatures from 100 K to 300 K, in steps of 50 K. The results are presented in Figure 4.11. The traces at 100 K and 300 K have been averaged for significantly longer and, consequently, have lower uncertainties. By comparing the different curves, no significant difference in the dynamics is observed, except for their amplitude.

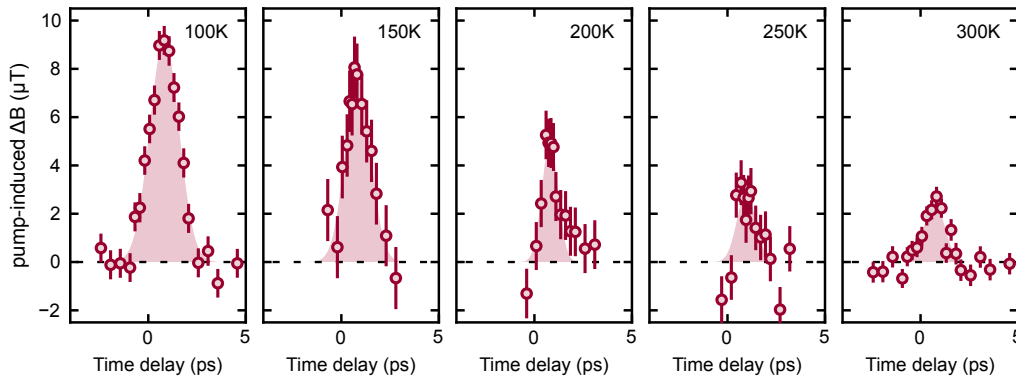


FIGURE 4.11: Time traces at different temperatures. Material from [55].

Figure 4.12 shows the extracted amplitudes (red circles), based on Gaussian fits of the traces presented in Figure 4.11, as a function of temperature. The effect is seen to monotonically decrease with increasing temperature. The temperature dependence of the magnetic field expulsion is compared with that of the superfluid density obtained from THz reflectivity [16] (blue dashed line). The agreement of the two suggests a common physical origin for the two different observables.

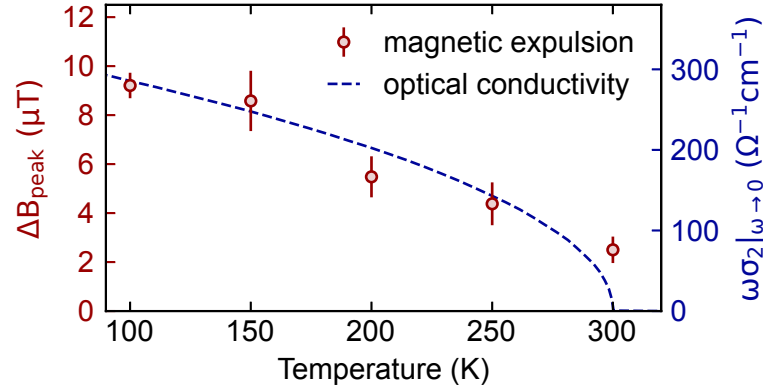


FIGURE 4.12: Temperature dependence of the differential magnetic field change at the peak of the pump-probe response (red circles), compared with the same dependence of the superfluid density extracted from THz reflectivity measurement [16] (dashed line). Material from [55].

4.4 Magnetic field propagation

In this section, we consider the dynamical nature of the ultrafast diamagnetic response. In analogy to a loop antenna, where a time-varying current in a circular path emits a magnetic wave, we expect the ultrafast change in magnetization, associated with the onset of superconducting shielding currents, to act as a source for a propagating wave.

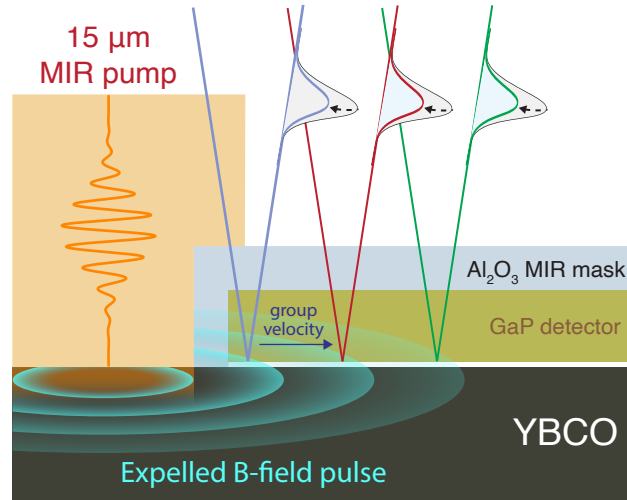


FIGURE 4.13: Schematics of magnetic field pulse propagation. Material from [55].

The origin of the wave is the irradiated area on the side of the detector. As shown in Figure 4.13, by shifting the probe beam sequentially further and further away from the edge, it is possible to sample the emitted wave at later and later delays. The time traces of the magnetic field differential for three representative distances from

the edge of the photo-excited region, at $50\ \mu\text{m}$, $110\ \mu\text{m}$, and $170\ \mu\text{m}$, are shown in the left plot of Figure 4.14. For further distances, the amplitude of the effect is seen to decrease (middle plot), and the arrival time of the $\sim 1\ \text{ps}$ -long pulse to be delayed (right plot).

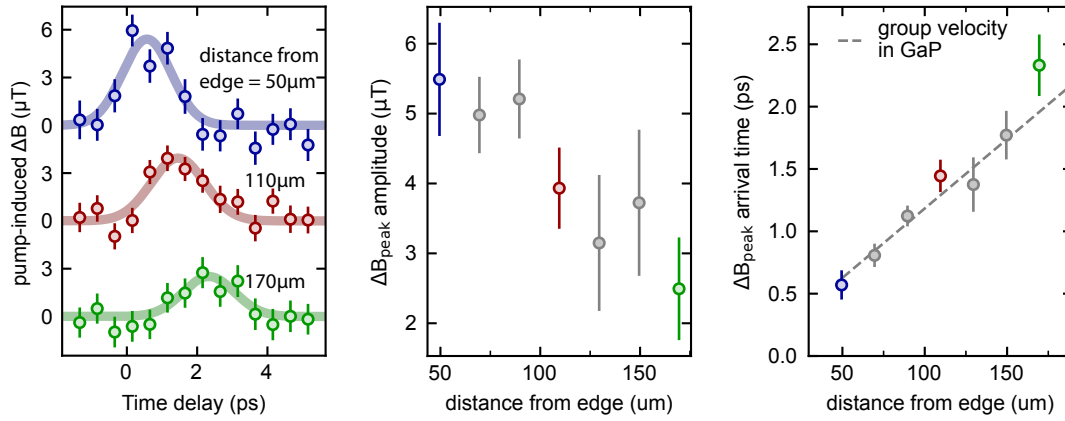


FIGURE 4.14: Magnetic field pulse propagation. Material from [55].

These observations are consistent with a propagating magnetic wave. In particular, its speed of propagation matches well with the group velocity of a 1 THz wave propagating in GaP [63].

Conclusions

Interpretation

The magnetic field expulsion sampled on the edge of the photo-excited region in driven $\text{YBa}_2\text{Cu}_3\text{O}_{6.48}$ is compatible with the dynamical onset of a superconducting-like diamagnetic response. Spatial and polarization dependencies exclude most alternative scenarios as the origin of the detected signal, such as accidental EOS in GaP (100) or MOS of the magnetic field carried by the pump. Different pump fluences result in a sublinear dependence of the effect with pump intensity, ruling out the electro-optic Kerr effect as the origin of the signal (which should be linear with pump intensity) and possibly suggesting a saturation regime of the effect. Interestingly, no deviations from linearity in the magnetic field dependence indicate that the critical field has been pushed to higher values (similarly to the increase in critical temperature) or that its notion must be modified when considering dynamical states. Finally, the temperature dependence, qualitatively similar to that obtained in THz measurements, suggests a common physical origin for these two different observables.

Quasi-static simulation associated a magnetic susceptibility $\chi \sim -0.3$ to the peak of the response in the driven state. This interpretation builds on the parallelism between equilibrium and photo-excited properties, in the same way that the $\sim 1/\omega$ divergence of σ_2 in THz measurements is interpreted as a transient superfluid density. This approach can be extended to other superconducting signatures in cuprates, such as Josephson oscillations or nonlinear transport. The validity of this quasi-static picture relies on the assumption that the superconducting state manifests over timescales much shorter than the duration of the drive. This situation can be realized by driving specific modes to high amplitudes, where rectification processes can induce quasi-static displacements of nonlinearly coupled modes, inducing more favorable conditions for the superconducting pairing. The lattice displacement via nonlinear phononics presented in Subsection 2.1.2 is one of the possible routes to realize this scenario.

An alternative, not contrasting, interpretation explains these observations by a mechanism where pre-existing diamagnetic currents, present throughout the pseudogap phase, are amplified or stabilized by the drive. This scenario is closely related to the amplifications of Josephson plasma polaritons presented in Subsection 2.4.4 and reminiscent of a Floquet-like dynamical superconductivity. An extension of the theoretical framework presented in [59], accounting for the magnetic response of the system, is currently being discussed.

Future prospects

The results presented in this thesis work required a considerable amount of experimental work, particularly for the development of the Ultrafast Magnetometry technique.

One of the most challenging aspects has been the integration of an intense MIR beam close to the detection crystal, which would have introduced significant spurious contributions if not appropriately handled. In this particular case, key to this success has been the implementation of Al_2O_3 crystals as frequency filters. Their operational bandwidth is, however, limited to their Reststrahlen band ($\sim 17 - 24$ THz), significantly hindering the applicability of this technique to excitations at different energies.

On the other hand, the experimental configuration presented in Chapter 3, where the pump and probe are approaching the sample-detector assembly from different directions, is not constrained to a particular excitation frequency range provided that the sample absorbs the pump beam radiation. However, thin samples are required to detect sizeable changes in the surrounding magnetic field. This approach could not be employed in the studies of $\text{YBa}_2\text{Cu}_3\text{O}_{6.5}$ single crystals presented in Chapter 4 because of limitations linked to the growing process.

The development of Focused Ion Beam (FIB) machining technologies [73] provides the technical capabilities to produce thin lamellas of $\text{YBa}_2\text{Cu}_3\text{O}_{7-\delta}$ with the *c*-axis oriented in the plane, exposed to the MIR radiation. A possible experimental setup employing thin $\text{YBa}_2\text{Cu}_3\text{O}_{6.48}$ lamellas is shown in Figure 4.15. The sample thickness ($\sim 5 \mu\text{m}$) is selected to be a few times larger than the pump penetration depth ($\sim 1 \mu\text{m}$). In this way, most of the sample volume is excited, and a negligible amount of the pump light traverses it. The remaining radiation is absorbed or reflected by an Al_2O_3 mask. In this geometry, the choice of the mask material is easier because the probe beam does not traverse it. Therefore, different pump frequencies are straightforwardly implementable. Furthermore, the probe beam is not constrained to measure edge effects but can also access the field reduction present in the center of the sample. This more flexible and controlled experimental configuration offers the potential for accurate studies of the photo-excited state, which can be used as a benchmark for quantitative theories of light-induced superconductivity.

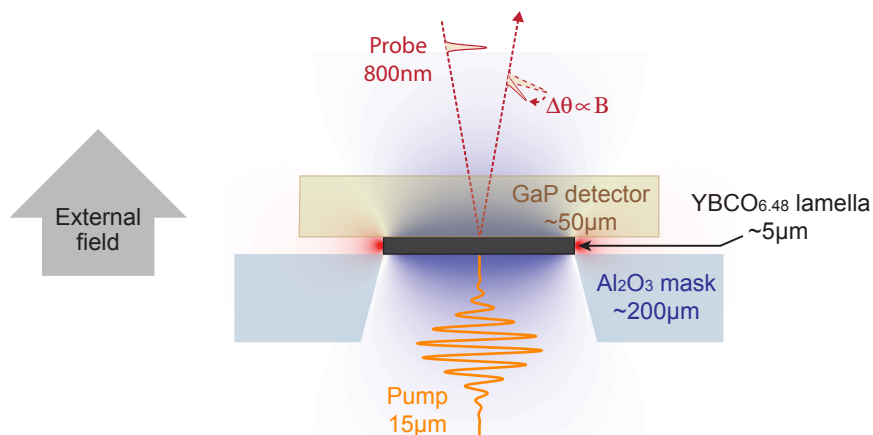


FIGURE 4.15: Experimental configuration for thin $\text{YBa}_2\text{Cu}_3\text{O}_{6.48}$ lamella measurements.

Appendix A

Sample growth and characterization¹

The optimally doped $\text{YBa}_2\text{Cu}_3\text{O}_7$ thin films were obtained through a commercial supplier (Ceraco GmbH) and grown on R-cut Al_2O_3 substrates. The films had a thickness of approximately 150 nm, a sharp superconducting transition temperature at around 85 K and a critical current density greater than 2 MA cm^{-2} . The $\text{YBa}_2\text{Cu}_3\text{O}_{6.48}$ single crystals had typical dimensions of approximately $2 \text{ mm} \times 2 \text{ mm} \times 0.5 \text{ mm}$, where the thin dimension corresponds to the c -axis, and were grown in yttrium-stabilized zirconium crucibles. The hole doping of the Cu-O_2 planes was adjusted by controlling the oxygen content of the Cu-O chain layer by annealing in flowing O_2 and subsequent rapid quenching. A superconducting transition at $T_c = 55 \text{ K}$ was determined by SQUID DC magnetization measurements, as shown in Figure A.1.

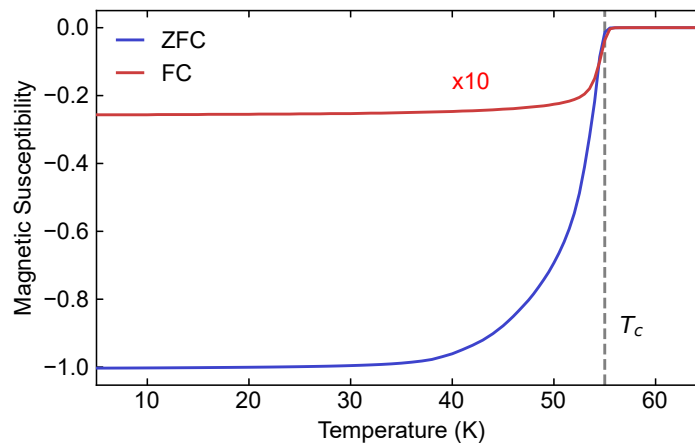


FIGURE A.1: Temperature dependent DC magnetization measurements (ZFC: zero field cooled, FC: field cooled) highlighting the superconducting transition in $\text{YBa}_2\text{Cu}_3\text{O}_{6.48}$. The measurements were performed in a 1 mT applied field perpendicular to the crystal c -axis

¹Part of this and the following Appendices, given the highly technical nature of the content, have been taken verbatim or adapted from the Supplementary Information and Methods of the related publication [55].

Appendix B

Light sources and signal acquisition

The equilibrium spatial scans and superconductivity disruption measurements shown in Chapter 3 were performed using the experimental setup sketched in Figure B.1. Ultrashort (100 fs) 800 nm laser pulses were produced starting from a commercial Ti:Al₂O₃ oscillator-amplifier chain that generated pulses with energies up to 2 mJ at a repetition rate of 900 Hz. These pulses were split using a beamsplitter into two branches. After attenuation, the lowest intensity branch was used to probe polarization rotation in the GaP (100) magneto-optic detector. In order to minimize the polarization noise of the source, the polarization of the beam was set using a nanoparticle high-extinction ratio linear polarizer.

As non-normal incidence reflections introduce a phase delay between s and p polarizations, incidence angle fluctuations can give rise to polarization noise. In order to minimize this noise source, only reflections close to normal incidence were used in the setup, and a commercial system using active feedback was used to stabilize the laser beam pointing. After traversing and being reflected from the second surface of the Faraday detector, the polarization state of light was analyzed using a half-waveplate, Wollaston prism, and balanced photodiode setup that allowed us to quantify the Faraday effect in the magneto-optic detection crystal. The higher intensity branch was mechanically chopped at a quarter of the repetition rate (225 Hz) and frequency-doubled using Second Harmonic Generation (SHG) in a β -BaB₂O₄ (BBO) crystal to obtain 400 nm pulses that were used to photo-excite the YBa₂Cu₃O₇ thin film samples. A mask, illuminated by these ultraviolet pulses, was imaged onto the back surface of the sample to create a half-gaussian beam with an edge that matched the long edge of the half-disk-shaped YBa₂Cu₃O₇ sample. This procedure, alongside YBa₂Cu₃O₇ being fully opaque to 400 nm radiation, ensured that the GaP detector was not exposed to the pump pulses.

The YBa₂Cu₃O₇ thin film samples were embedded in the detector assembly (see Figure 3.9) and mounted on the cold finger of a liquid helium cryostat to allow for temperature control. The cryostat was directly placed in a high vacuum chamber that also contained the part of the optical setup dedicated to polarization analysis to avoid spurious contributions arising from vacuum windows. A pair of coils in a Helmholtz configuration generated a magnetic field at the sample position whose polarity could be reversed at a frequency of 450 Hz. The highest achievable magnetic field was

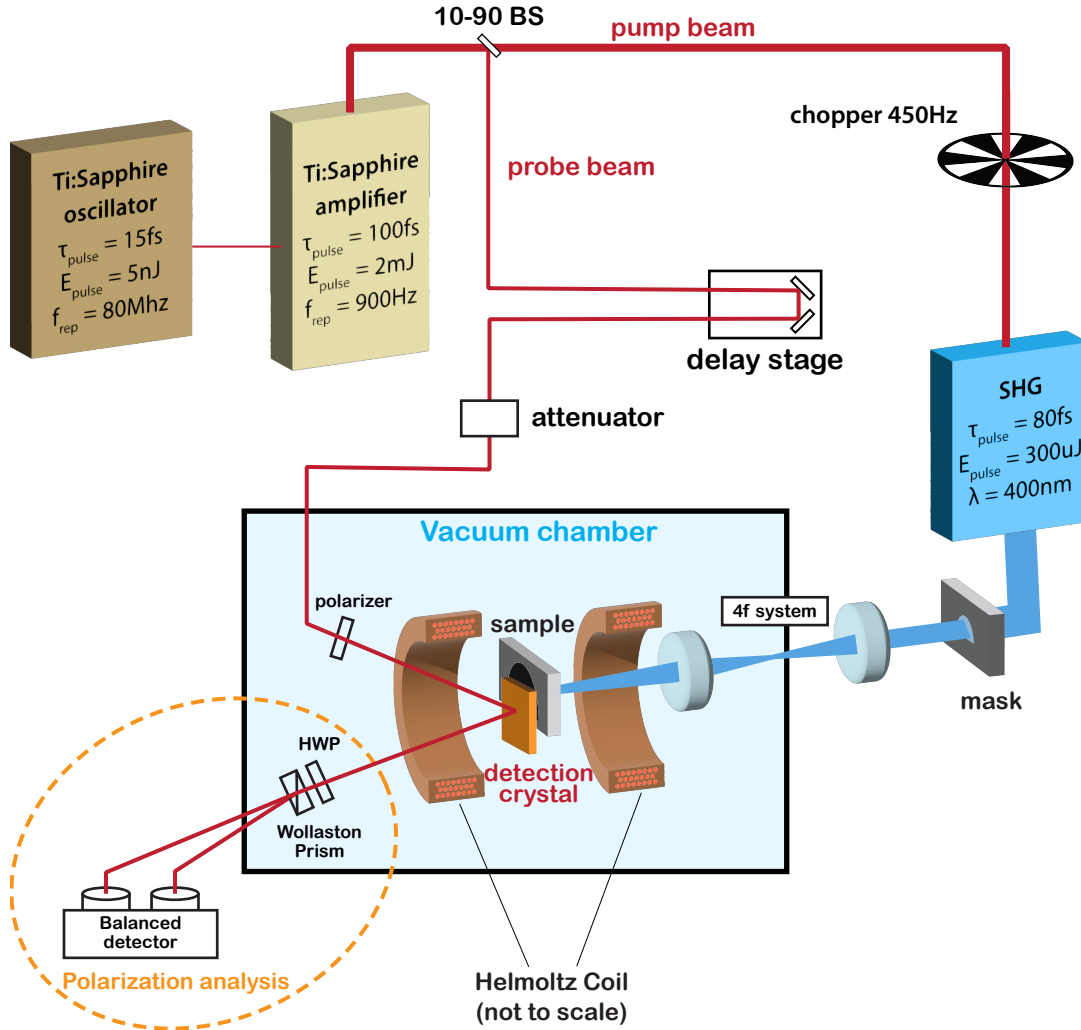


FIGURE B.1: Experimental setup for thin-film measurements presented in Chapter 3.

limited by heat dissipation and was ~ 3 mT. The sample position was controlled using computer-driven linear translation stages that made it possible to reproducibly move the cryostat and the sample inside the vacuum chamber with ~ 10 μm repeatability.

The measurements shown in Chapter 4 were carried out with a different experimental setup sketched in Figure B.2. Here, 800 nm pulses were generated using a pair of commercial Ti:Al₂O₃ amplifiers seeded by the same oscillator to achieve femtosecond synchronization. One amplifier produced 35 fs long, ~ 2 mJ pulses at 2 kHz repetition rate and was used for the probe beam. The second amplifier produced ~ 60 fs long, ~ 5 mJ pulses at 1 kHz repetition rate and was used to pump a home built three stages Optical Parametric Amplifier (OPA) that generated ~ 2 mJ total energy signal and idler pulses. These pulses were mixed in a 0.4 mm-thick GaSe crystal to obtain Difference Frequency Generated (DFG) ~ 150 fs long, ~ 20 mJ energy pulses centered at ~ 20 Hz, close to resonance with the B_{1u} apical oxygen phonon modes of YBa₂Cu₃O_{6.48}. These pulses were then chirped using a 10 mm-long NaCl

rod to a duration of ~ 1 ps in order to match the optimum pulse length for inducing superconducting-like optical properties in $\text{YBa}_2\text{Cu}_3\text{O}_{6.48}$ [17]. While the sample stages and cryostat were similar between the two setups, in this case, the polarization analysis setup is fully “in-line”, i.e., the beam travels directly from the polarizer to the Wollaston analyzer without being reflected by additional mirrors other than the detector. This scheme contributed to further reducing spurious sources of polarization noise. A magnetic field was applied at the sample position using a pair of Helmholtz coils whose polarity was switched at ~ 10 Hz frequency and could reach a maximum amplitude of 12.5 mT.

In both experimental setups, the polarity of the magnetic field is cycled periodically at a sub-harmonic of the pump and probe repetition rates. In order to obtain differential pump-probe measurements, the electrical pulses from the balanced photodetector were digitized using a commercial 8-channel 40 MS/s data acquisition (DAQ) card, triggered at the lowest frequency used in the experiment. These signals, acquired in the time domain, were then integrated after applying boxcar functions, yielding the signal amplitude from the sum and difference channels of the balanced photodetector for each probe laser pulse. Since acquiring an entire pulse sequence requires the acquisition of many pump-probe cycles, the sample clock signal of the data acquisition card is derived using direct digital synthesis from the oscillator repetition rate. In this way, drifts in the cavity length and repetition rates of the system do not affect the relative timing of the boxcar functions with respect to the arrival time of the electrical pulse.

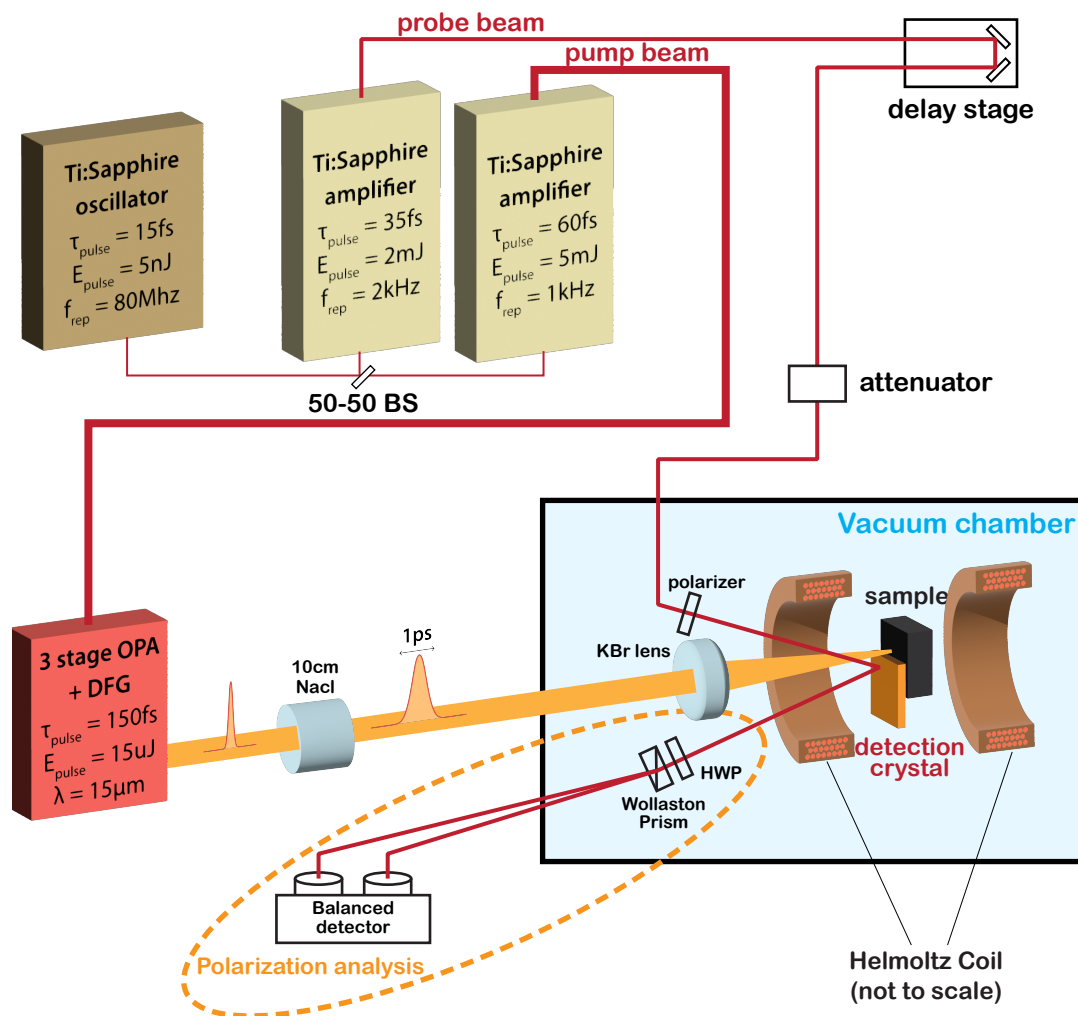


FIGURE B.2: Experimental setup for bulk measurements presented in Chapter 4.

Appendix C

Data acquisition and analysis

As mentioned in the Appendix B, for all the experiments, the polarity of the magnetic field was cycled periodically, and measurements with and without the pump were acquired to yield double differential pump-probe measurements and isolate contributions to the polarization rotation that were induced by the applied magnetic field. This procedure allowed us to filter out all contributions to the polarization rotation that would not invert with the externally applied magnetic field. In other words, because the pump-induced magnetic field changes measured with applied field $-B_{ext}$ were subtracted from those acquired with applied field $+B_{ext}$, the signal is not sensitive to magnetic fields carried by the MIR pulse itself or due to transient generation of fast electrons in the sample. In the following, we discuss this approach in detail and its impact on the measured quantities.

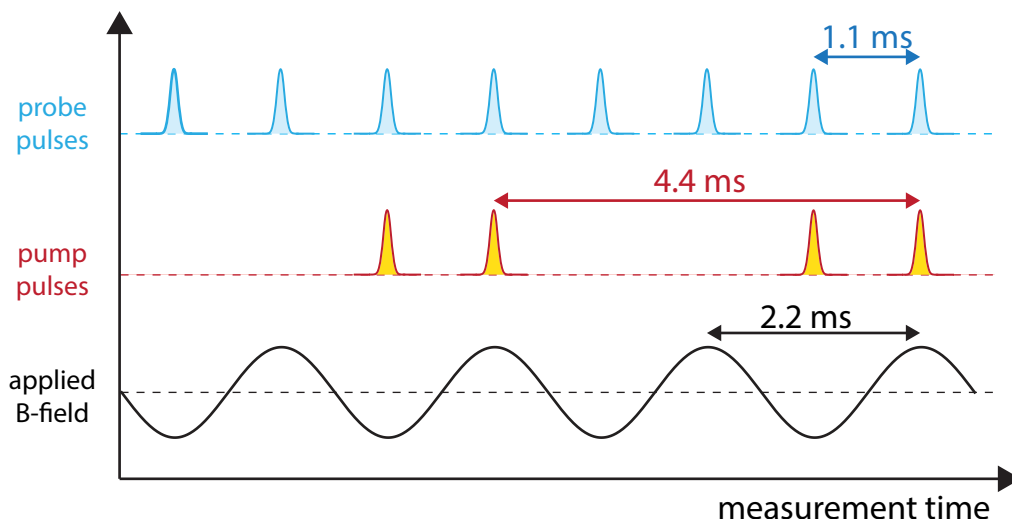


FIGURE C.1: Data acquisition scheme for $\text{YBa}_2\text{Cu}_3\text{O}_7$ measurements presented in Chapter 3.

For the measurements presented in Chapter 3, the magnetic field polarity was cycled following a sinewave at 450 Hz, and the pump was mechanically chopped at 225 Hz. A timing diagram of the acquisition scheme is shown in Figure C.1. The amplitude of the signal of the balanced photodetector difference channel is normalized by that of the sum channel in a pulse-by-pulse manner and indicated as *Normalized Difference* (ND). With the same convention as in Equation 3.14, we compute the

Normalized Magnetic (NM) observable by subtracting the ND signals obtained with a negative polarity of the magnetic field from those obtained with a positive polarity and indicate them as NM_i . The subscript i runs over the n repetitions in the acquisition. Furthermore, we distinguish those acquired in the presence of the pump from those at equilibrium with the superscripts *pump* and *equil*, respectively. The i -th pump-probe differential of the NM signal is indicated as *Normalized Pump Probe Magnetic* (NPPM) signal and is defined as

$$\text{NPPM}_i := \text{NM}_i^{\text{pump}} - \text{NM}_i^{\text{equil}} \quad (\text{C.1})$$

The quantities NM^{equil} and NPPM are then obtained as the averages of $\text{NM}_i^{\text{equil}}$ and NPPM_i over n pulses and are proportional to the static and pump-induced differential Faraday angles, respectively. After calibration of the Faraday effect in the GaP (100) detector, these quantities yielded the amplitude of the magnetic field and its pump-induced changes. To cancel out residual drifts, the phase of the magnetic field and that of the pump laser with respect to the probe laser were periodically alternated between 0 and π .

The measurements reported in Chapter 4 were acquired employing a slightly different scheme, shown in Figure C.2, to ensure that the sample was excited in a constant magnetic field. Here, the probe repetition rate was 2 kHz, and the pump struck the sample every second probe pulse (i.e., at 1 kHz). At the same time, the magnetic field polarity was modulated following a square wave at a lower frequency of around ~ 10 Hz. This scheme ensured that the sample was photo-excited in a constant magnetic field. The same quantities described above were calculated, yielding double-differential pump-probe measurements that distilled only the contributions to the polarization rotation arising from pump-induced changes in the sample magnetic properties.

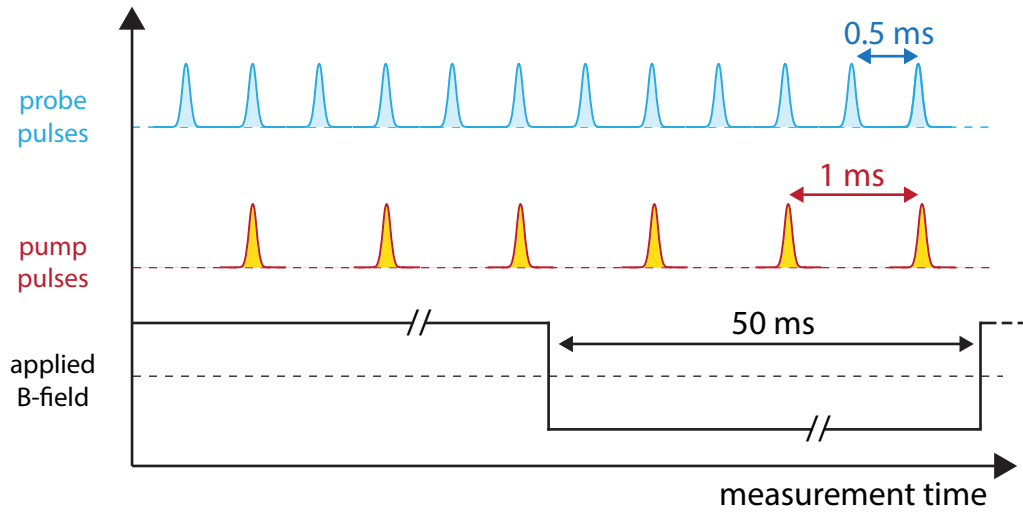


FIGURE C.2: Data acquisition scheme for $\text{YBa}_2\text{Cu}_3\text{O}_{6.48}$ measurements presented in Chapter 4.

Appendix D

Quasi-static magnetic simulations

The changes in the magnetic field surrounding the sample were computed numerically using a commercial software (COMSOL Multiphysics[®]), which employs a finite element method to solve Maxwell's equations taking into account the geometry of the experiment. The solution domain was defined as a spherical region of 1 mm radius in which a constant uniform magnetic field was applied. A half-disk-shaped region characterized by a uniform and field-independent magnetic susceptibility χ was placed in the center of the spherical region and was used to model the magnetic response of either the patterned $\text{YBa}_2\text{Cu}_3\text{O}_7$ thin film or the photo-excited region in $\text{YBa}_2\text{Cu}_3\text{O}_{6.48}$.

Although the size of the half-disk in the simulation was exactly matched to the one used in the experiments for the patterned $\text{YBa}_2\text{Cu}_3\text{O}_7$, assumptions had to be made regarding the thickness of the photo-excited region in $\text{YBa}_2\text{Cu}_3\text{O}_{6.48}$. The latter was modeled as a half-disk of 375 μm diameter, coinciding with the measured 15 μm pump beam spot size, using different thickness values corresponding to different assumptions on the pump penetration depth as discussed below. The weak magnetic response of the substrate or the unperturbed $\text{YBa}_2\text{Cu}_3\text{O}_{6.48}$ bulk was not included in the modeling as these are expected to be several orders of magnitude smaller because of their much lower magnetic susceptibility.

To account for the vertical spatial resolution of the detector that, as discussed in Section 3.3, is determined by the vertical dimension of the detection crystal, the results of the calculation were averaged over the detector thickness. This yielded two-dimensional maps of the spatially resolved magnetic field that were then convoluted with a two-dimensional Gaussian function to account for the lateral spatial resolution given by the finite size of the probe beam focus.

Figure D.1 shows a comparison between a line scan measured across the straight edge of the $\text{YBa}_2\text{Cu}_3\text{O}_7$ half-disk in an external field of 2 mT and the results of a magnetostatic calculation performed using geometrical parameters that reflect the experimental conditions. In this simulation, χ was varied to achieve the best agreement with the experimental data. The extracted value for $\chi \sim -1$ is compatible with the ZFC magnetic properties of $\text{YBa}_2\text{Cu}_3\text{O}_7$ thin films [74]. Indeed, owing to the magnetic field polarity inversion described in Appendix B, the NM signal defined in Appendix C is effectively sampling a ZFC response. This can be understood by considering that, in the presence of an impurity, the associated trapped flux does not change when the

external field is inverted. Therefore, the differential magnetic signal measured above the impurity is zero, equivalent to the field sampled above an ideal superconductor.

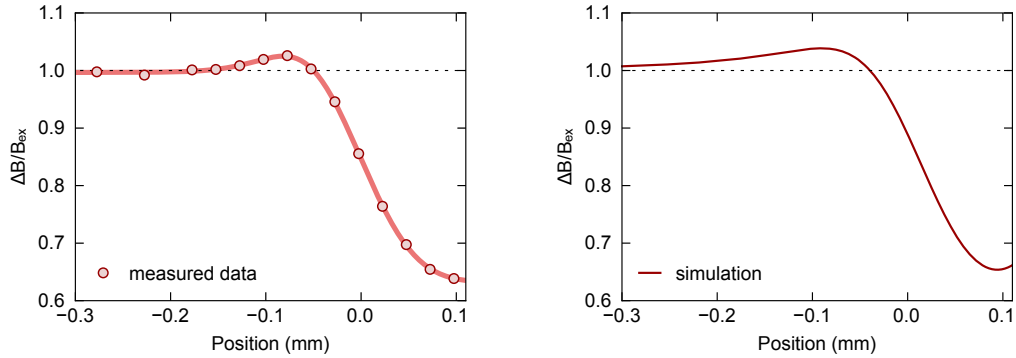


FIGURE D.1: Comparison between measured magnetometry data and simulations.

The left plot in Figure 4.2 shows the temperature dependence of the magnetic field measured at equilibrium on top of a $\text{YBa}_2\text{Cu}_3\text{O}_{6.48}$ single crystal, using a magneto-optic detector of thickness $250\ \mu\text{m}$. At $T_c \sim 55\ \text{K}$, as the sample turns superconducting, a sudden decrease in the measured magnetic field is observed. Magnetostatic calculations were used to link the measured magnetic field expulsion to the magnetic susceptibility of the $\text{YBa}_2\text{Cu}_3\text{O}_{6.48}$ sample. The right plot in Figure 4.2 shows a comparison of the extracted magnetic susceptibility χ with that measured on the same sample with a commercial DC SQUID magnetometer. The agreement between these two measurements is very good, validating this approach.

Similar calculations were used to quantify the magnetic susceptibility that the photo-excited region in $\text{YBa}_2\text{Cu}_3\text{O}_{6.48}$ should acquire after photo-excitation to produce a magnetic field change equal to that measured at the peak of the pump-probe response. This was achieved by running the calculations for a set of χ values and thicknesses of the photo-excited region to obtain calibration curves that related the average magnetic field expulsion measured $50\ \mu\text{m}$ away from the edge to the susceptibility χ . The conversion curve shown on the right of Figure 4.6 is calculated under the assumption of a thickness d of the photo-excited region equal to $2\ \mu\text{m}$, corresponding to the electric field penetration depth of the pump, defined as

$$d = \frac{c}{\omega \Im[\tilde{n}_0]}$$

where \tilde{n}_0 is the stationary complex refractive index of $\text{YBa}_2\text{Cu}_3\text{O}_{6.48}$ along the c -axis [75] at the pump frequency. This assumption is justified given the sublinear fluence dependence reported in Figure 4.10. Figure D.2 shows the dependence of the extracted χ on the thickness d of the photo-excited region used in the magnetostatic calculations. Three different assumptions are considered:

- $d = 1\ \mu\text{m}$, corresponding to the intensity penetration depth of the pump;

- $d = 2 \mu\text{m}$, corresponding to the electric field penetration depth of the pump;
- $d = 5 \mu\text{m}$, corresponding to the region in which about 99% of the pump energy is absorbed.

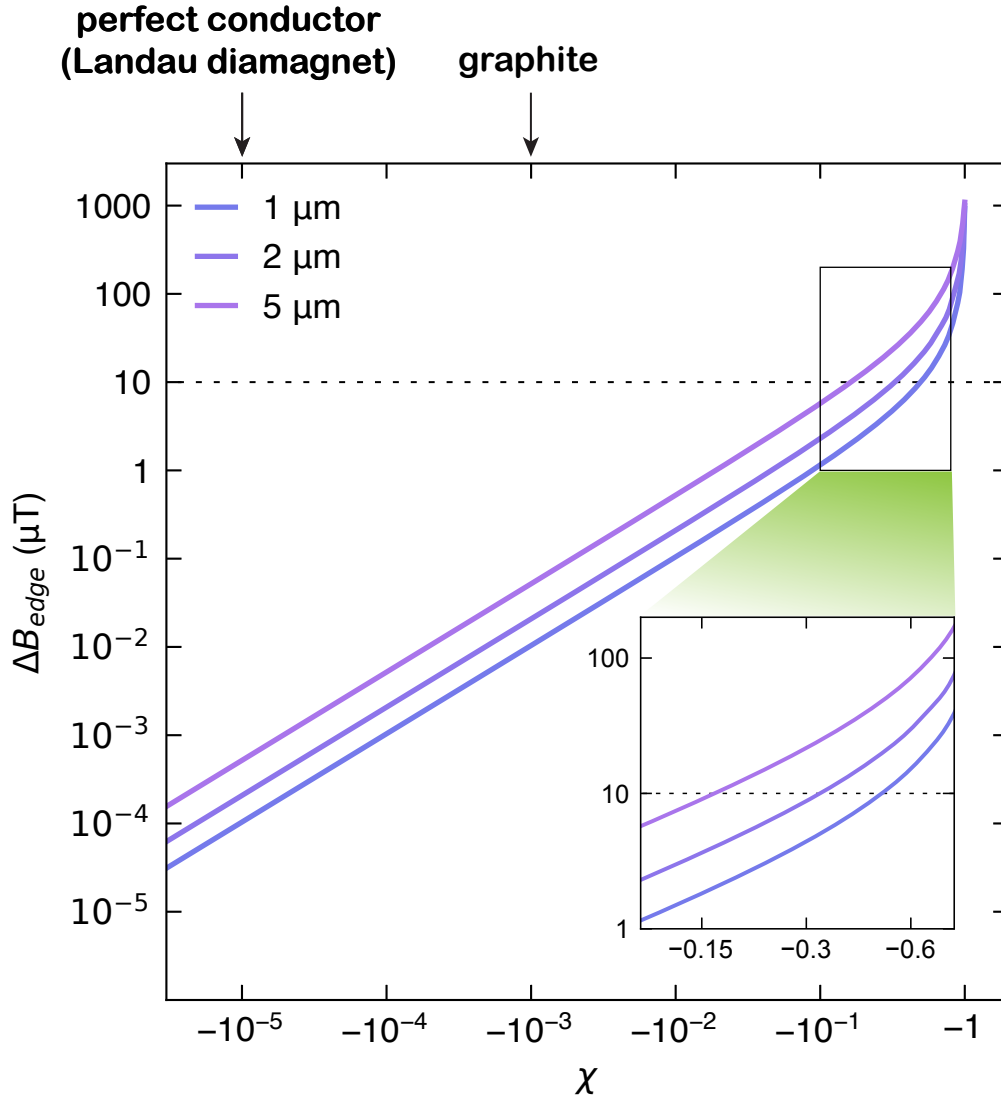


FIGURE D.2: Magnetic susceptibility estimates.

We stress that independently of the chosen value for the penetration depth d , the retrieved absolute value of χ remains in the 10^{-1} range, several orders of magnitude higher than the strongest diamagnetic response observed in metallic systems such as graphite.

Bibliography

- [1] Ye Yang et al. “Pressure-Induced Transition from a Mott Insulator to a Ferromagnetic Weyl Metal in $\text{La}_2\text{O}_3\text{Fe}_2\text{Se}_2$ ”. In: *Nature Communications* 14.1 (Apr. 2023).
- [2] S. Gerber et al. “Three-Dimensional Charge Density Wave Order in $\text{YBa}_2\text{Cu}_3\text{O}_{6.67}$ at High Magnetic Fields”. In: *Science* 350.6263 (Nov. 2015).
- [3] Philip B. Allen. “Theory of Thermal Relaxation of Electrons in Metals”. In: *Physical Review Letters* 59.13 (Sept. 1987).
- [4] Alberto de la Torre et al. “Colloquium: Nonthermal Pathways to Ultrafast Control in Quantum Materials”. In: *Reviews of Modern Physics* 93.4 (Oct. 2021).
- [5] T. F. Nova et al. “Metastable Ferroelectricity in Optically Strained SrTiO_3 ”. In: *Science* 364.6445 (June 2019).
- [6] D. Fausti et al. “Light-Induced Superconductivity in a Stripe-Ordered Cuprate”. In: *Science* 331.6014 (Jan. 2011).
- [7] D. Nicoletti et al. “Optically Induced Superconductivity in Striped $\text{La}_{2-x}\text{Ba}_x\text{CuO}_4$ by Polarization-Selective Excitation in the near Infrared”. In: *Physical Review B* 90.10 (Sept. 2014).
- [8] D. Nicoletti et al. “Magnetic-Field Tuning of Light-Induced Superconductivity in Striped $\text{La}_{2-x}\text{Ba}_x\text{CuO}_4$ ”. In: *Physical Review Letters* 121.26 (Dec. 2018).
- [9] M. Buzzi et al. “Photomolecular High-Temperature Superconductivity”. In: *Physical Review X* 10.3 (Aug. 2020).
- [10] M. Buzzi et al. “Phase Diagram for Light-Induced Superconductivity in $\kappa\text{-(ET)}_2\text{-X}$ ”. In: *Physical Review Letters* 127.19 (Nov. 2021).
- [11] M. Mitrano et al. “Possible Light-Induced Superconductivity in K_3C_{60} at High Temperature”. In: *Nature* 530.7591 (Feb. 2016).
- [12] A. Cantaluppi et al. “Pressure Tuning of Light-Induced Superconductivity in K_3C_{60} ”. In: *Nature Physics* 14.8 (Aug. 2018).
- [13] E. Rowe et al. “Resonant Enhancement of Photo-Induced Superconductivity in K_3C_{60} ”. In: *Nature Physics* 19.12 (Dec. 2023).
- [14] W. Hu et al. “Optically Enhanced Coherent Transport in $\text{YBa}_2\text{Cu}_3\text{O}_{6.5}$ by Ultrafast Redistribution of Interlayer Coupling”. In: *Nature Materials* 13.7 (July 2014).

-
- [15] S. Kaiser et al. “Optically Induced Coherent Transport Far above T_c in Underdoped $\text{YBa}_2\text{Cu}_3\text{O}_{6+\delta}$ ”. In: *Physical Review B* 89.18 (May 2014).
- [16] B. Liu et al. “Pump Frequency Resonances for Light-Induced Incipient Superconductivity in $\text{YBa}_2\text{Cu}_3\text{O}_{6.5}$ ”. In: *Physical Review X* 10.1 (Mar. 2020).
- [17] A. Ribak et al. “Two-Fluid Dynamics in Driven $\text{YBa}_2\text{Cu}_3\text{O}_{6.48}$ ”. In: *Physical Review B* 107.10 (Mar. 2023).
- [18] P. E. Goa et al. “Magneto-Optical Imaging Setup for Single Vortex Observation”. In: *Review of Scientific Instruments* 74.1 (Jan. 2003).
- [19] M. R. Freeman. “Picosecond Studies of Nonequilibrium Flux Dynamics in Superconductors”. In: *MRS Online Proceedings Library* 290.1 (Nov. 1992).
- [20] H. Kamerlingh Onnes. “Further Experiments with Liquid Helium. G. On the Electrical Resistance of Pure Metals, Etc. VI. On the Sudden Change in the Rate at Which the Resistance of Mercury Disappears.” In: *Through Measurement to Knowledge: The Selected Papers of Heike Kamerlingh Onnes 1853–1926*. Ed. by Heike Kamerlingh Onnes, Kostas Gavroglu, and Yorgos Goudaroulis. Dordrecht: Springer Netherlands, 1991.
- [21] J. File and R. G. Mills. “Observation of Persistent Current in a Superconducting Solenoid”. In: *Physical Review Letters* 10.3 (Feb. 1963).
- [22] G. De Vecchi et al. *Generation of Ultrafast Magnetic Steps for Coherent Control*. Aug. 2024. arXiv: [2408.05153](https://arxiv.org/abs/2408.05153) [[cond-mat](#), [physics:physics](#)].
- [23] J. A. Osborn. “Demagnetizing Factors of the General Ellipsoid”. In: *Physical Review* 67.11-12 (June 1945).
- [24] Michael Tinkham. *Introduction to Superconductivity*. 2 ed. Dover Books on Physics. Mineola, NY: Dover Publ, 2015.
- [25] George B. Arfken, Hans-Jurgen Weber, and Frank E. Harris. *Mathematical Methods for Physicists: A Comprehensive Guide*. 7th ed. Amsterdam ; Boston: Elsevier, 2013.
- [26] W. A. Little and R. D. Parks. “Observation of Quantum Periodicity in the Transition Temperature of a Superconducting Cylinder”. In: *Physical Review Letters* 9.1 (July 1962).
- [27] Charles P. Poole. *Superconductivity*. 3rd edition. Waltham, MA: Elsevier, 2014.
- [28] T. Okugawa et al. “Anti-Poiseuille Flow: Increased Vortex Velocity at Superconductor Edges”. In: *Physical Review B* 105.22 (June 2022).
- [29] Timm Carsten. “Theory of Superconductivity”.
- [30] J. M. Kosterlitz and D. J. Thouless. “Ordering, Metastability and Phase Transitions in Two-Dimensional Systems”. In: *Journal of Physics C Solid State Physics* 6 (Apr. 1973).

- [31] V. J. Emery and S. A. Kivelson. “Importance of Phase Fluctuations in Superconductors with Small Superfluid Density”. In: *Nature* 374.6521 (Mar. 1995).
- [32] R. J. Cava et al. “Structural Anomalies, Oxygen Ordering and Superconductivity in Oxygen Deficient $\text{Ba}_2\text{YCu}_3\text{O}_x$ ”. In: *Physica C: Superconductivity* 165.5 (Feb. 1990).
- [33] E. Pavarini et al. “Band-Structure Trend in Hole-Doped Cuprates and Correlation with $T_{c \text{ max}}$ ”. In: *Physical Review Letters* 87.4 (July 2001).
- [34] Robert W. Boyd. *Nonlinear Optics*. 3rd ed. Amsterdam ; Boston: Academic Press, 2008.
- [35] M. Först et al. “Nonlinear Phononics as an Ultrafast Route to Lattice Control”. In: *Nature Physics* 7.11 (Nov. 2011).
- [36] R. Mankowsky et al. “Nonlinear Lattice Dynamics as a Basis for Enhanced Superconductivity in $\text{YBa}_2\text{Cu}_3\text{O}_{6.5}$ ”. In: *Nature* 516.7529 (Dec. 2014).
- [37] Nikolay Plakida. *High-Temperature Cuprate Superconductors: Experiment, Theory, and Applications*. Vol. 166. Springer Series in Solid-State Sciences. Berlin, Heidelberg: Springer Berlin Heidelberg, 2010.
- [38] Y. Sato et al. “Thermodynamic Evidence for a Nematic Phase Transition at the Onset of the Pseudogap in $\text{YBa}_2\text{Cu}_3\text{O}_y$ ”. In: *Nature Physics* 13.11 (Nov. 2017).
- [39] R. Daou et al. “Broken Rotational Symmetry in the Pseudogap Phase of a High- T_c Superconductor”. In: *Nature* 463.7280 (Jan. 2010).
- [40] Arkady Shekhter et al. “Bounding the Pseudogap with a Line of Phase Transitions in $\text{YBa}_2\text{Cu}_3\text{O}_{6+\delta}$ ”. In: *Nature* 498.7452 (June 2013).
- [41] B. Fauqué et al. “Magnetic Order in the Pseudogap Phase of High- T_C Superconductors”. In: *Physical Review Letters* 96.19 (May 2006).
- [42] M. Hücker et al. “Competing Charge, Spin, and Superconducting Orders in Underdoped $\text{YBa}_2\text{Cu}_3\text{O}_y$ ”. In: *Physical Review B* 90.5 (Aug. 2014).
- [43] S. Blanco-Canosa et al. “Resonant X-Ray Scattering Study of Charge-Density Wave Correlations in $\text{YBa}_2\text{Cu}_3\text{O}_{6+x}$ ”. In: *Physical Review B* 90.5 (Aug. 2014).
- [44] Tao Wu et al. “Magnetic-Field-Induced Charge-Stripe Order in the High-Temperature Superconductor $\text{YBa}_2\text{Cu}_3\text{O}_y$ ”. In: *Nature* 477.7363 (Sept. 2011).
- [45] Tao Wu et al. “Incipient Charge Order Observed by NMR in the Normal State of $\text{YBa}_2\text{Cu}_3\text{O}_y$ ”. In: *Nature Communications* 6.1 (Mar. 2015).
- [46] Suchitra E. Sebastian et al. “Normal-State Nodal Electronic Structure in Underdoped High- T_c Copper Oxides”. In: *Nature* 511.7507 (July 2014).
- [47] P. Carretta et al. “Superconducting Fluctuations and Anomalous Diamagnetism in Underdoped $\text{YBa}_2\text{Cu}_3\text{O}_{6+x}$ from Magnetization and ^{63}Cu NMR-NQR Relaxation Measurements”. In: *Physical Review B* 61.18 (May 2000).

- [48] Lu Li et al. “Diamagnetism and Cooper Pairing above T_c in Cuprates”. In: *Physical Review B* 81.5 (Feb. 2010).
- [49] S. Martin et al. “Normal-State Transport Properties of $\text{Bi}_{2+x}\text{Sr}_{2-y}\text{CuO}_{6\pm\delta}$ Crystals”. In: *Physical Review B* 41.1 (Jan. 1990).
- [50] T. R. Chien, Z. Z. Wang, and N. P. Ong. “Effect of Zn Impurities on the Normal-State Hall Angle in Single-Crystal $\text{YBa}_2\text{Cu}_{3-x}\text{Zn}_x\text{O}_{7-\delta}$ ”. In: *Physical Review Letters* 67.15 (Oct. 1991).
- [51] C. M. Varma et al. “Phenomenology of the Normal State of Cu-O High-Temperature Superconductors”. In: *Physical Review Letters* 63.18 (Oct. 1989).
- [52] Jan Zaanen et al. *Holographic Duality in Condensed Matter Physics*. Cambridge: Cambridge University Press, 2015.
- [53] Y. J. Uemura et al. “Universal Correlations between T_c and n_s/m^* (Carrier Density over Effective Mass) in High- T_c Cuprate Superconductors”. In: *Physical Review Letters* 62.19 (May 1989).
- [54] R. D. Averitt et al. “Nonequilibrium Superconductivity and Quasiparticle Dynamics in $\text{YBa}_2\text{Cu}_3\text{O}_{7-\delta}$ ”. In: *Physical Review B* 63.14 (Mar. 2001).
- [55] S. Fava et al. “Magnetic Field Expulsion in Optically Driven $\text{YBa}_2\text{Cu}_3\text{O}_{6.48}$ ”. In: *Nature* 632.8023 (Aug. 2024).
- [56] A. von Hoegen et al. “Amplification of Superconducting Fluctuations in Driven $\text{YBa}_2\text{Cu}_3\text{O}_{6+x}$ ”. In: *Physical Review X* 12.3 (July 2022).
- [57] B. Liu et al. “Generation of Narrowband, High-Intensity, Carrier-Envelope Phase-Stable Pulses Tunable between 4 and 18 THz”. In: *Optics Letters* 42.1 (Jan. 2017).
- [58] N. Taherian et al. *Squeezed Josephson Plasmons in Driven $\text{YBa}_2\text{Cu}_3\text{O}_{6+x}$* . Jan. 2024. arXiv: [2401.01115](https://arxiv.org/abs/2401.01115) [cond-mat].
- [59] Marios H. Michael et al. “Parametric Resonance of Josephson Plasma Waves: A Theory for Optically Amplified Interlayer Superconductivity in $\text{YBa}_2\text{Cu}_3\text{O}_{6+x}$ ”. In: *Physical Review B* 102.17 (Nov. 2020).
- [60] Y. Yuan, J. Theile, and J. Engemann. “Measurement of the Meissner Effect by a Magneto-Optic Ac Method Using Ferrimagnetic Garnet Films”. In: *Journal of Magnetism and Magnetic Materials* 95.1 (Apr. 1991).
- [61] M. R. Koblischka and R. J. Wijngaarden. “Magneto-Optical Investigations of Superconductors”. In: *Superconductor Science and Technology* 8.4 (Apr. 1995).
- [62] J.A. Riordan and X.-C. Zhang. “Sampling of Free-Space Magnetic Pulses”. In: *Optical and Quantum Electronics* 32.4 (May 2000).
- [63] D. F. Parsons and P. D. Coleman. “Far Infrared Optical Constants of Gallium Phosphide”. In: *Applied Optics* 10.7 (July 1971).

- [64] J. A. Riordan, Z. G. Lu, and X.-C. Zhang. “Free-Space Ultrafast Magneto-Optic Sampling”. In: *Conference on Lasers and Electro-Optics (1997), Paper CPD10*. Optica Publishing Group, May 1997.
- [65] T. Dietl et al. “Dynamics of Spin Organization in Diluted Magnetic Semiconductors”. In: *Physical Review Letters* 74.3 (Jan. 1995).
- [66] R. Rey-de-Castro et al. “Subpicosecond Faraday Effect in $\text{Cd}_{1-x}\text{Mn}_x\text{Te}$ and Its Application in Magneto-Optical Sampling”. In: *Applied Physics Letters* 85.17 (Oct. 2004).
- [67] R. Rey-de-Castro et al. “Subpicosecond Magneto-Optical Sampling with $\text{Cd}_{1-x}\text{Mn}_x\text{Te}$ ”. In: *Annals of Physical and Rehabilitation Medicine* (Jan. 2004).
- [68] R. Rey-de-Castro. “Ultrafast Optical Properties and Applications of $\text{Cd}_{1-x}\text{Mn}_x\text{Te}$ Semimagnetic Semiconductors”. PhD thesis. University of Rochester, 2004.
- [69] Paul Fumagalli and J. Schoenes. *Magneto-Optics: An Introduction*. De Gruyter Graduate. Berlin ; Boston: De Gruyter, 2022.
- [70] Chia-Chu Chen and John F. Whitaker. “An Optically-Interrogated Microwave-Poynting-vector Sensor Using Cadmium Manganese Telluride”. In: *Optics Express* 18.12 (June 2010).
- [71] Amikam Aharoni. “Demagnetizing Factors for Rectangular Ferromagnetic Prisms”. In: *Journal of Applied Physics* 83.6 (Mar. 1998).
- [72] T. R. Dinger et al. “Direct Observation of Electronic Anisotropy in Single-Crystal $\text{Y}_1\text{Ba}_2\text{Cu}_3\text{O}_{7-x}$ ”. In: *Physical Review Letters* 58.25 (June 1987).
- [73] Katja Höflich et al. “Roadmap for Focused Ion Beam Technologies”. In: *Applied Physics Reviews* 10.4 (Dec. 2023).
- [74] Abdalla A. Elabbar. “AC Response of $\text{YBa}_2\text{Cu}_3\text{O}_7$ Thin Film Superconductor”. In: *Physica C: Superconductivity* 469.4 (Feb. 2009).
- [75] C. C. Homes et al. “Optical Properties along the C-Axis of $\text{YBa}_2\text{Cu}_3\text{O}_{6+x}$, for $x = 0.50 \rightarrow 0.95$ Evolution of the Pseudogap”. In: *Physica C: Superconductivity* 254.3 (Nov. 1995).

Acknowledgements

Prima di tutti, vorrei ringraziare la mia famiglia, che sin da piccolo mi ha sostenuto e mi ha dato i mezzi per fare una vita privilegiata, dove mi possa concedere di inseguire i miei sogni e le mie ambizioni. Le stesse opportunità non sono arrivate per voi, e il fatto che, nonostante tutto, voi abbiate scelto il sacrificio definisce la vostra persona. La distanza a cui ci ha spinto non altera il bene che vi voglio, e non vedo l'ora di condividere tanti nuovi ricordi assieme a voi.

My sincere acknowledgments are then due to my supervisor, Andrea Cavalleri. Since our first meeting, you warned me, "In this group, either we do great things, or we die trying." and I'm glad I didn't die. From you, I learned the art of focusing towards a goal rather than going off a tangent. I will do my best to implement this teaching in my future academic life.

I owe my deepest thanks to my scientific (and life) mentor, Michele Buzzi. On more than one occasion, I genuinely thanked every superior being possible for allowing me to learn from you and receiving your unconditioned support, sometimes even at your own expense. Your help extends much further the infinite number of breathtaking restaurants you suggested, and I will fondly remember the nights spent in the 49 lab. But most of all, I won't forget the lesson you taught me while looking for mirror knob holes.

As a second mentor, I'd like to thank Gregor Jotzu. I truly enjoyed our coffee break chats and your genuine scientific curiosity, which felt like fresh air in an environment often focused on overachieving rather than understanding. I wish you the best with your new group in Lausanne, and I hope our paths cross again in the future. Hopefully, one day, our lunch club will come back to life!

Special thanks go to all the wonderful friends and colleagues that I met at work, even those that were inappropriate. I cannot mention you all because you are too many for a single page. Still, I'll make sure to drag you all over to my place for a last party before leaving. As an exception, I must thank Giovanni De Vecchi, with whom I shared much more than just our project. My days in Texas without you will be very long, especially considering I won't be able to slack off on work by playing kicker. . .

As a special mention, I would like to thank my favorite Latina, Adriana, who managed to warm up even the winters in Hamburg. Thanks for always being there when I needed it, thanks for feeding me when I was hungry, but most of all, thanks for being the beautiful person you are. I couldn't feel more lucky to have you at my side. And Moka, too, of course.

Last but not least, I would like to thank all the beautiful people that I met during my stay in Hamburg, who filled my evening with laughter and coziness (you are, of course, also invited to the party). Most of all, my greek malaka Stratos deserves an honorary mention as the last survivor of the crew. Distance may part us, but love will find a way.